January 2014

Preparation And Analysis Of Evaporatively Bonded Superalloys For Use In Hydrogen Burning Gas Turbines

Serges Eric Tatsinkou Nguelo

Follow this and additional works at: https://commons.und.edu/theses

PREPARATION AND ANALYSIS OF EVAPORATIVELY BONDED

SUPERALLOYS FOR USE IN HYDROGEN BURNING GAS TURBINES

by

Serges Eric Tatsinkou Nguelo
Bachelor of Science, University of Dschang 2011

A thesis

Submitted to the Graduate Faculty

of the

University of North Dakota
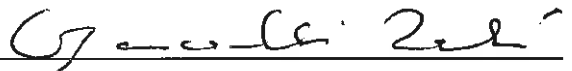
in partial fulfillment of the requirements
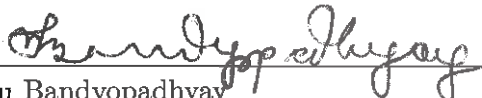

for the degree of

Master of Science

Grand Forks, North Dakota
August
2014

This thesis, submitted by Serges Eric Tatsinkou Nguelo in partial fulfillment of the requirements for the degree of Master of Science in Mechanical Engineering from the University of North Dakota, has been read by the Faculty Advisory Committee under whom the work has been done, and is hereby approved.
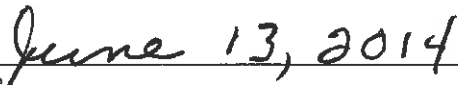
_____
Matthew Cavalli

_____
Marcellin Zahui

_____
Bishu Bandyopadhyay

This thesis is being submitted by the appointed advisory committee as having met all of the requirements of the School of Graduate Studies at the University of North Dakota and is hereby approved.

_____
Wayne Swisher

Dean of the School of Graduate Studies

_____
Date June 13, 2014

i

PERMISSION

Title   Preparation and Analysis of Evaporatively Bonded Superalloys for use
                   in Hydrogen Burning Gas Turbines

Department   Mechanical Engineering

Degree   Master of Science

      In presenting this thesis in partial fulfillment of the requirements for a graduate degree from the University of North Dakota, I agree that the library of this University shall make it freely available for inspection. I further agree that permission for extensive copying for scholarly purposes may be granted by the professor who supervised my thesis work or, in his absence, by the Chair person of the department or the dean of the School of Graduate Studies. It is understood that any copying or publication or other use of this thesis or part thereof for financial gain shall not be allowed without my written permission. It is also understood that due recognition shall be given to me and to the University of North Dakota in any scholarly use which may be made of any material in my thesis.

<div align="right">

Serges Tatsinkou
August 8, 2014

</div>

TABLE OF CONTENTS

CHAPTER

iv

LIST OF TABLES

LIST OF FIGURES

ACRONYMS

APMT	Oxide dispersion–strengthened FeCrAl alloy made by Kanthal
APS	Atomic Plasma Spraying
ASME	American Society of Mechanical Engineers
CM 247 LC	Alumina–scale–forming nickel–based superalloy
CR	Corrosion Rate
CTE	Coefficient of Linear Thermal Expansion
CVAAS	Cold Vapor Atomic Absorption Spectroscopy
CVD	Chemical Vapor Deposition
DGS	Detonation Gun Spraying
DOE	United States Department of Energy
EB–PVD	Electron Beam–Physical Vapor Deposition
EDM	Electrical Discharge Machining
EDS	Energy–Dispersive Spectroscopy
EERC	Energy and Environmental Research Center
EFG	Entrained Flow Gasifier
EIA	United States Energy Information Agency
EMB	Evaporative Metal Bonding
EPA	United States Environmental Protection Agency
FBG	Fluidized–bed Gasifier
FHWA	Federal High Way Administration
FS	Flame Spraying
GDP	Gross Domestic Product
GPS	Gamma Prime Strengthened
GT	Gas Turbine
HGFV	Hot Gas Filter Vessel
HHC	High Hydrogen Content
HVOF	High Velocity Oxygen Fuel
IC	Ion Chromatography
ICP	Inducively Coupled Plasma
IGCC	Integrated Gasification Combined Cycle
LLQ	Lower Limit of Quantification
MBC	Metallic Bond Coat
MS	Mass Spectrometry
ODS	Oxide Dispersion Strengthened
PBR	Pilling–Bedworth Ratio
PDBE	Poly Brominated Diphenyl Ethers
Rene 80	Alumina–scale–forming nickel–based superalloy
SCC	Stress Corrosion Cracking
SEM	Scanning Electron Microspy
SF	Shape Factor
TBC	Thermal Barrier Coating
TLP	Transient Liquid Phase
TOx	Thermal Oxidizer
UND	University of North Dakota
VPS	Vacuum Plasma Spraying

ACKNOWLEDGMENTS

ABSTRACT

Superalloys for use in hydrogen–burning gas turbines must demonstrate long–term durability in environments that may be more corrosive than typical turbines due to the presence of impurities in the combusted syngas. This long–term durability implies high oxidation and spallation resistance to different types of corrosion attacks as well as a high strength to be able to withstand the residual stresses induced by the temperature gradients. The performance of these superalloys in these environments can only be realistically assessed if their design involves a good understanding of the types of microcontaminants present in the syngas as well as resulting stresses induced during high temperature operation. This work has two main goals: 1) Characterize the composition of typical syngas combustion flue gases and 2) Successfully fabricate bi–layer structures of iron– and nickel–based superalloys using evaporative metal bonding (EMB) and perform a finite element analysis to predict the stresses at the bonding surface at all temperatures.

The characterization of combusted and non–combusted syngas produced using the University of North Dakota Energy and Environmental Research Center (EERC) pilot–scale gasifiers revealed the presence of elements S, Cr, Fe, Ni, Si, V, Pb, Hg, Mn, Co, K, Be, Cd, Se, Ca, Ni, Cr, Sb and Na trapped on the filter surfaces and in the impinger solutions. All trace metals detected felt in the range of 0–2 ppmw required by gas turbine (GT) manufacturers except Si and S which had ppmw values of 3.69 and 4.6 respectively. This was attributed to the fact that no sulfur removal was used during that run and the excess silicon came from the rust present at the bottom of the thermal oxidizer (TOx). These low ppmw values showed that the syngas produced at the EERC was of good quality and could be tolerated by any industrial GT. But because very small amounts of impurities could still trigger the hot corrosion of GT parts, the information on the different trace metals will be used to perform corrosion tests on joints made using the EMB process.

The modeling of bonding pressures in Rene 80 – APMT and CM 247 LC bi–layer struc-tures revealed a general trend according to which the thermally induced stresses created in the diffusion–bonded joints were more compressive at the center and tensile towards the edge. The optimization of the finite element model was done by studying the effect of some simulation parameters on the distribution of the maximum stress at the bonding surface and the best values were chosen for each one of them. The coefficient of thermal expansion (CTE) values were experimentally measured using the University of North Dakota thermo-mechanical analyzer (TMA) and used as input for the finite element simulations. The EMB process was successfully applied to joint APMT with Rene 80 and CM 247 LC cylindrical plates.

CHAPTER I

LITERATURE REVIEW

1.1 Introduction

1.1.1 Problem

The drastic depletion of natural energy resources is a crucial problem the world has been been facing for several decades now. New energy–generation methods are being sought to satisfy the energy needs of society. These include: solar energy, wind energy, biofuels and coal gasification. The first three have some major drawbacks. If the surface of interest is shielded so that it can no longer receive solar radiation or wind gusts then it becomes useless. Biofuels compete with the basic needs of humans who rely on many of the same biofuels for food. Coal gasification appears to be the most effective short–term alternative for energy production.

The energy production through coal gasification is accomplished using gas turbines (GTs). GT manufacturers are speeding up efforts to develop different models to meet the demand for enhanced fuel utilization. One of the proposed solutions is to use a very clean synthetic gas (syngas) as reactant in the combustion reaction. But the use of syngas as fuel is facing many problems including microcontaminants induced–corrosion occurring at high temperature on the GT hot section parts. As a result, the load carrying capability of these components is reduced, reducing the overall GT efficiency. Constraints on fuel quality and content have been imposed by GT manufacturers in order not only to regain but also to increase the efficiency of the current commercial GTs. With constrained fuel sources and increasing environmental focus, the quest for higher efficiency and lower emissions targets becomes more challenging every day.

According to the DOE Report of April 2013, there will be an increase of 29% in need of coal in the world in 2035, i.e. an increase of 14% from the similar report done in

2008 [1]. The EIA predicts world generation of electricity to grow by 77% (an increase of 14 trillion kilowatt–hours a year) from 2006 to 2030 [2]. A problem with this growth is that coal utilization produces a lot of unwanted gases such as CO_2, SO_2, SO_3, NO, NO_2, H_2S, NH_3, N_2, HCN, COS and particulate maters which considerably reduce the GT efficiency when present in the GT combustion gases. Many of these gases can be removed from the syngas stream using various purification techniques and used to fuel other devices or industries [3]. A well–handled removal process leaves behind a very clean syngas with high hydrogen content (HHC). But if not well–handled, some trace elements evolving from the condensation of these harmful gases will access the GT and cause the corrosion of the hot section parts during the combustion and even during the cooling down.

1.1.2 Motivation

The need for high efficiency GT requires components made of materials able to withstand temperatures up to 1500^oC [2]. These materials must have high temperature strength, good resistance to creep, oxidation and different forms of high temperature corrosion. Few, if any, materials can meet all requirements. Most commercial GT manufacturers use nickel–based superalloys to provide the mechanical strength at elevated temperatures and coat them with more temperature corrosion–resistant materials, thermal barrier coats (TBCs). Over the life of a typical turbine engine, spallation of the TBC is possible. This is often due to a thermal expansion mismatch between the TBC and the nickel superalloy. Therefore, there is a need for an appropriate interlayer between the structural alloy and the TBC. The development of a process to produce and test such a structure is a a main goal of the work presented and described in this thesis.

1.1.3 Objective

The work presented in this thesis is a part of the US DOE Project Award Number: DE–FE0007325 and entitled "PREPARATION AND TESTING OF CORROSION AND SPALLATION–RESISTANT COATINGS", whose main objective is to take a recently developed method of plating nickel superalloys with protective FeCrAl layers closer to commercial use in syngas–fired turbines. The project is designed to determine if plating APMT, a highly oxidation–resistant ODS FeCrAl alloy made by Kanthal, onto nickel–based super-

2

alloy (Rene 80 and CM 247 LC) turbine parts is a viable method for substantially improving the lifetimes and maximum use temperatures of the parts. The three superalloys used in this project were chosen from two representative classes of gas turbine materials: Rene 80 and CM 247 LC from the gamma prime–strengthened (GPS) class and APMT from the oxide directionally solidified (ODS) MCrAlY– protective coating class. Their chemical compositions are presented in Table 1.1. In addition to the data presented in Table 1.1, APMT

Table 1.1: Composition of APMT, CM 247 LC and Rene 80 in wt%. [4–6]

	Fe	Ni	Cr	Al	Ti	Co	Mo	W	Nb	C	B	Zr
APMT	bal	-	22	5	-	-	3	-	-	0.05	-	-
CM 247 LC	-	bal	8.1	5.6	0.7	9.5	0.5	9.5	0.1	0.07	0.015	0.015
Rene 80	0.1	bal	14.2	3	5.1	9.4	4	4.1	0.03	0.16	0.02	0.04

contains additional elements Mn and Si in the respective proportions: 0.4 wt% and 0.7 wt%. CM 247 LC also contains additional elements Ta and Hf in the respective proportions: 3.2 wt% and 1.4 wt%. The three superalloys were chosen because Siemens Energy, a partner in the proposed work, has found that a TBC made from yttrium–stabilized zirconia applied to an ODS FeCrAl alloy has a much greater (at least 3.5 times) spallation life (Figure 1.1) than if it is applied directly to the superalloys Rene 80 or CM 247 LC and has a much greater oxidation resistance than either of the superalloys. It has also been found that CM 247 LC
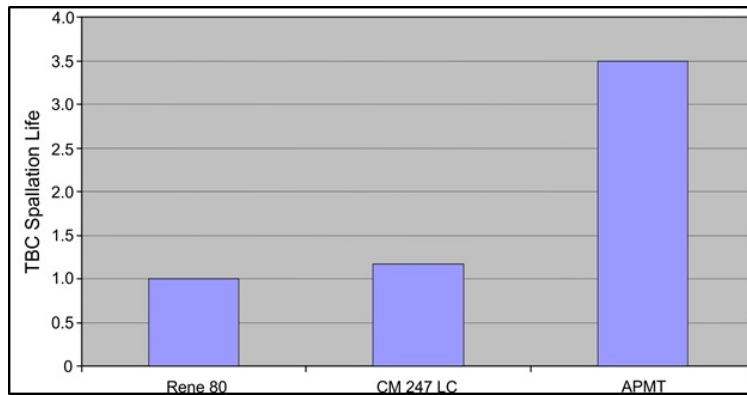
Figure 1.1: TBC spallation life comparison for the three superalloys of interest [2].

has poor oxide adhesion as compared to other alloys and Rene 80 has the greatest oxide thickness and depth of degradation [2]. A creep rupture lifetime test at 950°C and 15 MPa pressure on a CM 247 LC–APMT diffusion bonded sample showed a breakage in the APMT section far away from the joint, meaning that the diffusion bonding process creates a bond stronger than the ODS alloy itself (Figure 1.2). More details of these three superalloys as
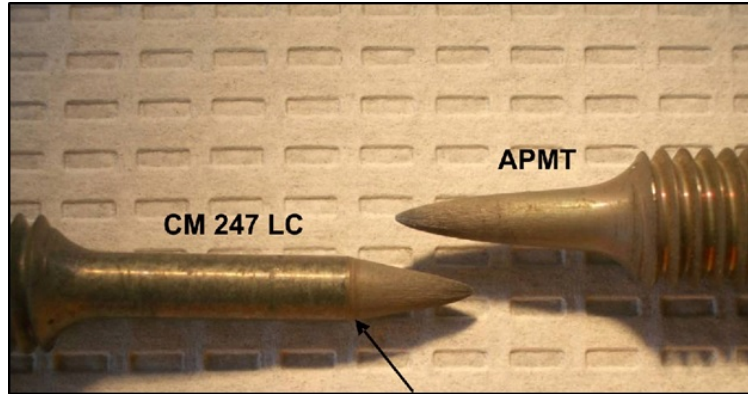
Figure 1.2: Test specimen after creep rupture test at 950°C showing the break occurs in the APMT, relatively far from the joint [2].

well as their mechanical and chemical properties can be found in Reference [2].

1.2 High Temperature Corrosion in Gas Turbines

1.2.1 Definition

A gas turbine (GT) is an internal combustion engine designed and built to generate power. It has three main components: a compressor, a combustion chamber and a turbine. Figure 1.3 shows the cut away diagram of the Rolls–Royce Trent 1000 gas turbine aero–engine with the three main components represented. A GT can be operated in a simple cycle or in a combined cycle. In a simple cycle, ambient air enters into a compressor and brought to a higher pressure (up to 30 bar) and sent to the combustion chamber where fuel is added and the mixture ignited at approximately 1350°C [8]. The combustion produces a very hot gas which is then sent to the turbine, where it expands down to the exhaust pressure, producing shaft work output in the process. In a combined cycle (of which the integrated gasification combined cycle (IGCC) is an example), the excess heat from the primary combustion is used to convert CO to CO_2 through the water–gas shift (WGS)
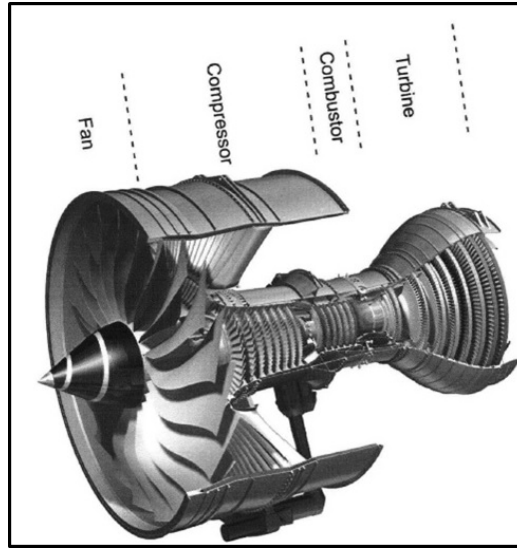
Figure 1.3: Cut away diagram of the internals of a modern high–bypass gas turbine aero–engine (Rolls-Royce Trent 1000) [7].

reaction, consuming steam and producing hydrogen in the process [9]. As result, more H_2 is produced and the efficiency can increase from 39% for a simple cycle to about 57.5% in a combined cycle [8]. The exhaust gas which finally exits the turbine at about 640°C can either be sent through a diffuser to produce electricity or through a nozzle for propulsion purposes. Depending on the needs, GTs have several applications ranging from marine to aerospace industry as shown in Figure 1.4 [10].

The introduction of new GT materials as well as the improvements in fuel quality raise a crucial need for re–evaluation of corrosion risks associated with the levels of trace metal contaminants present in the gas stream. Corrosion is defined as the deterioration of a material and its properties as a result of a chemical or electrochemical reaction between the material and its environment. Most corrosion processes occur significantly only with an electrolytic solution present. This form of corrosion is called aqueous corrosion and it occurs mostly in the compressor section of the GT. But corrosion can also occur in the absence of the electrolyte if the material is exposed to high temperatures. This form of corrosion is called high–temperature corrosion and it occurs both in the combustor and the turbine sections [11]. It occurs as well on the surfaces of heat exchangers, high pressure
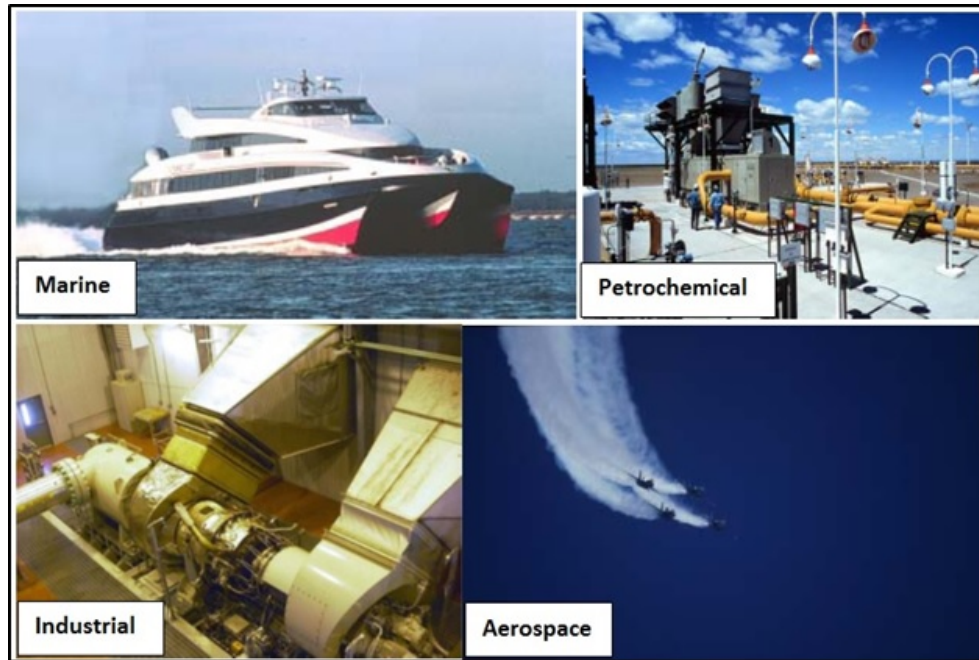
Figure 1.4: Gas turbine applications [10].

boilers, rocket engines and furnaces [12–19]. When these materials are subjected to high temperature gradients, they react actively with air as temperature increases in the system. A metal scale is first formed from the trace metals contained in the ash deposits, followed by the formation of molten salts which wash away the previously formed protective oxide layer. The process is repeated many times and, as result, there is a significant material weight loss which strongly reduces the mechanical performances and high–temperature strength of the material. Corrosion begins as soon as the material surface temperature falls below the dew point of the corrosive salt. If the degradation process is not discovered early enough and prevented, the corrosion process will continue until mechanical failure of the component part as long as oxygen is present.

High–temperature corrosion is affected by numerous factors such as temperature, exposure time, alloy composition, oxygen concentration, and gas composition. For instance, Covino *et al.* [12] recently showed that temperature greatly affects the rate of corrosion reaction (Figure 1.5). The degradation can be divided into two main classes: the gas–induced corrosion and the deposit–induced corrosion. The gas–induced corrosion results
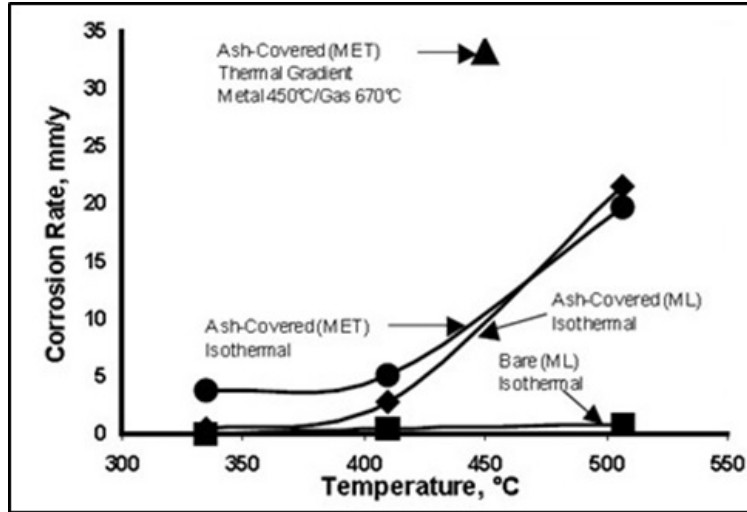
Figure 1.5: Effect of temperature and thermal gradients on the high–temperature corrosion of carbon steel boiler tubes [12].

from the reaction of the material with a gaseous environment while the deposit–induced corrosion results from the reaction of the material with a solid deposit (impurities in the form of contaminants) which condenses on the material surface and acts as a catalyst to the degradation process.

1.2.2   Mechanism

1.2.2.1   Gas–induced corrosion. Also called tarnishing, this form of corrosion results from the direct reaction occuring at high temperature between a gas and a metal. Gas–induced corrosion occurs through several processes including oxidation, chloridation, sulfidation, nitridation, and carburization.

1.2.2.1.1   Oxidation. Almost every metal will react with air at elevated temperature. Most starts to oxidize on exposure to temperatures above 300°C in environments containing greater than 1 vol% O_2 [16]. Therefore, oxidation resistance must be taken seriously in most metallurgical engineering applications. The excess air in the GT favors the formation of different types of oxides depending on the superalloy composition. According to Bordenet [8], a metal M will oxidize to M_xO_y if the partial pressure of oxygen is higher or equal to the quantity $\exp\left(\frac{\Delta G^o}{RT}\right)$ and the free enthalpy ΔG^o is negative for the reaction

defined in Equation 1.2.1:

$$2\frac{x}{y}M + O_2 \leftrightarrow \frac{2}{y}M_xO_y \qquad (1.2.1)$$

The control of metal loss as a result of oxidation or high–temperature corrosion is expressed by a power–law relationship as defined in Equation 1.2.2.

$$W = A * t^n \qquad (1.2.2)$$

Where W is the decrease in mass of metal per unit area in time t, A is a temperature–dependent coefficient and n is the rate coefficient. The value of n defines the type of loss mechanism. The value n = 1 corresponds to a linear loss, n = 0.5 to a parabolic, and n = -1 to a logarithmic loss [8, 16, 20]. The linear law corresponds to a transport–controlled oxidation while the parabolic one corresponds to a solid–state diffusion–controlled oxidation (case of FeCrAl superalloys). The parabolic law occurs in metals with thick coherent oxides while the linear law ccurs in metals with porous or cracked oxide films (transport of reactant ions occurs at faster rates than the chemical reaction) [21]. The logarithmic law is characterized by a fast oxidation at the beginning followed by a rate decrease to a very low value towards the end. The kinetics of the transport–controlled oxidation can also be assessed from the Pilling–Bedworth ratio (PBR) shown in Equation 1.2.3. The PBR is defined as the ratio of the oxide volume produced by oxidation to the volume of metal consumed by oxidation.

$$PBR = \frac{M * d}{n * m * D} \qquad (1.2.3)$$

Where (m, d) and (M, D) are the molecular weights and densities of the metal and oxide respectively, and n is the number of metal atoms in oxide formula. If PBR is less than 1.0, a poor oxide layer is formed and the oxidation is linear with time. A PBR value of 1.0 or greater results in a complete coverage of the metal surface by the formed protective oxide. But if the growth of the protective oxide is very fast, (PBR value greater than 1.0), this can lead to spallation which acts as a stress–relief mechanism [16]. In addition to a PBR value of 1.0 and a negative ΔG^o, the protective oxide film should have good adherence,

high–temperature plasticity to prevent fracture, a low vapor pressure, low conductivity and low diffusion coefficients for metal ions and oxygen, a high melting point, and a thermal coefficient of expansion comparable to that of the metal.

1.2.2.1.2   Chloridation. In the chloridation process, chlorine diffuses through the pores and cracks of the protective oxide layer and then moves toward the surface of the metal. Once it reaches the metal surface, it reacts with metal to form gaseous metal chloride. Because of the high partial pressure of this new compound, continuous evaporation of metal chloride occurs and the corrosion rate increases as well [22]. Chlorine can also react with chromium initially used in the oxide layer formation by forming chromium chloride. If the oxygen concentration in the medium is high enough then the gaseous metal chloride will react with oxygen to form metal oxide and chlorine will be released, thus forming a cycle of reactions as illustrated in Figure 1.6. Skrifvars *et al.* [23] showed that a very low amount of chlorine contained in sodium chloride salt causes corrosion of stainless steels at temperatures far below the melting point of the salt.
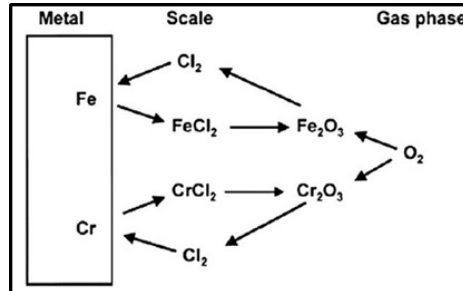
Figure 1.6: Corrosion mechanism between Cl_2 (g) and solid metal [22].

1.2.2.1.3   Sulfidation. Sulfidation or sulfur–induced corrosion is mainly due to reaction of the metal with one of the following gases H_2S, SO_2 and SO_3. Among these gases, H_2S is the most corrosive and its reaction with the base alloy produces a metal–sulfur compound that forms on or beneath the surface of the material [16, 24]. Sulfides are formed at low oxygen partial pressures while sulfates are formed at high partial pressures of oxygen. Lee *et al.* [25] demonstrated that if the oxygen potential decreases then the sulfur potential will increase and the sulfidation attack will occur underneath the protective

oxide initially formed at the alloy surface. In SO_2–containing air, any addition of water increases considerably the rate of sulfidation attack. Once sulfur enters the alloy, it ties up Cr and Al to form sulfides of chromium and aluminium, preventing any formation or reformation of the protective oxide (Cr_2O_3 or Al_2O_3). If an excess amount of sulfur is present to convert all Cr and Al completely to sulfides, then the sulfides of the base metal will form in the grain boundaries as well. These sulfides of the base metal are the ones responsible for the accelerated sulfidation often observed in GT. This is because they have a relatively low melting point and they form faster than the sulfides of chromium and aluminium. According to Deacon [26], sulfur compounds from the coal are transformed into highly corrosive gaseous H_2S.

1.2.2.1.4 Nitridation. Nitridation is the degradation process which occurs when metals and alloys are exposed to ammonia–bearing or nitrogen–base atmospheres at elevated temperatures [11]. According to Hurley [14], modeling indicates that at high temperatures, nickel can vaporize from alloys by forming nickel hydroxide gas ($Ni[OH]_2$). The gaseous nickel carbonyl $Ni(CO)_4$, which is a coordination compound where nickel atom is in a tetrahedral arrangement with four carbonyl groups, forms from $Ni(OH)_2$ gas at lower temperatures. Therefore, the transition from hydroxide to carbonyl involves reduction of Ni^{2+} to Ni^o. At equilibrium, nickel carbonyl formation can be expressed by the gas–phase reaction shown in Equation 1.2.4:

$$Ni(OH)_2 + 5CO \Rightarrow Ni(CO)_4 + CO_2 + H_2O \qquad (1.2.4)$$

$Ni(CO)_4$ easily decomposes to nickel and carbon monoxide in an inert gas at atmospheric pressure. Nitridation is much higher in N_2 gas as compared to NH_3 at temperatures between 980^oC and 1090^oC and is even more pronounced when the alloy is exposed to thermal cycling [16]. The nitridation process follows parabolic kinetics, indicating that the diffusion of nitrogen is the rate–controlling step. Kim *et al.* [27] also showed that selective dissolution and aggressive corrosion of nickel alloys occur in supercritical water if subcritical temperatures are reached. Kritzer *et al.* [28] reported that this aggressive corrosion is due to the

high solvency of subcritical water with respect to inorganic compounds.

1.2.2.1.5 Carburization. Also called carbon ingress, carburization is the material degradation process in which the base alloy reacts with carbon to form different forms of intermediate transition metal carbides, which are very reactive and can easily be hydrolysed by dilute acids or water. Gases containing carbon monoxide, methane, hydrocarbons, carbon and other carbonaceous compounds in high concentration in the outer porous oxide layers are the means by which high–carbon activities are generated at the alloy surface and carburization takes place. When there are some surface deposits preventing air from reaching the metal surface, the oxygen activity is reduced and carburization replaces oxidation at the alloy surface. Carbon attack is localized and confined to the pit. As a consequence, the material usually fails by embrittlement. Ardy *et al.* [29] recently showed that the failure of a cone burner at the tip–end results from the carburization from the combustion gas into material above 650^oC. Strong carbide former elements such as Cr, Mo, W and Fe react with carbon to form different carbides along the grain boundaries and within the grains. The formation of chromium carbide inhibits the protective oxides formation, making the base alloy more vulnerable to different types of corrosion. In the same manner, the formation of tungsten and molybdenum carbides reduces both the room temperature ductility of the base metal and its resistance to thermal shock.

1.2.2.2 Deposit–induced corrosion. In general, the corrosion of GT components mostly depends on the amount and composition of the impurity deposits on the surface. The general corrosion mechanism is attributed to the formation of low melting point ash deposits originating from certain trace metal impurities deposited the hot section parts of the system either by impaction or by condensation. These impurities include highly volatile elements such as Cl, Br, V, Hg, and S and moderately volatile elements such as As, Ge, Sb, B, F, Cd, Se, Zn and Sn [30, 31]. This form of corrosion often exhibits selective attack and internal oxidation. Selectively removed species move outward while vacancies move inward and eventually form voids [16]. As a consequence, corroded materials will generally fail under much less load compared to pristine samples. As the metal dissolves (oxidizes),

it can either form unstable/stable oxide layers or decompose immediately and go to vapor phase. In the following sections, attention is focused only on the highly volatile elements since they are more likely to induce corrosion of the hot parts due to the fact that they start in the vapor phase and condense later on the GT parts and initiate the corrosion process. According to Kawahara [32], the severity of the corrosion environments at the interface is influenced by the penetration extent of corrosive matters through deposits and scales.

   1.2.2.2.1 *Sulfidation attack.* Also called hot corrosion, sulfidation attack is defined as the accelerated oxidation of materials caused by the presence of a thin film of fused salt in a high temperature oxidizing gas environment. There are two types of hot corrosion: type I hot corrosion occurring at high temperature (between 800 and 950°C) and type II hot corrosion occurring at a lower temperature (between 650 and 800°C). The general attack mechanism has been extensively studied [13,16,18,33–35]. It mainly involves the formation of sodium sulfates through reaction with fuel sulfur and results in serious intergranular pitting of hot section components. It can also be generated by other sulphates such as K_2SO_4, $ZnSO_4$, $CaSO_4$, $CdSO_4$, $PbSO_4$, and $MgSO_4$ but this is very rare. The higher the salt deposit melting rate the higher the rate of base alloy corrosion [17,23,33]. Type I hot corrosion morphology is typically characterized by a thick, porous layer of oxides with the underlying alloy matrix depleted in chromium, followed by internal chromium–rich sulfides. Na_2SO_4 is the dominant salt found in the turbine blade deposits due to the thermodynamic stability of this compound in the presence of Na and S in an oxidizing gas [36]. The hot corrosion reaction proceeds in three stages: incubation, initiation and propagation [36]. The incubation step is characterized by low oxidation kinetics, the initiation step is marked by the failure of the protective oxide and a rapid corrosion follows (propagation step). According to Rapp [37], the mechanism of Ni–based alloys hot corrosion starts with Ni reacting with fused Na_2SO_4 to form liquid NiO causing the oxygen activity to decrease and the sulfur activity to increase. The formation of liquid nickel sulfide causes an increase in local salt basicity inducing the dissolution/fluxing of the normal protective NiO scale to form a basic solute of nickelate ions. With a negative solubility gradient, non–protective NiO particles

12

are precipitated within the salt film.

1.2.2.2.2   *Vanadium attack.* Vanadium is a naturally occurring component present as porphyrin in most crude oils and residual–grade fuel oils [13, 17, 18, 33, 38, 39]. As described by Bornstein [33, 38], vanadium attack starts with vanadium reacting with oxygen to form four major oxides: VO, V_2O_3, V_2O_4, and V_2O_5. The first three have a melting point of about 1500^oC while V_2O_5 has a melting point of about 670^oC. The low melting point of V_2O_5 makes it the only oxide liquid at most GT operating temperatures. The melted V_2O_5 quickly diffuses through the protective oxide and forms some vanadates with the base metal and vanadium is regenerated. The freed vanadium reacts with oxygen to form more V_2O_5, thus completing the cycle. The same author reported that the formed vanadates behave both as effective fluxes to remove protective oxides and as diffusion media which allow the rapid transport of oxygen to the metal surface. In marine environments, V_2O_5 also reacts with alkali sulfates to form condensed alkali–vanadates, which, in turn, prevent protective oxide formation thus enhancing the rate of depletion of the base metal. Vanadium–induced corrosion will be also accelerated in Mn–containing media, as Mn contributes to Na_2SO_4–V_2O_5 corrosion by interfering with the inhibiting effects of Mg and Si [40]. The Na_2SO_4–V_2O_5 compounds that result during combustion are semimolten and corrosive at metal temperatures normally associated with gas turbine operation.

1.2.2.2.3   *Bromine attack.* Bromine has a similar corrosion mechanism with chlorine. Bromine induced–corrosion starts with the formation of hydrobromic acid. Above this acid dew point, metallic bromine diffuses through the protective oxide and reacts with the base metal to form metal bromide. This metallic bromide reacts with oxygen and bromine is either released to the bulk gas or diffused back to the alloy–oxide interface and, like in chlorination, the cycle is completed and repeats itself several times [41, 42]. Hernas *et al.* [43] recently showed that the process of degradation of rotary air preheaters is intensified by the presence of bromine, whose sources are polybrominated diphenyl ethers (PDBEs) present in the biomass. PBDEs reach the environment due to the lack of chemical bonds with the matrix of the materials to which they are added. This was also confirmed by Vainikka *et*

al. [44], who added that Br originates from plastics in the form of brominated flame retardants, from the solid recovered fuel and wastewater sludge. Bromine initially vaporizes in the furnace and later forms waterwall deposits. In the presence of oxides and water at an elevated and high temperature, Br can be formed from KBr, which intensifies the corrosion process. Zhuang *et al.* [45] also showed using scanning electron microscopy (SEM), that a 40 ppm deposit of bromine on a metallic coupon surface results in small pitting, cracking, and blistering as well as a loss of Fe, Cr and Ni.

1.2.2.2.4 **Lead attack.** The mechanism of lead–induced corrosion proceeds through the disruption of the oxide film of the alloys as a result of the incorporation of lead. The protective film disruption is the beginning of stress corrosion cracking in the alloys. Chung *et al.* [46] demonstrated that the cracking was mainly intergranular in mode, between 60 and 450 μm in crack length and approximately 10^{-6} to 10^{-7} mm/s^{-1} in crack velocity. The modeling studies carried by Hurley [15] predicted that lead vaporizes primarily as PbS, with some lead metal, and condenses as PbS with a condensation temperature around 880°C. He added that the presence of chlorine increases the concentration of vapor phase lead as PbCl$_4$ at temperatures below 800°F, most significantly near 400°F, at which temperature approximately 1/10 of the lead may be in the vapor phase as PbCl$_4$. This was confirmed by Bankiewicz *et al.* [47], who reported that the lead–induced corrosion observed in AISI 347 exposed to PbCl$_2$ was due to the PbCrO$_4$ formation which decreased the protectiveness of Cr$_2$O$_3$. Zhang *et al.* [48] showed that 24 different base metals exposed to lead are all corroded by lead except Mo and Nb. Sakai [49] showed that the presence of lead increases the anodic polarization current in the passivity region, indicating the degradation of the passive oxide film followed by an accelerated anodic selective dissolution of the metal elements. Lu *et al.* [50], added that lead not only increases the critical current density in the polarization curve, it also increases the passive and transpassive current density. They further reported that the effect of lead on a steam generator corrosion becomes significant when the lead oxide concentration is between 10 and 100 mg/Kg and that the effect continues to increase with lead concentration above 100 mg/Kg.

1.2.2.2.5 ***Mercury attack.*** There are two types of mercury–induced corrosion: amalgam corrosion and liquid metal embrittlement. Amalgam corrosion occurs either in the presence of water and between 0^oC and the water dew point [51]. Therefore, any cryogenic warming of the heat exchanger or any unexpected plant shutdown will allow any trace of mercury present to concentrate in the heavier liquid phase (amalgam) and lead to the destruction of the base metal. The corrosion mechanism proceeds first with metal mercury adsorption on the base metal surface followed by an amalgamation with the metal [52–54]. Then the amalgamated base metal diffuses into the metal bulk causing stress corrosion by oxidizing electrochemically with water. Zerouali *et al.* proposed a simple attack mechanism for aluminum alloy AA 5083 corrosion induced by mercury (Equation 1.2.5 and Equation 1.2.6).

$$Al(Hg) + 3OH^- = Al(OH)_3 + Hg + 3e^- \tag{1.2.5}$$

$$Al(Hg) + H_2O = AlO_2^- + Hg + 4H^+ + 3e^- \tag{1.2.6}$$
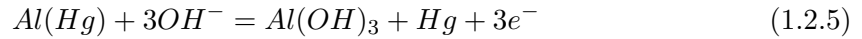
The liquid metal embrittlement involves the diffusion of mercury into the grain boundaries and resulting in cracks developing along the grain boundary. No air or water is needed once the corrosion process is initiated. Figure 1.7 shows a photomicrograph of mercury embrittlement on a failed heat exchanger [52].
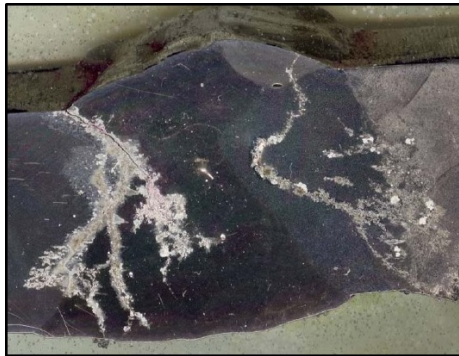
Figure 1.7: Liquid metal embrittlement failure on brazed aluminium heat exchanger [52].

1.2.3 Effects on the Mechanical Properties of the Base Metal

All of the above forms of high temperature corrosion reduce the cross–sectional area

of the component part, thereby increasing the stresses in the material. When trace metals like chlorine attack the base metal, the oxide layer is destroyed and there is an increase in mass loss over time. This mass loss results in a considerable reduction of the mechanical performance and high temperature strength of the material. For instance, in the sulfidation attack, a protrusion of oxide/sulfide forms from the alloy surface inward, acting to localize stress or to reduce the load–bearing section [16]. Palani *et al.* [55] reported that at 300^oC, lead contamination reduces the ultimate tensile strength as well as the elongation of the material. Pidaparti *et al.* [56] showed as the duration of a 5059 aluminum sample sensitization increases from 50 days to 74 days, the highest stress levels increase by about 56 %. As consequance, the creep and fatigue life are reduced as a result of notch formation in the base metal caused by different impurity attacks. Covino *et al.* [11] reported that these notches are either the precursors to fatigue cracks or assist in the growth of existing cracks. The same authors showed that the effect of hot corrosion is reduced at low stresses by plotting the time to rupture vs the applied stress for four different superalloys. The degradation in rupture life for Udimet 500 is shown in Figure 1.8. Figure 1.8 shows that there is a threshold stress level below which rupture life may become insensitive to hot corrosion

1.2.4   Cost, Evaluation, Testing and Prevention.

1.2.4.1   Cost. Corrosion–induced failures cost the United States many billions of dollars every year. A significant fraction of this cost could be avoided if people were well–educated on different corrosion prevention techniques. According to Virmani [58], studies carried out in several countries around the world from 1949 to 1995, predicted the total annual cost of corrosion to be in the range of 1 to 5 % of each country's gross domestic product (GDP). These costs include all the means used to control, prevent, and repair corrosion. This includes: replacement of corroded materials, salaries of corrosion engineers, money spent on inspection, maintenance, repairs, testing and prevention. Figure 1.9 shows results from a study done in 1998 by the Federal Highway Administration (FHWA) on the distribution of corrosion cost per category in the United States. The information provided in Figure 1.9 was obtained from publicly available government reports and from discussions with industry experts. The total cost of corrosion was estimated by determining the per-
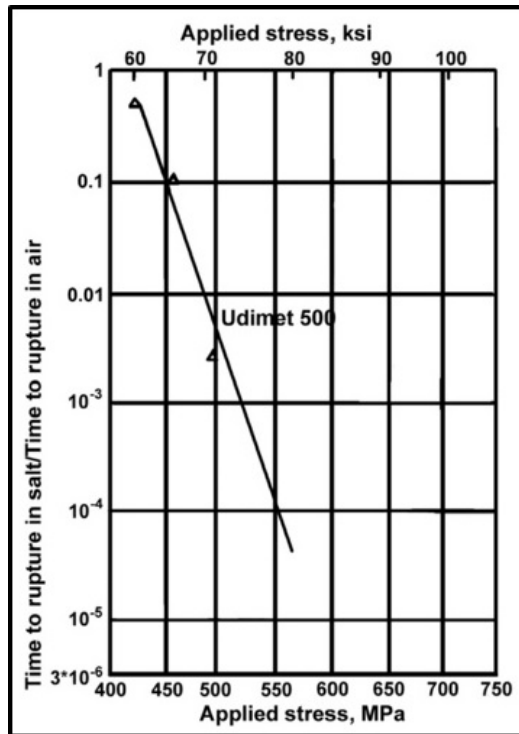
Figure 1.8: Degradation in rupture life for Udimet 500 due to hot corrosion at 705°C. [11,57].
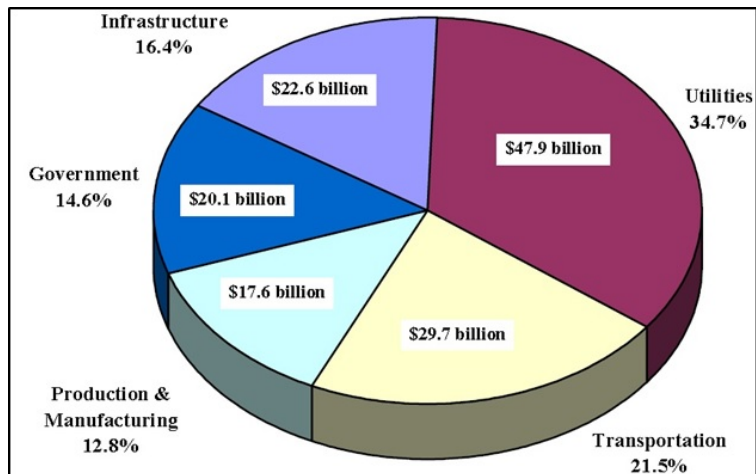
Figure 1.9: Cost of corrosion in sector categories analyzed in 1998 (total 137.9 billion US dollars/year) [58].

centage of the GDP of five sector categories, namely infrastructure, utilities, transportation, manufacturing and government, for which corrosion costs were estimated and numbers extrapolated to the US total GDP. From the extrapolations, the direct cost of corrosion in the U.S. was estimated in 1998 by the FWHA to equal 276 Billion dollars, which is about 3.1 % of GDP. But in their 2011 report, G2MT Laboratories estimated the total cost of corrosion in the United States to equal 993 Billions dollar in March 2013 and they estimated the same cost to exceed one trillion dollars in June 2013 [59].

1.2.4.2 Evaluation. One of the most important factors in evaluating corrosion damage in materials is the estimation of corrosion rate. Since corrosion will always occur as a results of the interaction of the material with its environment, it is crucial to know how fast or slow the material is likely to be be destroyed. According to Cramer [16], the average corrosion rate (CR) may be obtained from Equation 1.2.7.

$$CR = (K * W)/(A * T * D) \qquad (1.2.7)$$

Where K is a constant, T is the time of exposure in hours to the nearest 0.001 h, A is the area in cm^2 to the nearest 0.01 cm^2, W is the mass loss in grams to the nearest 1 mg, and D is the density in g/cm^3. The corrosion rate can also be expressed in years (converted from hours to years) but one must make sure of the uniformity of the corrosion rate before any conversion is done.

1.2.4.3 Testing. Laboratory testing procedures are used to screen metals and alloys for further testing and to develop data helpful to understanding corrosion processes. There exist several methods to test corrosion in the laboratory and each of these methods aims at simulating as close as possible the real–life environment of the corroded material. In the case of high–temperature corrosion, the corrosion resistance is tested using the following methods: furnace test, thermogravimetric analysis test, differential thermal analysis (DTA), differential scanning calorimetry (DSC), burner–rig test and molten–salt test. The last two methods are the most commonly used to test corrosion resistance in GT [8].

1.2.4.3.1 Burner–rig test. This test consists of burning the fuel of interest and impinging the exit gases onto a rotating spindle containing specimens of interest. The specimens are exposed directly to the hot gas in which some impurities have been added. The salt deposit is formed during testing as a result of the reaction with the hot gas. This method appears to be closer to real–world GT situation as compared to other corrosion testing techniques. But there are two disadvantages: 1– the equipment used is very expensive making this technique less available for a simple laboratory–testing scale (few organizations in the world can afford a burner–rig tester like NASA) and 2– the test is performed only at atmospheric pressure which is not always the case with GT engines. For instance, in aircraft propulsion, the engine experiences different pressures at idle, takeoff, climb and cruise.

1.2.4.3.2 Molten–salt test. In this test, a solution containing the desired corrosive species is sprayed onto a sample which is then heated. Upon heating, the solvent evaporates and the salt deposit remains on the surface of the sample which is then exposed to high temperatures to evaluate the level of damage caused by the deposited impurities. The test conditions are: temperature, density, electrolyte pH, and specific gravity. The sample exposure time can either be static or cyclic. In the static exposure, the sample is placed in the test apparatus and remains there until it is subjected to the total duration time specified. In cyclic exposure, the sample is subjected to a repeated sequence of timed conditions until a certain number of cycles is achieved. The fact that the amount and composition of salt deposit can always be controlled makes this method advantageous compared to the burner–rig test. Moreover, it is cheap, easy to conduct and can be repeated as many times as desired. This test is often used to compare the relative performance of metals and coatings to a standard known value for quality control purposes. It is a tool for evaluating the uniformity of thickness and degree of porosity of metallic and non–metallic protective coatings [16].

1.2.4.4 Prevention. Corrosion prevention can be achieved by different methods such as the use of corrosion inhibitors, protective coatings, material selection, engineering plastics and polymers, cathodic and anodic protection, corrosion control services, research

and development, education and training. But corrosion prevention in the case of GT mainly involves the first three techniques.

1.2.4.4.1 *Corrosion inhibitors.* Even though high–temperature corrosion is caused by impurities, some of these impurities can be beneficial in the sense that they can either slow down the degradation process or prevent it from happening. Zhang *et al.* [48] defined a corrosion inhibitor as a chemical substance that, when added in small concentration to an environment, effectively decreases the corrosion rate by forming a protective film which gives the surface a certain level of protection. For instance, magnesium can be added to the fuel to control vanadium attack by modifying the composition and melting point of the ash deposit. It combines with V_2O_5 to form magnesium orthovanadate (new ash component) which has a high melting point of about 1243^oF [33, 37, 40]. This high melting point allows the ash deposit to remain solid on gas turbine blades preventing corrosion from occurring. The added magnesium also forms magnesium sulfate which is water–soluble and which will be easily removed by periodic water washing of the hot gas path at the end of the process. Subramanian *et al.* [60] added that the introduction of magnesium causes the Mg^{2+} incorporated oxide to precipitate at the inner oxide solution interface. This precipitation restricts the egress of iron ions from the inner oxide solution interface and therefore alters the kinetics of the anodic reaction. Palani *et al.* [55] also added that dissolving magnesium species in the feed water reduces the incidence of lead–induced corrosion stress corrosion cracking (SCC) of Alloy 800, as $MgCl_2$ forms preferentiably to $PbCl_2$, thus reducing the lead contamination. Manganese and silicon have the same prevention mechanism as magnesium and can also be added in the place of magnesium for the same purpose. Adding silicon in a molten salt help reduce significantly the corrosion of stainless steels [61]. Chromium is added to help reduce ash fouling or increase the corrosion resistance of the material. The mechanism involves the formation of volatile compounds which pass through the turbine without depositing as they remain in the gas phase. Higher chromium ($\geq$23 %) is used for protection from low–temperature hot corrosion while higher aluminum ($\geq$ 8 %) is used for oxidation protection. Molybdenum is sometimes added to promote resistance to pitting

corrosion occurring at high temperature. Silicon, niobium, aluminium, tungsten and titanium can also be added to promote resistance to carburization [16]. The addition of rare earth elements such as lanthanum, cerium, yttrium improves the protective oxide adhesion and resilience to cyclic oxidation [11, 16].

1.2.4.4.2 *Protective coatings.* Protective coatings are protective barriers used to isolate GT components from the high temperature produced by the combustion of syngas. Protective coatings are the most commonly used techniques to protect the GT engine hot component sections against gas–induced and deposit–induced corrosions especially the high–temperature oxidation as well as the hot corrosion [62–64]. They are are used to protect the GT engine hot component sections against gas–induced and deposit–induced corrosions. There are three types of protective coatings: overlay coatings, diffusion coatings and ceramic overlay coatings. The first two are metallic bond coats (MBC) and are usually represented by MCrAlY where M stands for Ni, Co, Fe or a combination of two or more of these elements. The MBC is used for corrosion protection while the ceramic coating overlay is used for thermal protection of the first stage blading. The protective coating provides the corrosion and creep resistance while the base metal provides the mechanical strength at high temperature. The use of ceramics as TBCs is due to the fact that they possess very high creep strength and very low thermal conductivity (good insulators). The most common ceramic oxides used in GT part coatings include two or more of the following oxides: Y_2O_3, Al_2O_3, Cr_2O_3, SiO_2, Y_2O_3, MgO, CeO_2, CaO, $ZrSiO_4$, NiO, HfO_2, $NaVO_3$, and ZrO_2. The diffusion MBCs are applied using chemical vapor deposition (CVD) while the overlay MBCs are applied using vaccuum plasma spraying (VPS), atmospheric plasma spraying (APS), and high velocity oxygen fuel (HVOF). Ceramic coatings are applied using flame spraying (FS) or atmospheric plasma spraying (APS) or detonation gun spraying (DGS) or electron beam physical vapor deposition (EB–PVD). The coating thickness ranges from 100 to 1500 μm for ceramic coatings, from 20 to 100 μm for diffusion MBCs and from 150 to 500 μm for overlay MBCs [8].

1.2.4.4.3 ***Material selection.*** Material selection aims at achieving a desired performance and life expectancy of parts in service. The choice of a particular type of material must ensure: availability, lifetime, safety, cost, maintenance and fabrication as well as the the material properties with respect to the corrosive environment of interest. In the recent years, high–temperature materials development has become one of the most commonly used techniques to prevent high temperature corrosion. This new technique is been developed to remediate to the double failure effects encountered in commonly used TBCs. According to Immarigeon [62], the life of the overlay ceramic is limited by its susceptibility to thermal fatigue cracking while the life of the bond coat is limited by its oxidation and corrosion behavior. Most failures observed in TBCs manifest themselves as delamination at the interface between the bond coat and the ceramic top coat (Figure 1.10). The driving
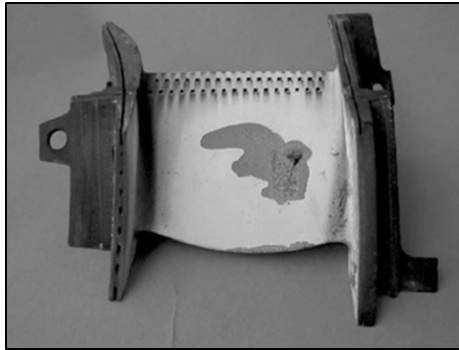
Figure 1.10: Failure of an EB–PVD YSZ/NiCoCrAlY thermal barrier coating on a service–exposed high–pressure vane of a commercial civil aero engine [63].

force for delamination arises from the temperature gradients set up during thermal cycling coupled with the difference in thermal expansion coefficients of the various constituents present [63]. Kawahara *et al.* [32] added that the temperature cycling was responsible of the spallation of the protective oxide. The material selection process for corrosion control mainly relies on the use of much more corrosion–resistant and high–temperature alloys such as nickel–based [2, 16], iron–based [2, 16, 65] and cobalt–based [66] ODS alloys such as APMT, or gamma prime–strengthened (GPS) alloys such as CM 247 LC and Rene 80 [2], and titanium alloys [16]. These types of materials are chosen because they are highly

corrosion/oxidation– and spallation–resistant materials, preserving most of their mechanical properties at high temperatures. They mostly form protective oxides and oxides formed have good adherence, high melting point, low vapor pressure, good high–temperature plasticity to resist fracture, low electrical conductivity and low diffusion coefficients for metal ions and oxygen. They can be used separately or in combination. ODS alloys and carbon–carbon composites are used in most applications in which strength must be conserved [66]. The good oxidation resistance of aluminides and silicides make them good candidates for high temperature systems requiring very high yield strength [67]. Titanium alloys are used primarily in the aerospace and the military industry, where the high strength–to–weight ratio and resistance to high temperatures are properties of interest while nickel–based alloys are used extensively in the oil production, refinery, and chemical processes industries, where conditions are severely corrosive [16].

The rest of the thesis is planned as follows:

- In chapter 2, data collected from the combustion of HHC syngas produced in pilot–scale coal–fired entrained–flow and fluidized–bed gasifiers will be analyzed in order to better understand realistic corrosion conditions inside HHC syngas–fired turbines and results will be presented.

- In chapter 3, force distributions in clamped structures will be modeled in order to optimize the joining process for any joint configuration. Based on this information, clamping methods to apply single plates of APMT to CM 247 LC and Rene 80 turbine structures will be developed and results will be presented.

- In chapter 4, a conclusion will be given as well as recommendations to be considered in the next steps of the project.

CHAPTER II

CHARACTERIZATION OF SYNGAS MICROCONTAMINANTS

2.1 Definition

Synthetic gas, commonly referred to as syngas, is a fuel gas mixture produced by means of partial coal combustion, at temperatures and pressures of 800 – 1050 ^oC / 25 bar using a fluidized–bed gasifier (FBG) or 1200 – 1600 ^oC / 25 bar using an entrained–flow gasifier (EFG). It mainly contains CO and H_2 as well as small amounts of H_2O (vapor), H_2S, N_2, CO_2 and CH_4 [30,68]. Syngas is highly combustible, especially when it has a high hydrogen content (HHC) and it is used to fuel internal combustion in gas turbines (GT). It is also used as an intermediate stage in the Fischer–Tropsch process to produce synthetic petroleum to be used as fuel or lubricant. Other production methods include steam reforming of natural gas (or liquid hydrocarbons) and gasification of biomass [68]. According to the US DOE Report of April 2013 on the advancements in coal gasification [1], the coal–derived syngas produced by integrated gasification combined cycle (IGCC) will contribute to about 30 % to the world energy generation in 2035. Therefore, a need for efficient and clean burning of coal is of great importance to the energy sector. Recent advancements of IGCC technologies are paving the way for syngas to become one of the most economically important fuels in the world. But there is a concern with the combustion of H_2–syngas in turbines because of the impurities obtained as byproducts of the combustion. These impurities are thought to be the agents responsible of the corrosion of the GT hot section parts [1, 2, 68–72].

2.2 Effects of Impurities in Coal Gasification

As mentioned earlier, one of the objectives of this work was to determine what microcontaminants are present in combusted and non–combusted HHC syngas that may contribute to corrosion of the GT hot section parts. The behavior of iron– and nickel–based alloys in coal–derived syngas systems is still not yet well–defined because of the unknown na-

ture of the gas stream constituents. As a consequence, the corrosion mechanism is strongly influenced by the composition of coal–derived syngas, which itself depends on several factors such as coal composition, type of gasifier used, and gas stream cleanup technique [1, 2, 68]. These factors define the types and concentrations of syngas microcontaminants whose role in GT high temperature corrosion is not well–known. The stainless steel pipes used to transport syngas have recently been thought by Hurley *et al.* [2] to be a possible source of other microcontaminants observed in the HHC coal–derived syngas.

2.2.1 Type of Coal used

Sampling for this work was done at the UND–EERC from January 2012 to November 2013. During this period, three sets of sampling were done, the first one from March to July 2012, the second one in March 2013 and the third one from October to November 2013. Three types of coal were used: Montana Rosebud Subbituminous, Wyoming Eagle Butte and Wyoming Antelope dried. The nominal ash compositions of these three types of coal are shown in Table 2.1. Because of the high silica, alumina and calcium oxide contents in these three types of coal, many studies report silicon–rich, aluminum–rich and calcium–rich contaminated syngas despite the different removal techniques used [1, 2, 68]. A gasifier firing the Wyoming Eagle Butte or the Wyoming Antelope coal is expected to produce more sulfur–contaminated syngas as compared to the Montana Rosebud coal which does not contain any sulfur–related compounds. It is also expected to have high aluminum and sodium contents in the syngas produced when firing the Eagle Butte as it contains more aluminum– and sodium–related compounds than the Montana Rosebud. Since none of these coal contains manganese, any trace detected in the syngas would be coming from external sources.

2.2.2 Type of Gasifier used

The UND–EERC has several types of gasifiers. These include: a 1–MW transport reactor development unit gasifier, a high–pressure fluid–bed gasifier (HP–FBG), a low–pressure continuous Fluid–bed Reactor, an entrained–flow gasifier (EFG), a fixed–bed gasifier, a mild gasification carbonizer and a small laboratory–scale fixed–bed gasifier reactor. Only the EFG (Figure 2.1) and HP–FBG (Figure 2.2) were used in this work for sampling purposes.

Table 2.1: Ash Compositions of the Wyoming Eagle Butte, Montana Rosebud Subbituminous and Antelope dried Coals (wt%) [69–72]

Oxide	Eagle Butte	Montana Rosebud	Antelope dried
Na_2O	2.50	0.40	1.47
MgO	7.20	7.90	7.14
Al_2O_3	17.20	14.30	13.55
SiO_2	32.40	54.7	24.82
K_2O	0.30	0.50	0.17
CaO	31.10	17.9	26.68
TiO_2	1.00	0.70	1.39
MnO	≤ 0.1	-	-
Fe_2O_3	8.10	3.40	7.52
SO_3	13.50	-	16.33
P_2O_5	-	0.20	0.90

Other equipment typically used in gasification systems could include a Fischer–Tropsch reactor Skid, a warm–gas cleanup train, a large hot–gas filter vessel, a bench–scale hot–gas filter vessel, a sulfur reactor, and a hydrogen separation membrane. EFG is currently the most used gasifier in coal–derived electricity generation due to its high operating temperature of about 1500^oC [2]. These conditions assure complete coal conversion, low tar formation, and the creation of a low–leachability slag from the majority of the ash–forming constituents. But the drawback here is that at high temperatures most ash–forming constituents initially present in the coal all go into vapor phase and will later condense on the GT blades during the cooling and thereby initiate the deposit–induced corrosion. This applies to the most highly volatile elements such Cl, Br, V, Hg, Si, Al and S, which are most likely to be present on turbine blades at cooler temperatures. Hurley *et al.* [70] reported that lower–rank coals contain oxygen functional groups such as carboxylic acids which can exchange with ions in groundwater to take on many different metals, especially alkali and alkaline–earth elements. The authors added that during conversion of the coal, these elements can also reach the vapor phase, which then condenses on other surfaces or forms gas–entrained submicron particulates. The HP–FBG has two main advantages: easy control of temperature and great ability to deal with very fine grained materials without the need of pre–processing.

Figure 2.1: Photograph of the EERC Entrained–Flow Gasifier used.

The temperature can be kept below the melting or fusion point of the ash to avoid harmful processes such as sulfidation attack which are mainly due to the formation of low melting ashes. When using FBGs, instability of the bed and fly–ash sintering in the gas channels appear to be the most common problems occuring when firing biomass fuels [73]. The HP–FBG produces a high tar content as well as an incomplete carbon burn–out, and has a poor response to load changes. The lower running temperatures of FBG makes it produce more CH_4 as compared to the EFG. The FBG also produces hydrocarbons and trace organics whose nature and composition are largely dependent on the fuel type and operational parameters. The N_2 purge requirements of the FBG are substantially lower than for the EFG, resulting in much lower N_2 dilution of approximately 3% of the dry gas, which means less possibility of gas contamination [73].

2.2.3 Type of Cleaning Techniques

GT cleaning aims at removing any contaminant (particulate matter) from the syngas before it can be sent to the GT combustion chamber. There are currently two main types

Figure 2.2: Photograph of the EERC high–pressure FBG.

of gasifier equipments cleaning: warm– and cold–gas cleanup methods [74]. There is a third method which consists of removing any contaminant from the coal to acceptable levels before it can be fed into the gasifier. The warm–gas cleanup is performed on the hot gas while the cold–gas cleanup is performed on a cooled syngas. Cold–gas cleanup requires the syngas to be cooled to lower temperatures, cleaned and then reheated. The cooling and reheating step contributes to a loss of thermal efficiency of the GT as additional steam is needed for the reheating process. The current commercially available cold–gas cleanup techniques really do a good job but the problem is that they are very expensive. Therefore any warm–gas cleanup technique will help to significantly reduce this efficiency loss and improve the powerplant thermal efficiency and commercial viability. High temperature capture of the trace elements in one step will reduce the footprint, cost, and complexity of the pollution mitigation method and will also increase the certainty of the final disposition of the trace elements [68]. Despite the fact that all these methods are very good at removing large particulate matter from the gas stream, they sometimes fail to remove submicron particles which have a high probability of reaching the GT combustor and causing severe corrosion of the hot section parts. The major issue here is that until today, very few data are available on the nature and composition of these submicrons particles as well as their role in the GT

component corrosion process. Although the syngas entering the turbine is expected to be clean as demanded by GT manufacturers, it is very important to understand the level of syngas trace metals contaminants to reallistically assess the conditions of safe operation [75].

2.3   Syngas Characterization Techniques

Microcontaminants sampling consists of collecting particulate– and vapor–phase elements using two sampling trains, one each designed for the US Environmental Protection Agency (EPA) methods for halogen sampling (M26–A) and trace metals sampling (M29). The sampling train consists of a one–piece glass nozzle/probe liner, a large particulate cyclone, the polycarbonate filter (Whatman Nuclepore type with a melting temperature of 250°C), followed by a series of impingers (five for M26–A and six for M29), shown in Figure 2.3. Impingers are of a standard Greenburg–Smith design type and are connected in series with leak–free ground brass fittings. While filter–trapped particulate matters are analyzed using scanning electron microscopy (SEM) for their morphology (shape and size), impinger solutions major and trace elements are analyzed using different spectroscopic techniques such as cold–vapor atomic absorption spectrometry (CVAAS) and inductively coupled plasma–mass spectrometry (ICP–MS). A target trace metal emission will be detected only if its concentration is above the corresponding lower limit of quantification (LLQ) of the spectrometer. At the beginning of each sampling, a pretest leak check is done and the initial meter volume is recorded. For each run, the required data are recorded on a data sheet. When the desired amount of gas is collected, the glassware is disconnected and the
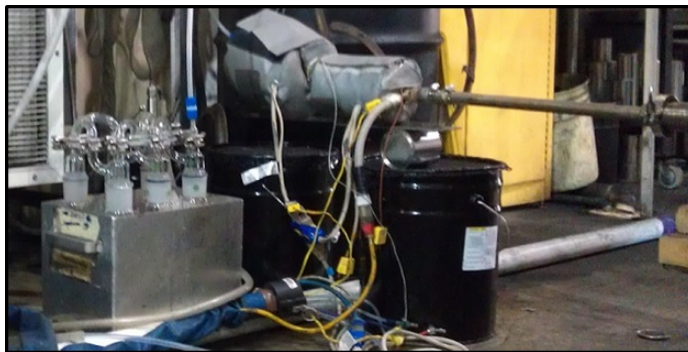
Figure 2.3: EPA Sampling train used for M26–A and M29.

contents of the acid impingers are poured into leak–free storage bottles. Each impinger is rinsed with water, and the rinse is added to the corresponding storage bottle. All sample collection bottles are sealed, labeled, and sent to the analytical laboratory for minor elements detection.

2.3.1   Sample collection

2.3.1.1   EPA Method 29 M29 is applicable to the determination of EPA–designated hazardous metal emissions such as Pb, Ni, Mn, Hg, Se, Cd, Cr, Ag, Tl, As, Sb, Ba, Be, Co, P, Zn, and Cu from stationary sources [76]. A stack sample is withdrawn isokinetically from the source. Particulate emissions are collected in the probe and on a heated filter while gaseous emissions are collected in aqueous acidic solutions of H_2O_2 and $KMnO_4$. The sampling train, whose schematic is shown on Figure 2.4, consists of a one–piece glass nozzle–probe liner, a large particulate cyclone, a polycarbonate filter (Whatman Nuclepore type with 0.1 μm holes), followed by a series of six impingers. Impingers are of a standard Greenburg–Smith design–type and are connected in series with leak–free ground brass fittings. The first and second impingers contain 150 mL each of the mixture HNO_3–H_2O_2 (5% HNO_3 and 10% H_2O_2), the third impinger is empty, the fourth and fifth impingers both contain 150 mL of the mixture H_2SO_4–$KMnO_4$ (4% $KMnO_4$ and 10% H_2SO_4), and the sixth impinger contains about 350 g of pre–weighted silica gel. The mixture HNO_3–H_2O_2 is used to trap all the trace metals (including the oxidized form of mercury) that have gone through the filter's pores, while the H_2SO_4–$KMnO_4$ mixture is used to trap the elemental form of mercury.

2.3.1.2   EPA Method 26–A M26–A is applicable for the determination of hydrogen halide (HCl, HBr, and HF) and halogen (Cl_2 and Br_2) emissions from stationary sources. The impinger solutions are analyzed by ion chromatography (IC), which detects and quantifies the amount of F^-, Cl^-, and Br^- in these solutions. The concentration of a target hydrogen halide or halogen emission in solution is suggested to be greater than the corresponding LLQ to be detected by the IC system. The minimum detection limit for bromide, chloride, and fluoride is 1 mg/L, using the EERC equipment for M26–A. The first and second impingers each contain 100 mL of 0.1 N H_2SO_4. The third and fourth impingers
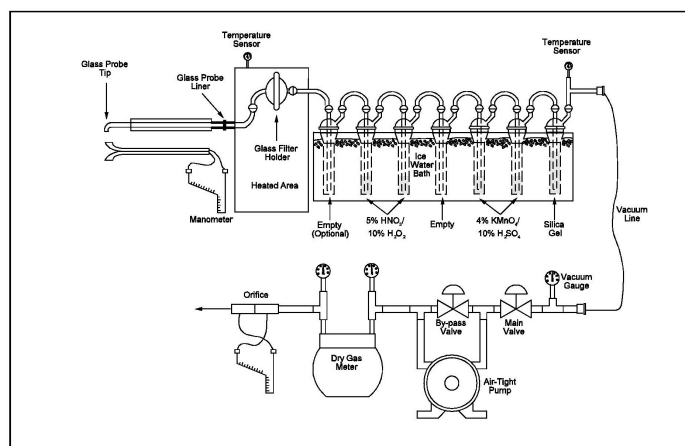
Figure 2.4: Schematic of the sampling train used for M29 method [76].

contain 100 mL of 0.1 N NaOH. The fifth impinger contains about 350 g of silica gel. The H_2SO_4 solution is used to solubilize hydrogen halides that have been vaporized to the gas phase, while the NaOH solution is used to hydrolyze halogens (Cl_2, Br_2) into protons (H^+), halide ions, and hypohalous acids (HClO and HBrO). Then Na_2SO_4 is added to the alkaline solution to assure reaction with the hypohalous acid to form a second halide ion such that two halide ions are formed for each molecule of halogen gas.

2.3.2 Sample analysis

2.3.2.1 Cold–vapor atomic absorption spectrometry This technique as described in Reference [77], is used to measure the elemental form of mercury. Mercury is chemically reduced to the free atomic state by reacting the sample with a strong reducing agent like stannous chloride or sodium borohydride in a closed reaction system. The volatile free mercury is then driven from the reaction flask by bubbling air or argon through the solution. Mercury atoms are carried in the gas stream through tubing connected to an absorption cell, which is placed in the light path of the atomic absorption spectrometer. Sometimes the cell is heated slightly to avoid water condensation but otherwise the cell is completely unheated. As the mercury atoms pass into the sampling cell, measured absorbance rises indicating the increasing concentration of mercury atoms in the light path. Some systems allow the mercury vapor to pass from the absorption tube to waste, in which

case the absorbance peaks and then falls as the mercury is depleted. The highest absorbance observed during the measurement will be taken as the analytical signal. In other systems, the mercury vapor is rerouted back through the solution and the sample cell in a closed loop. The absorbance will rise until an equilibrium concentration of mercury is attained in the system. The absorbance will then level off, and the equilibrium absorbance is used for quantitation.

2.3.2.2 Inductively coupled plasma–mass spectrometry Inductively coupled plasma–mass spectrometry (ICP–MS) is a technique for trace element analysis in water, minerals, and rocks [77]. It has the ability to detect very low levels (parts per billion) of most elements in a sample. The dynamic range is typically ten orders of magnitude and data reduction is relatively simple. Rapid data acquisition and data reduction enable the measurement of large numbers of samples in a short period of time.

2.3.2.3 Scanning Electron Microscopy SEM is a microscopy technique which uses electrons ejected from a specimen to form a magnified image. These electrons are ejected as a result of the sample being hit by a beam of electrons produced in a vaccuum at the top of the microscope by an electron gun and sent down through a series of electromagnets and lenses. This hit produces different types of electrons such as auger, secondary and backscattered electrons as well as X–rays, which are then collected on a specific detector located above the specimen. The UND–EERC SEM system is an automated JEOL 5800 equipped with Oxford Instruments INCA EDS system and a silicon drift x–ray detector. Specimen preparation begins with filters being removed from the sampling train (Figure 2.3) and directly kept in a desiccator (Figure 2.5). They are removed later at an appropriate time for full analysis. Small pieces of each filter are cut off, carbon– or gold–coated for better quality images, and then mounted with double–stick tape on a graphite plug. The coated specimen and the plug are both inserted into the SEM analysing chamber and the microscope is turned on. Particles are analyzed and spectra acquired for 20 s using a 2 nA beam current at 20 kV accelerating voltage. Several spots will be chosen at random on the filter surface and submitted to a full spectral analysis.

Figure 2.5: EERC Desiccator used to keep filter samples.

2.4 Syngas Analysis Results

The sampling parameters for the three sets of samples collected in this work are shown on Table 2.2, Table 2.3 and Table 2.4. Syngas analysis results presented in the following sections carry on the first two sets of samples. The results of the third set will be presented in the future. The Montana Rosebud subbituminous coal was mixed with between 5% and

Table 2.2: Sampling Parameters for the first Sampling Set

Parameter	Date	Duration	Volume	Fuel	Port	Gasifier	EPA
Test-1-2012	3/27/2012	221 min	34.48 ft3	Natural gas	outlet	EFG	M29
Test-2-2012	3/28/2012	150 min	43.66 ft3	Rosebud	outlet	EFG	M29
Test-3-2012	3/30/2012	217 min	63.68 ft3	Natural gas	outlet	EFG	M29
Test-4-2012	4/11/2012	223 min	60.68 ft3	Rosebud	outlet	FBG	M29
Test-5-2012	4/11/2012	60 min	09.20 ft3	Rosebud	outlet	FBG	M26–A
Test-6-2012	4/18/2012	150 min	40.29 ft3	Rosebud	outlet	FBG	M26–A
Test-7-2012	7/10/2012	185 min	44.50 ft3	Rosebud	outlet	EFG	M29

15% of ground pelletized wood and no sulfur removal was used during the first sampling period. During the second sampling period no M26–A sample was collected as no halogen or halide were found in the previous samples analysis. The second set was conducted in order to double check some discrepancies and inconsistencies observed in the previous sampling. In fact, it was thought that some trace metals observed in the combusted syngas did not

Table 2.3: Sampling Parameters for the second Sampling Set

Parameter	Date	Duration	Volume	Fuel	Port	Gasifier	EPA
Test-1-2013	3/12/2013	210 min	54.47 ft3	Eagle Butte	inlet	FBG	M29
Test-2-2013	3/13/2013	218 min	35.38 ft3	Eagle Butte	outlet	FBG	M29
Test-3-2013	3/13/2013	30 min	09.60 ft3	Eagle Butte	inlet	FBG	M29
Test-4-2013	3/15/2013	85 min	23.78 ft3	Eagle Butte	outlet	FBG	M29

Table 2.4: Sampling Parameters for the third Sampling Set

Parameter	Date	Duration	Volume	Fuel	Port	Gasifier	EPA
Test-5-2013	10/29/2013	168 min	56.75 ft3	Antelope	outlet	EFG	M29
Test-6-2013	10/30/2013	120 min	49 ft3	Antelope	inlet	EFG	M29
Test-7-2013	11/4/2013	171 min	47.5 ft3	Natural gas	outlet	EFG	M29

come from the combustion but rather from the rust present on the inside walls of the TOx as shown in Figure 2.6. As a result, the thermal oxidizer (TOx) was thoroughfully cleaned on February 25, 2013 before the sampling period of March 2013 and a decision was also made to sample at the TOx inlet for a meaningful comparison.

2.4.1 Impinger Solution Samples

Analytical results for EPA hazardous emission elements are presented in Table 2.5, Table 2.6, Table 2.7, Table 2.8, and Table 2.9 according to their respective sampling dates. The concentration of each element is given for the solution analyzed and for the gas volume that was sampled. Concentrations are expressed in $\mu g/L$ for the first and third row (U–1) and in $\mu g/m^3$ for the second and fourth row (U–2) of each table.

Table 2.5: Test 2–2012, Sample I.D.: EFG–039–M29, Test Length: 150 min, VmSTD: 43.666 ft^3, Fuel: Montana Rosebud subbituminous coal

	Conc.	As	Pb	Hg	Sb	Ni	Mn	Se	Be	Cd	Co	Cr
H_2O_2	U–1	LLQ	1.9	0.15	2	58.7	20.8	LLQ	0.2	18.8	LLQ	48.6
	U–2	LLQ	0.77	0.06	0.81	23.8	8.42	LLQ	0.08	7.61	LLQ	19.7
$KMnO_4$	U–1			3.55								
	U–2			1.44								

In these tables, the nozzle results are absent because no nozzle was used in this work. The oxidized form of Hg is shown in the H_2O_2 solution while its elemental form is shown

Figure 2.6: Rust removed from the bottom of the thermal oxidizer.

Table 2.6: Test 3–2012, Sample I.D.: EFG–039–M29, Test Length: 217 min, VmSTD: 63.684 ft^3, Fuel: natural gas

	Conc.	As	Pb	Hg	Sb	Ni	Mn	Se	Be	Cd	Co	Cr
H$_2$O$_2$	U–1	LLQ	1.2	0.13	LLQ	12.8	13.3	2.2	0.2	0.2	LLQ	9.82
	U–2	LLQ	0.33	0.04	LLQ	3.55	3.69	0.61	0.06	0.06	LLQ	2.72
KMnO$_4$	U–1			0.138								
	U–2			0.04								

Table 2.7: Test 4–2012, Sample I.D.: FBG–025–M29, Test Length: 223 min, VmSTD: 60.681 ft^3, Fuel: Montana Rosebud subbituminous coal

	Conc.	As	Pb	Hg	Sb	Ni	Mn	Se	Be	Cd	Co	Cr
H$_2$O$_2$	U–1	LLQ	0.76	0.16	LLQ	7.53	63.8	1.1	0.2	0.2	LLQ	8.2
	U–2	LLQ	0.22	0.05	LLQ	2.19	18.58	0.32	0.06	0.06	LLQ	2.39
KMnO$_4$	U–1			0.839								
	U–2			0.29								

Table 2.8: Test 5–2012, Sample I.D.: FBG–025–M26, Test Length: 60 min, VmSTD: 9.198 ft^3, Fuel: Montana Rosebud subbituminous coal

	Chloride, ppm	Fluoride, ppm	Bromide, ppm
H$_2$SO$_4$ in Flue Gas	1.3	2.3	LLQ
NaOH in Flue Gas	LLQ	LLQ	LLQ

Table 2.9: Test 6–2012, Sample I.D.: FBG–025–M26, Test Length: 150 min, VmSTD: 40.294 ft^3, Fuel: Montana Rosebud subbituminous coal

	Chloride, ppm	Fluoride, ppm	Bromide, ppm
H$_2$SO$_4$ in Flue Gas	LLQ	LLQ	LLQ
NaOH in Flue Gas	LLQ	LLQ	LLQ

in the KMnO$_4$ solution. Test 1–2012 results are not presented here because a lot of rust was found on the filter and the sample was discarded from data analysis. A part of the filter melted during Test 2–2012 and most of the solid particles went into the impinger solutions but the decision was made to analyze the impinger solution sample to determine what portion of the particulate matter went into solution. Any value below an element LLQ was classified as *non–detected* and labeled in the tables as LLQ while the remaining values were classified as *detected* since they were above the elements LLQ and were well–quantified. The LLQ values of the different elements investigated are shown in Table 2.10.

Table 2.10: Limit of detection of trace metals analyzed

Trace Metal	As	Be	Cd	Co	Cr	Mn	Ni	Pb	Sb	Se	Hg
LLQ, μg/L	0.5	0.1	0.1	0.5	0.1	0.1	0.2	0.1	0.1	1	0.02

2.4.2   Filter samples

Figure 2.7, Figure 2.8 and Figure 2.9 show SEM images of the filters and the randomly spots chosen in Test 3–2012, Test 4–2012 and Test 7–2012, respectively. The spectra of these spots are shown in Table 2.11, Table 2.12 and Table 2.13.

Analyses of the different samples show major elements Fe, S, Cr, Si and Ni on the filter surfaces as well as minor elements Pb, Hg, Sb, Ni, Mn, Se, Be, Cd, Cr in impinger solutions. The initiative to collect samples at the TOx inlet came into play to have a clear idea on which microcontaminant was present in the non–combusted syngas as well as what happens during combustion. Figure 2.10, Figure 2.11, Figure 2.12 and Figure 2.13 show SEM images of the filters and the respective randomly spots chosen in Test 1–2013, Test 2–2013, Test 3–2013 and Test 4–2013. The spectra of these spots are not shown here because elements found on the filters were similar to those found in 2012. Comparative SEM images

Figure 2.7: Spots chosen from Test 3–2012 for full spectral analysis.

Figure 2.8: Spots chosen from Test 4–2012 for full spectral analysis.
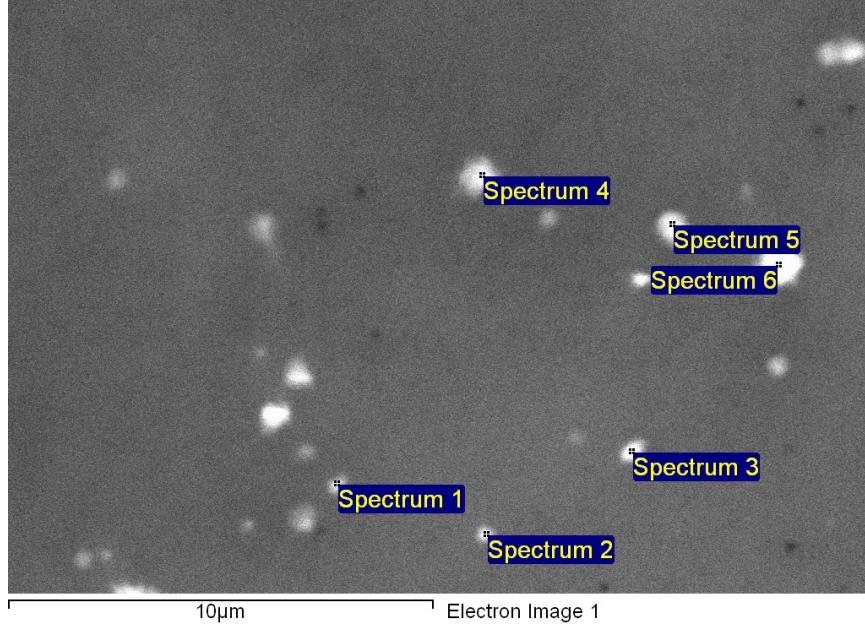
Figure 2.9: Spots chosen from Test 7–2012 for full spectral analysis.

Table 2.11: Spectral compositions in wt% of the spots chosen from Test 3–2012 filter

	O	Si	S	Cr	Fe	Ni	Total
Spot 1	48.88	1.89	6.79	5.42	33.66	3.35	100
Spot 2	61.84	0.00	7.16	4.17	26.82	61.84	100
Spot 3	54.78	0.00	4.45	8.07	32.69	0.00	100
Spot 4	79.04	0.00	5.78	0.00	15.19	0.00	100
Spot 5	100	0.00	0.00	0.00	0.00	0.00	100
Spot 6	100	0.00	0.00	0.00	0.00	0.00	100
Spot 7	100	0.00	0.00	0.00	0.00	0.00	100
Max.	100	1.89	7.16	8.07	33.66	3.35	
Min.	48.88	1.89	4.45	4.17	15.19	3.35	

Table 2.12: Spectral compositions in wt% of the spots chosen from Test 4–2012 filter

	O	Si	S	Cr	Fe	Ni	Total
Spot 1	63.8	3.7	19	2.1	11.4	0.0	100
Spot 2	62.7	2.7	19.4	2.0	12.1	1.1	100
Spot 3	70.3	0.0	17.3	0.0	12.5	0.0	100
Spot 4	65.5	3.3	18.1	2.5	10.6	0.0	100
Spot 5	72.5	0.0	17.1	0.0	10.4	0.0	100
Max.	72.5	3.7	19.4	2.5	12.5	1.1	
Min.	62.6	2.7	17.1	2.0	10.4	1.1	

Table 2.13: Spectral compositions in wt% of the spots chosen from Test 7–2012 filter

	O	Si	S	Cr	Fe	Ni	Total
Spot 1	73.63	11.94	5.57	0.00	8.87	0.00	100
Spot 2	73.9	6.87	9.36	0.00	9.87	0.00	100
Spot 3	74.76	0.00	13.67	0.00	11.57	0.00	100
Spot 4	67.15	0.00	12.86	0.00	19.99	0.00	100
Spot 5	70.35	0.00	11.10	0.00	18.55	0.00	100
Spot 6	67.26	0.00	13.00	0.00	17.94	0.00	100
Max.	74.76	11.94	13.67	0.00	19.99	0.00	
Min.	67.15	6.87	5.57	0.00	8.87	0.00	

of Test 2–2013 and Test 3–2013 particles are shown on Figure 2.14 (a) for the inlet and on Figure 2.14 (b) for the outlet of the TOx.
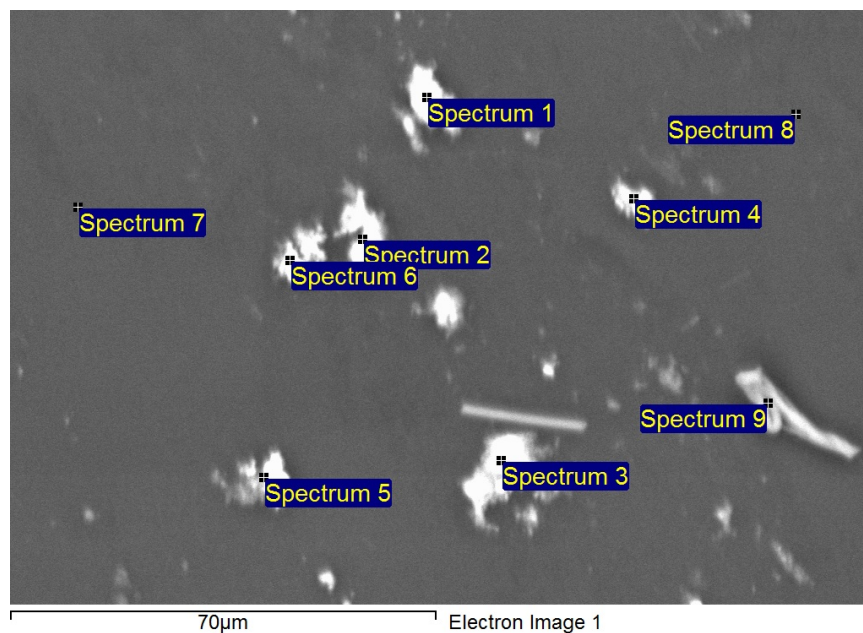
Figure 2.10: Spots chosen from Test 1–2013 for full spectral analysis.

2.4.3 Discussion

As seen from Table 2.5, Table 2.6 and Table 2.7, when only natural gas was being fired (e.g. Test 3–2012) all of the hazardous elements analyzed for the M29 test matrix were present in the gas collected from the TOx except As and Co. It was not known if these trace metals get into the TOx from the air injected earlier or if they were contaminants
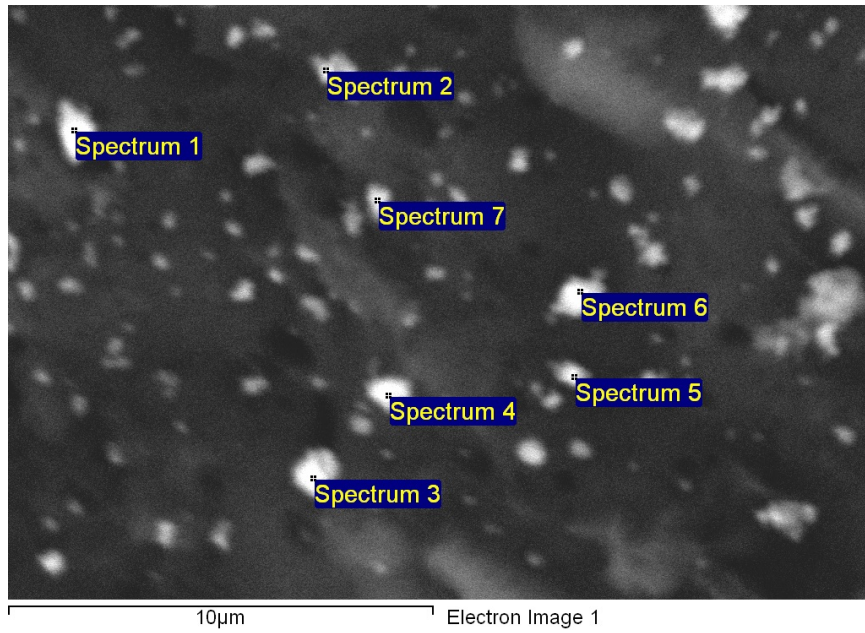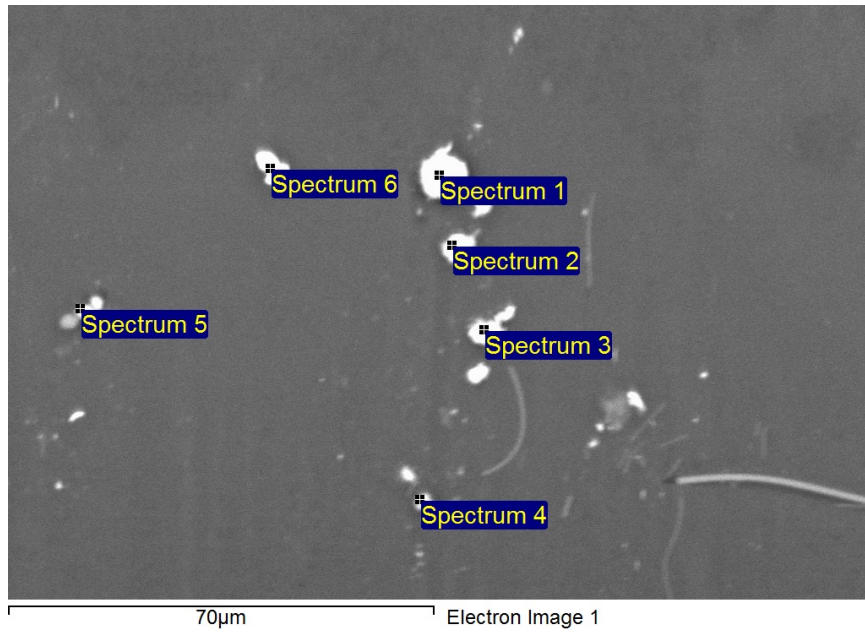
Figure 2.11: Spots chosen from Test 2–2013 for full spectral analysis.
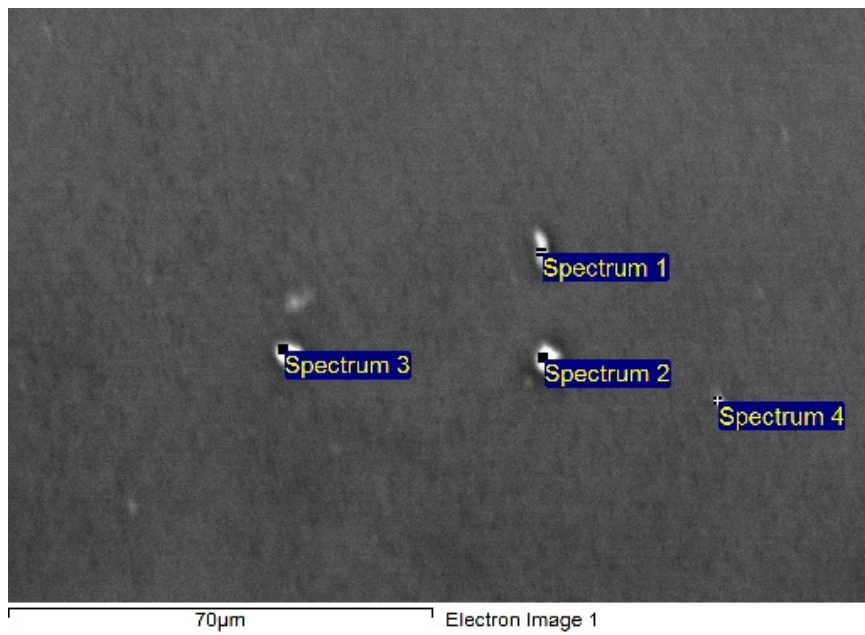
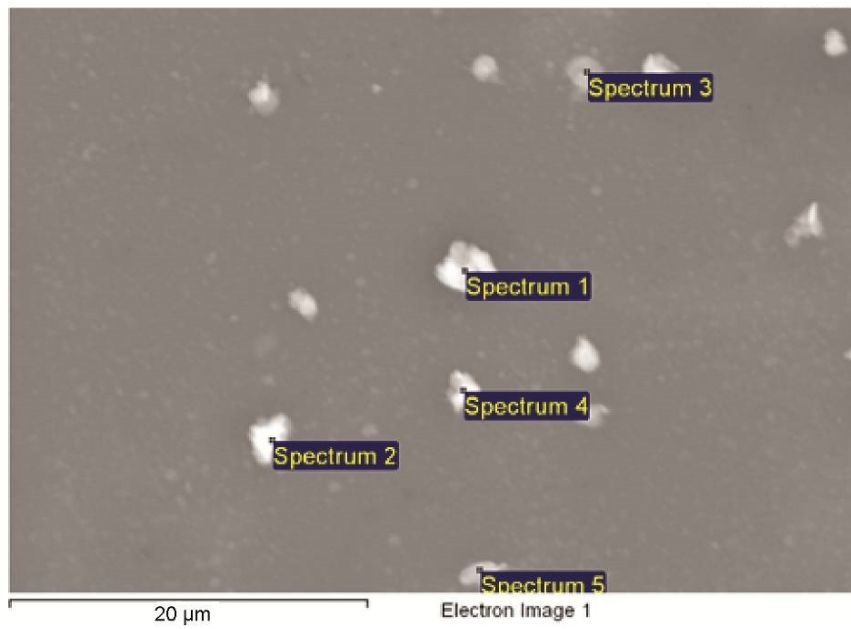Figure 2.12: Spots chosen from Test 3–2013 for full spectral analysis.
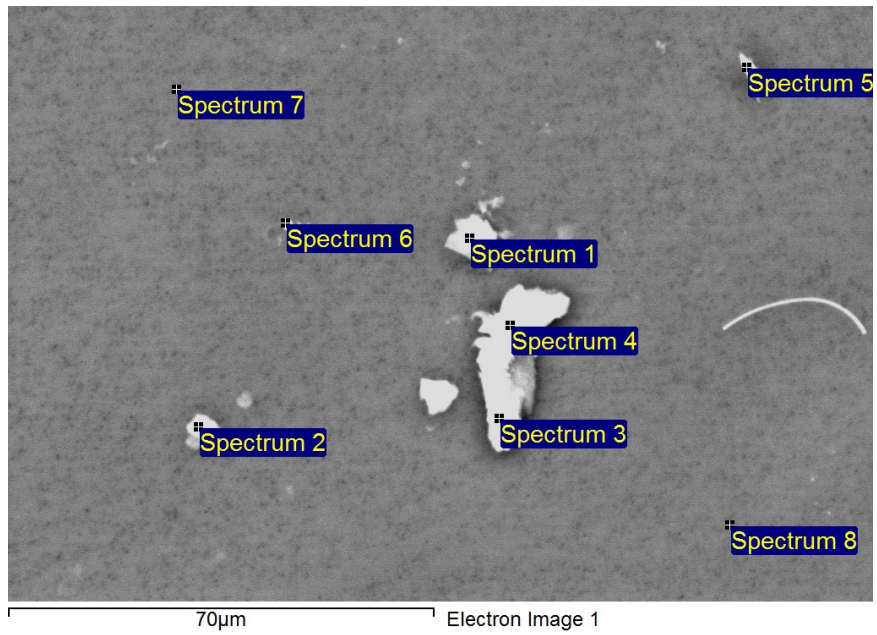
Figure 2.13: Spots chosen from Test 4–2013 for full spectral analysis.


(a) Inlet (Test 2–2013)

(b) Outlet (Test 3–2013)
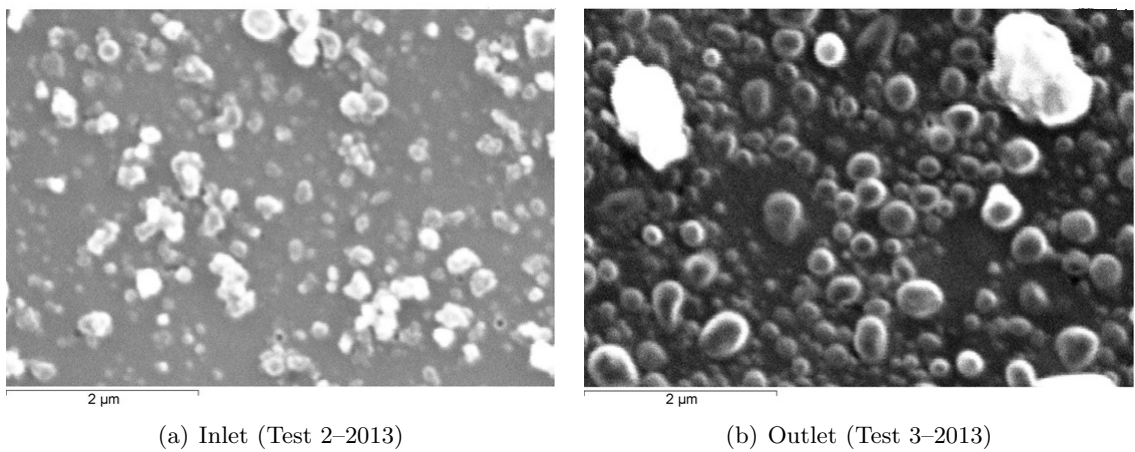
Figure 2.14: SEM images of particles collected from Test 2–2013 and Test 3–2013

previously deposited in the TOx. However, when syngas was fired (e.g. Test 4–2012) the amount of Mn in the gas stream increased substantially. Recalling that none of the coal used had a Mn content led to the conclusion that the Mn present on the filter came from a different source. A comparison between Test 2–2012 and Test 4–2012 reveals much higher Ni and Cr concentrations in Test 2–2012 solution. It is believed that either the EFG produced more of those elements in the syngas than the FBG did or that those elements were in the particulate matter that would normally be collected by the filter but were not separated in Test 2–2012 because the filter had melted. Table 2.8 and Table 2.9 show that halogens (Br_2, Cl_2) and hydrogen halides (HF, HCl, HBr) of concern were not present at any level above the detection limits of the ICP–MS used. This explains the reason why there was no M26–A sample collected during the 2013 sampling period. A comparison between Table 2.12 and Table 2.13 shows no trace of Cr nor Ni when firing the Montana coal, meaning that the EFG probably produced these elements in quantities below the LLQ and they could not be detected.

Table 2.14: Shape factor category distribution of 2012 particles

Shape	Spherical	Rectangular	Total
Test 3-2012	364	548	912
Test 4-2012	1648	1441	3089
Test 7-2012	719	294	1013

Table 2.15: Shape factor category distribution of 2013 particles

Shape	Spherical	Rectangular	Total
Test 1-2013	834	171	1005
Test 2-2013	588	425	1013
Test 3-2013	932	68	1000
Test 4-2013	686	325	1011

SEM analysis of the 2012 and 2013 samples shows that the particulate matters are primarily non–stoichiometric iron and chromium sulfates. At a first glance it can be seen that the iron weight percent remained high during both sampling periods. It was initially thought that the high Fe content in combusted syngas was coming from the rust formed
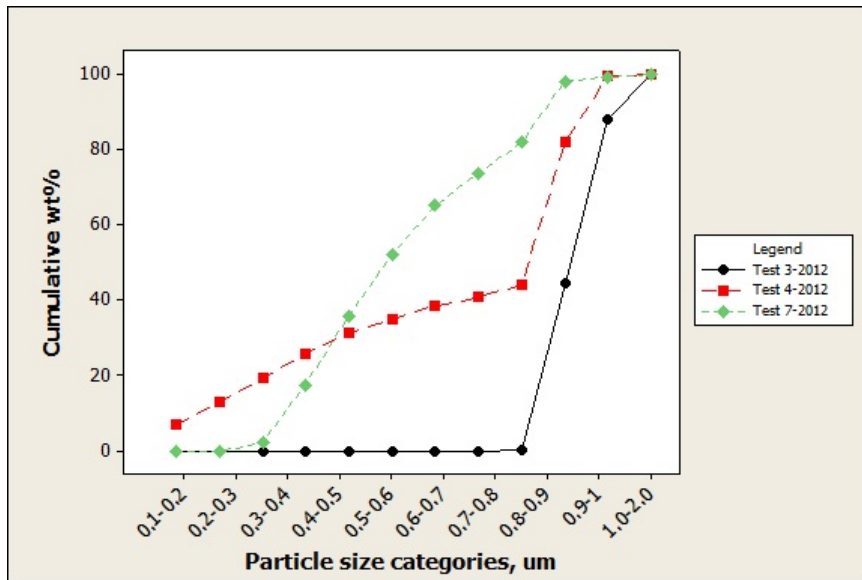
Figure 2.15: Cumulative size distribution of 2012 samples.
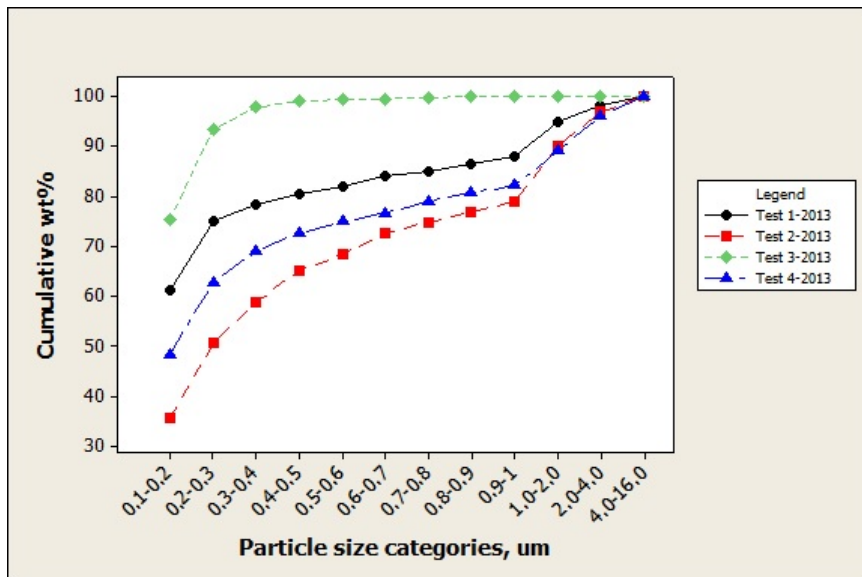
Figure 2.16: Cumulative size distribution of 2013 samples.
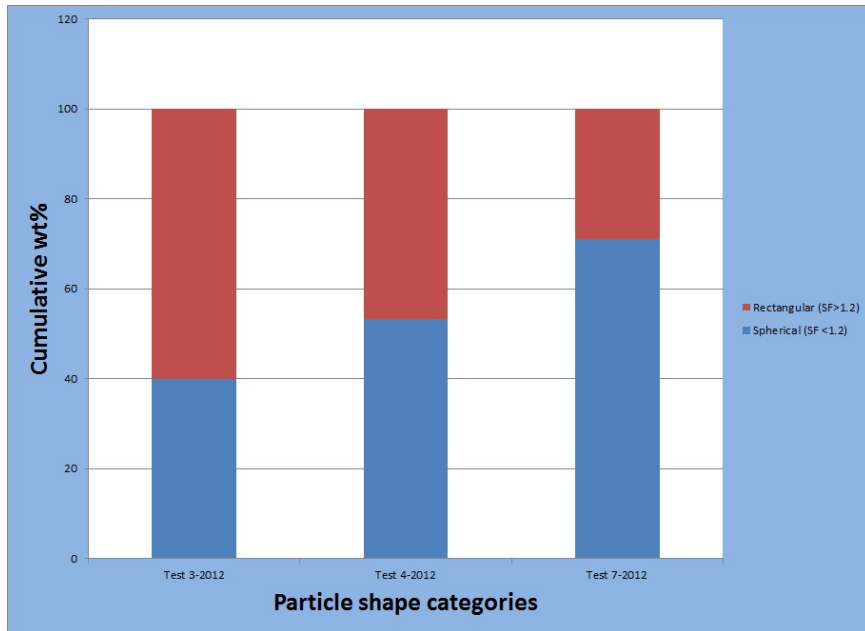
Figure 2.17: Cumulative shape distribution of 2012 particles.
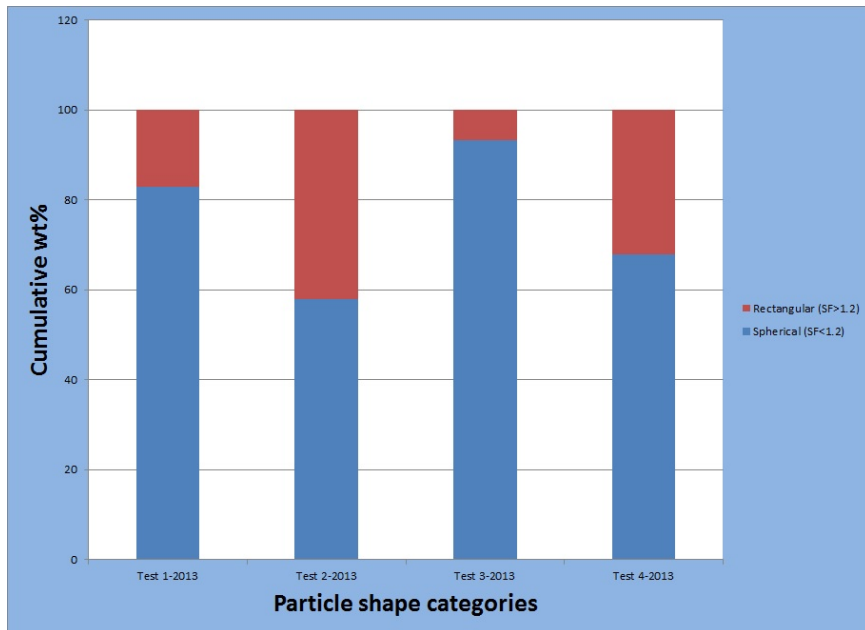
Figure 2.18: Cumulative shape distribution of 2013 particles.

on the inside walls of the TOx. However, after cleaning the TOx it was still high in the combusted syngas mean stream. It was therefore concluded that the Fe present in the syngas came from a reaction of the syngas with the stainless steel pipes used to transport the syngas and the combusted coal itself. Iron initially reacts with carbon to form vapor–phase carbonyls, which, during combustion, react with sulfur to form non–stoichiometric sulfate particles. The excess silicon observed was most likely coming from the coal ash (each coal fired had a high SiO_2 content), possibly through the formation of a silicon monoxide fume. In the TOx, the silicon monoxide may oxidize to form a small particle of silicon dioxide which may then serve as a nucleation site for the iron–rich sulfate. Sulfur content remained an increasing quantity as the sampling progressed (Test 1–2013 to Test 3–2013) and this excess was due to the fact that no sulfur removal was used during those runs.

Most spots present on the filters were composed of very fine particles. The morphology study presented on Figure 2.17 and Figure 2.18 showed that most particles were spherical and few were rectangular. This classification was done based on the shape factor (SF) which is equal or less than 1.2 for spheres and greater than 1.2 for rectangles. The shape factor is used to determine the macroscopic shape of the particle and the shape is a key factor to determining weight percents. SF is equal to 1 for perfect spheres and increases with the angularity of the particle. The shape distribution summary is presented Table 2.14 and Table 2.15. Figure 2.15 and Figure 2.16 show cumulative size distribution of 2012 and 2013 particles. It can be seen that most particles captured at the inlet had diameters typically between 0.2 and 0.5 μm whereas those collected at the outlet were slightly larger and more smoothly spherical (Figure 2.14 (a) and Figure 2.14 (b)). Unfortunately, the particles were so small that good X–ray signals could not be obtained using the EERC SEM. Therefore the exact compositions of the particles could not be determined. An attempt was later made to fix the situation by finding an appropriate and available SEM with greater ability to determine the composition of these small particles. This attempt led us to the use of the OAK RIDGE National Laboratory SEM (JEOL USA) to re–analyze some of the 2012 and 2013 samples. Some pieces of the filter samples were then cut out and sent to OAK RIDGE
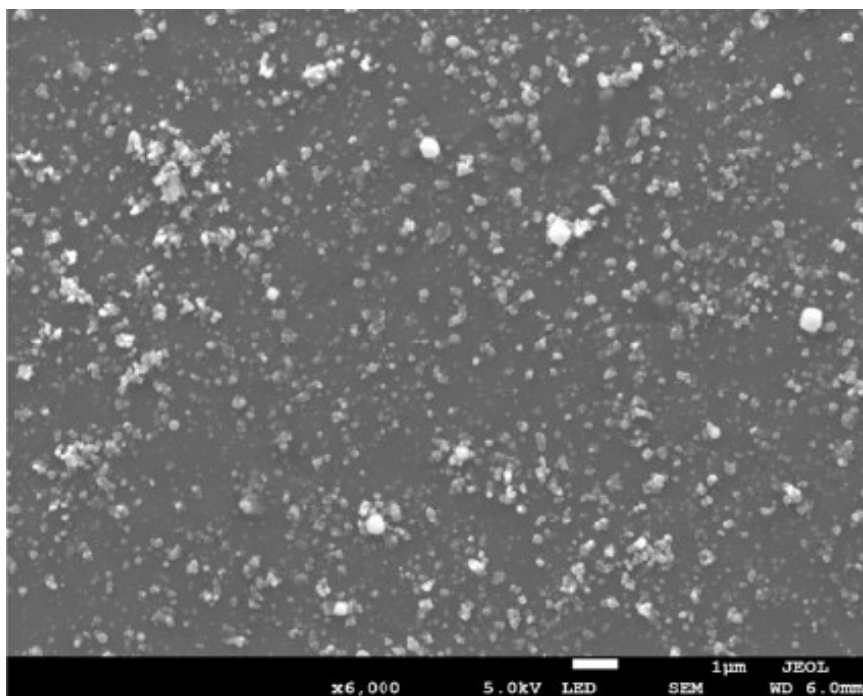
Figure 2.19: SEI image of particles collected on the filter at the TOx inlet.

for analysis using a more powerful field emission–type spectroscope.

Figure 2.19 shows an image of the inlet particles with the OAK RIDGE system. The particles captured at the inlet had diameter typically between 0.2 and 0.5 μm. Figure 2.20 shows two higher–magnification images of the same area. Figure 2.20 (a) was taken using secondary electron imaging (SEI) whereas Figure 2.20 (b) was taken using backscattered electron imaging (BEI). In BEI imaging the contrast is modified by the density of the particles making denser particles to appear brighter than less dense ones. It can be seen that the majority of the particles are darker meaning that the filters analyzed more likely contained higher–atomic–number elements such as sulfur or metals. Those images also reveals that many of the larger particles are composed of conglomerates of 0.1 μm particles. However, OAK RIDGE was also not able to provide sufficient EDS data from the small particles for identification, other than carbon and sulfur, which could have been interference from X–rays emanating from the underlying filter. The small black circles are holes in the filter. Figure 2.21 shows an SEI image taken with the EERC SEM for the particles collected

(a) SEI

(b) BEI
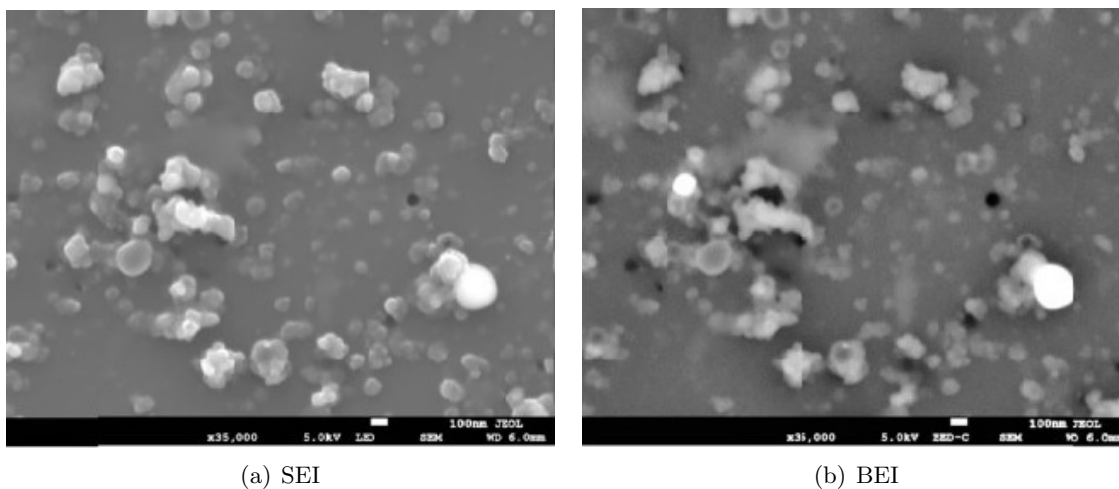
Figure 2.20: Higher–magnification views of the same area showing the difference between SEI and BEI images.

10 μm
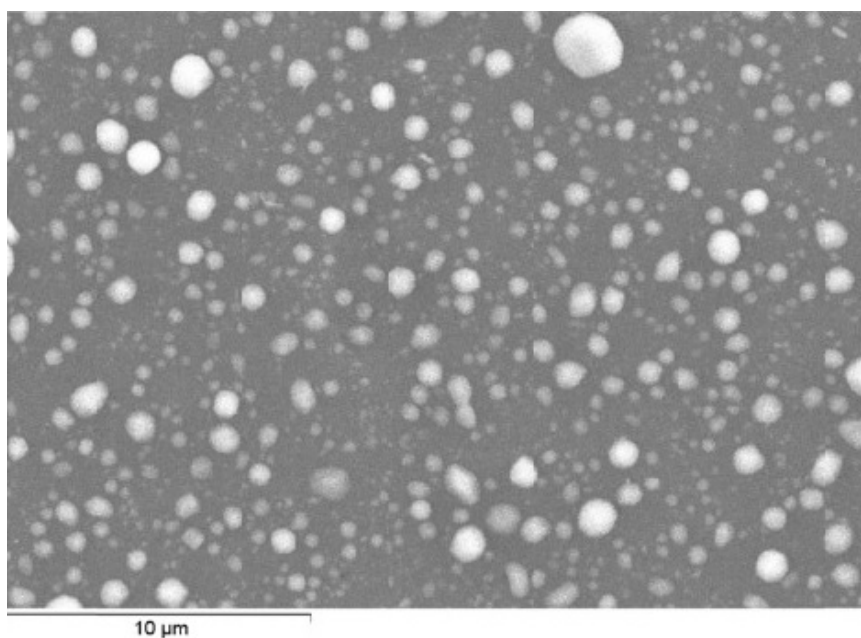
Figure 2.21: SEI image of particles collected on the filter at the TOx outlet.

on the filter at the outlet of the TOx. The image shows that the particles are somewhat larger and more spherical than those collected at the TOx inlet (Figure 2.19). As with the inlet particles, the EDS data were still not conclusive as to the compositions of these particles although more oxygen was detected. Figure 2.22 shows an SEI image taken with the
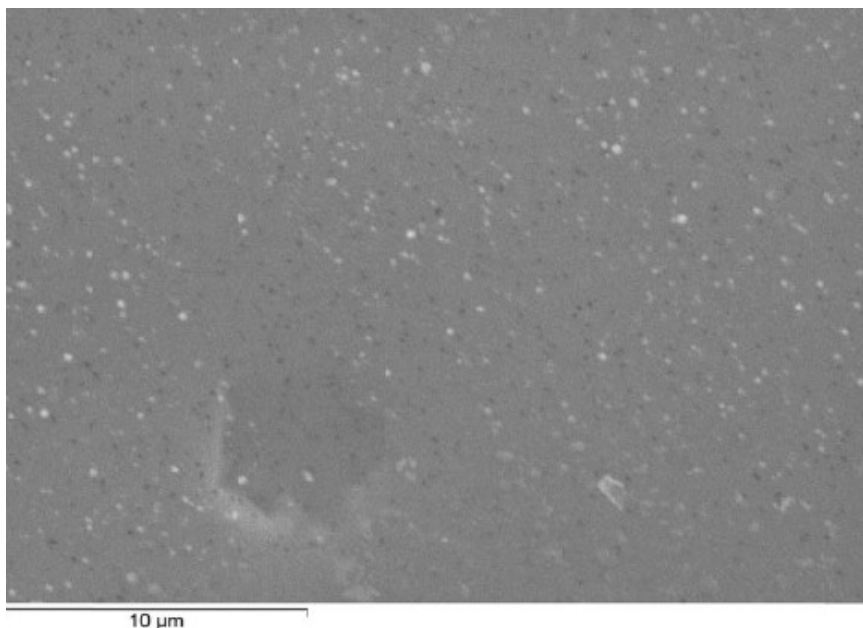
Figure 2.22: SEI image of particles collected on the filter at the TOx inlet when no syngas was being burned.

EERC SEM for particles collected on the filter at the TOx outlet when no syngas was being burned. It shows that the particles collected are much smaller and much less concentrated than those collected from the TOx outlet when syngas was being burned. Because the EDS signals collected both at the EERC and OAK RIDGE were not conclusive as to the exact composition of the particles collected on the filters, a suggestion was made to use the Oak Ridge National Laboratory (ORNL) spectral analysis equipment. The ORNL equipment consists of a X–ray photoelectron and Auger electron spectroscopes. were performed on the samples. In X–ray photoelectron spectroscopy (XPS), surface analyses can be done on electrons emitted from within a few nanometers of the surfaces of the particles and filters while in Auger electron spectroscopy (AES) individual particles can be analyzed. Because AES was hampered by excessive charging of the samples because of their non–conductive nature,

only XPS was performed on the samples. XPS measurements were performed with a K–α XPS instrument (Thermo Fisher Scientific) utilizing a monochromated, micro–focusing, Al K–α X–ray source (h = 1486.6 eV) with a variable spot size (i.e., 30–400 m). The large area samples were all analyzed using the 400 m X–ray spot size for maximum signal. The instrument has a hemispherical electron energy analyzer equipped with a 128 multi–channel detector system and operates at a base pressure of 5 x 10^{-9} mbar or lower. Core level spectra were taken with a pass energy of 50 eV. Samples were mounted to the sample platen with double–sided tape and were therefore electrically isolated from instrument ground. All spectra were acquired using a charge neutralization flood gun to maintain stable analysis conditions (flood gun uses a combination of low energy electrons and argon ions for optimum charge compensation). The typical pressure in the analysis chamber with the flood gun operating is 2 x 10^{-7} mbar. Data were acquired and analyzed using the Thermo Scientifics Avantage software (v4.61). Figure 2.23 shows the XPS spectrum of the TOx inlet
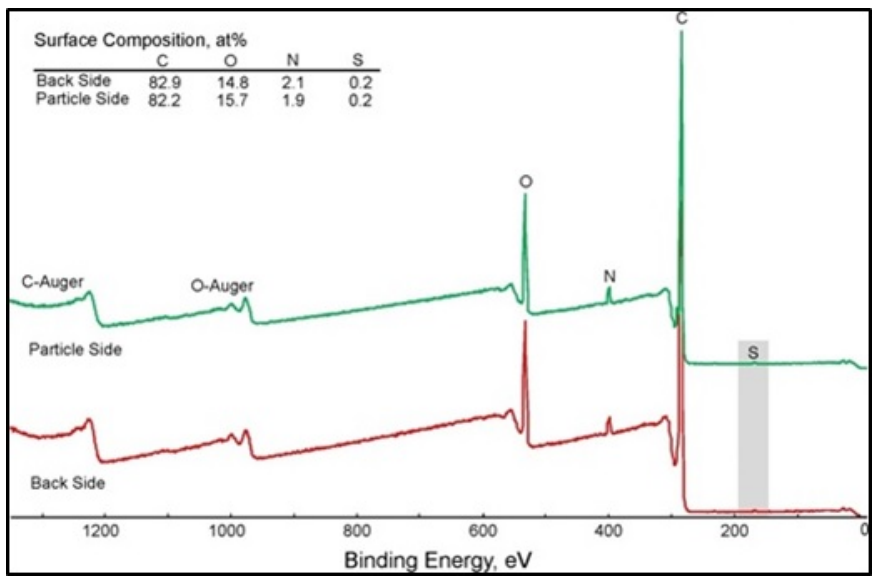
Figure 2.23: XPS spectrum for an area on the front side (filter + particles) of the Test 2–2013 filter sample compared the spectrum collected from an area on the back side (just filter material).

sample containing both particles collected during Test 2–2013. The y–axis represents the count levels in atomic percent (at%) while the x–axis represents their corresponding binding

energies. The spectrum of the particle (particle attached to the filter) was compared to the spectrum of just the filter. The data showed that the particles did not contain any metals. Surprizingly, the atomic composition was almost identical to that of the polycarbonate filter used. It was therefore believed that particles were primarily soot–based and not formed from volatilization of metals in the FBG. Figure 2.24 compares the XPS spectra for parti-
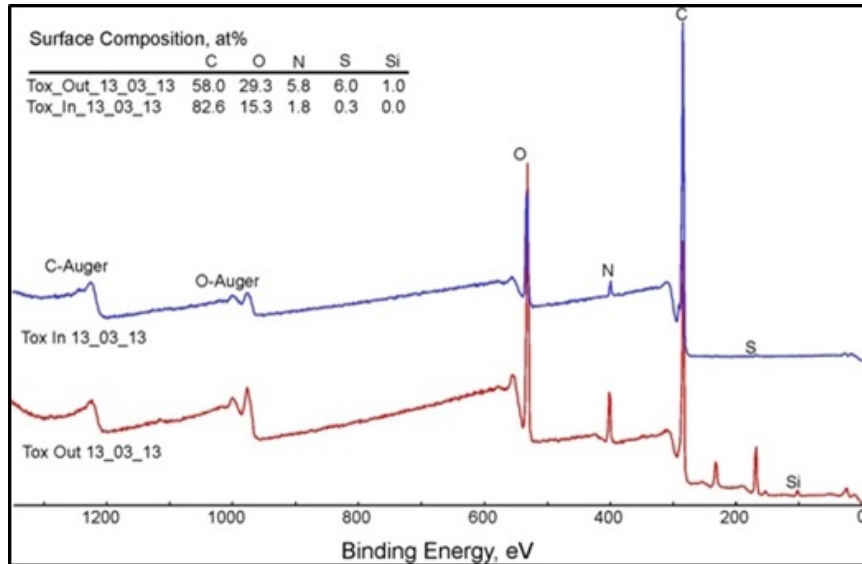
Figure 2.24: XPS spectra for an area of the filter covered with particle collected from the inlet of the TOx (blue) compared to an area of the filter covered with particles collected from the TOx outlet (red).

cles collected from both combusted and non–combusted syngas. Filter area is also included in the analyses. The data indicate that the soot–based particles are not well burned in the TOx, although they are significantly oxidized, nitrided and sulfidized in the combustor. Figure 2.25 shows data for the TOx outlet particles as well as spectra for the same areas after one and two ion etching. The etching remove the outer layers of the particles. The data indicate that the oxidation, nitridation, and sulfidation of the particles are primarily surface phenomena.

At this stage, the results were still inconclusive regarding the exact composition of the small particles and some inconsistencies with previous results were also observed. Therefore, it was decided to run a new set of three M29 tests using two types of grids (holey carbon and
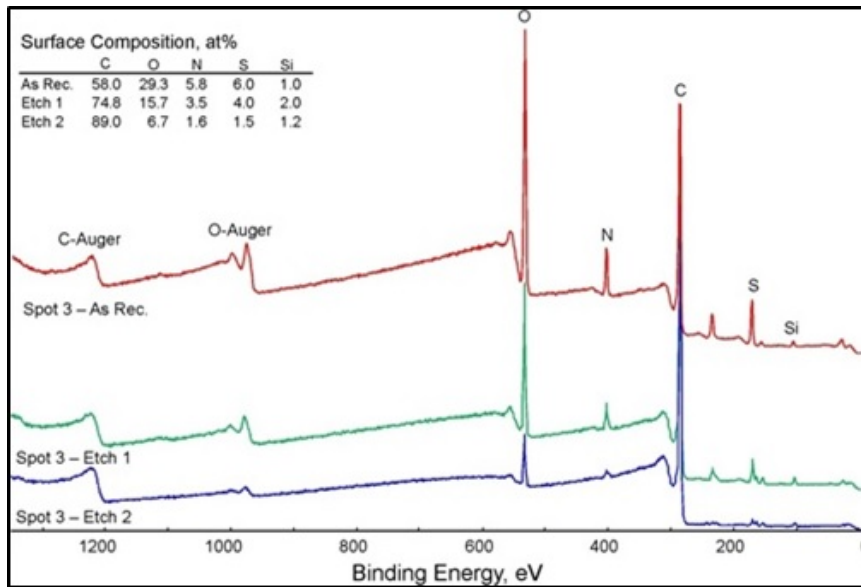
Figure 2.25: XPS spectra for an area of the filter covered with particles collected from the outlet of the TOx before ion etching (red) and after one (green) and two (blue) etching cycles.
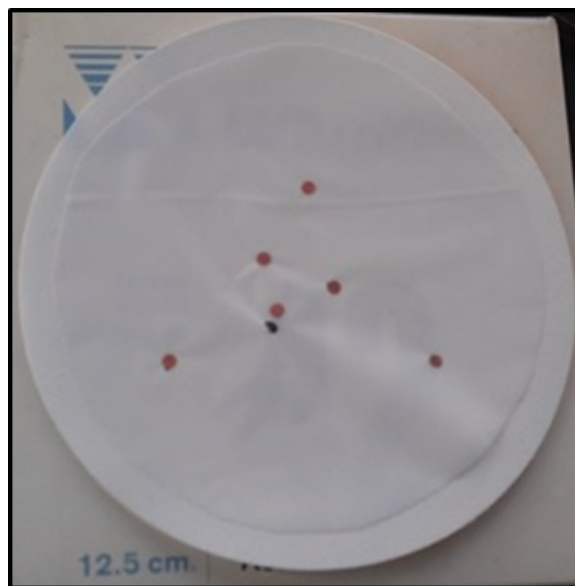
Figure 2.26: Grids used during the third sampling period.

51

copper) attached to three filters. These samples were collected from October to November 2013. The decision to use those grids came from the fact that they are highly conductive as compared to simple carbon–coated filter samples used before. Figure 2.26 shows a picture of the different types of grids used where the inner grids are the holey carbon grids and the outer the simple copper grids. The particulate matter collected on those grids was then sent to the EERC SEM Laboratory for major element detection while the impinger solution samples were sent to the analytical laboratory for minor element (trace metals and ions) detection. The results of these analyses will be part of our future work and hopefully the exact composition of the filter particles will be determined as the subsequent information will be used in the corrosion testing of the Rene 80 – APMT and CM 247 LC – APMT diffusion–bonded plates.

2.4.4 Summary

The long–term durability of GT hot section parts strongly depends on the level of trace metal contaminants in the combusted syngas. These contaminants come from various sources such as compressor inlet air, injected water (and/or steam), fuel gases, improperly handled light fuel oils or evaporative cooler carryover [8, 74, 78–81]. A proper control of these contaminants will help prevent the fouling and corrosion of the hot section components. The syngas analysis performed in this work revealed several elements trapped on the filter surfaces and in the impinger solutions. Five of these elements are of most concern: V, Na, K, Pb, and Ca [79, 80]. This is because their presence in significant amount usually leads to blades fouling and severe corrosion of the GT materials, resulting in the reduction of the overall efficiency of the GT. The significance level is expressed in terms of parts per million (ppm) of fuel equivalent content. In other terms, 1 ppm of fuel contaminant is equivalent to 1 pound of contaminant entering the turbine section about every 50 hours [79]. Owners of commercial GT are being required to limit the trace metal emissions in the syngas to a maximum of 2 ppm or less [78–80]. Typical values recommended by GT manufacturers are shown in Table 2.16 where all values are given in fuel equivalent parts per million by weight (ppmw).

The total ppmw values measured in this work are shown in Table 2.17 for the first

Table 2.16: Maximum contamination values in ppmw for the hot gas path in GT as specified by turbine manufacturers [80].

Element	Maximum contamination (ppmw)
Na + K	1.00000
Pb	1.00000
Ca	2.00000
V	0.50000

set of samplings. These values were calculated using Equation 2.4.1 along with the Excel spreadsheet of Reference [82].

$$X_T = \frac{A}{F}.X_A + \frac{S}{F}.X_S + X_F \qquad (2.4.1)$$

Where:

X_T = total contamination in fuel equivalent ppmw

$\frac{A}{F}$ = air to fuel mass flow ratio

$\frac{S}{F}$ = steam (water) to fuel mass flow ratio

X_A = contaminant concentration in inlet air ppmw

X_S = contaminant concentration in injected steam or water ppmw

X_F = contaminant concentration in fuel ppmw

The second set was not analyzed for its ppmw because it contained non–combusted syngas samples collected from the inlet of the TOx. It was of no interest because the limitation on the trace metal emission in GT only applies to the combusted syngas exhiting the combustion chamber as the resulting combustion byproducts are the agents responsible of corrosion observed on the GT blades. From Table 2.17 it can be seen that many of the trace metals detected fall in the range of 0–1 ppmw except silicon and sulfur which had respective ppmw values of 3.69 and 4.6 for Test 4–2012. The high sulfur–content was most probably due to the fact that no sulfur removal was used on that day. The high silicon–content was probably due to the rust present at the bottom of the TOx and some of that silicon might have come from the inner walls of the stainless steel pipes used to transport the

Table 2.17: Maximum contamination values in ppmw for the hot gas path in GT as measured in this work.

Element	Maximum contamination (ppmw)		
	Test 3–2012	Test 4–2012	Test 7–2012
Al	0.25000	0.26000	0.39000
Ba	0.00200	0.00170	0.00260
Ca	0.03400	0.03600	0.05200
Fe	0.02900	0.05000	0.01900
Mg	0.01700	0.01800	0.02600
P	0.13000	0.14000	0.20000
K	0.35000	0.37000	0.54000
Si	1.99000	3.69000	0.45000
Na	0.59000	0.62000	0.00090
S	0.28000	4.60800	1.67000
Ti	0.00130	0.00260	0.00044
V	0.00002	0.00026	0.00039

syngas. This can be justified by comparing the data of the first sets of sampling to the data of the second sets which happened after the TOx was thouroughfully cleaned. The second sets had much smaller sulfur and silicon contents as compared to the first sets. Therefore, it is highly recommended to produce syngas in a rust–free environment and make sure that each contaminant removal equipment is connected and fully functional. If effective, this will result in a very clean syngas production and small risk of corrosion of the hot section parts. The effect of trace metals contaminants should be of interest and concern to all gas turbine users, irrespective of the type of fuel used. The low ppmw values of Table 2.17 show that the syngas produced at the UND–EERC is of good quality and can be tolerated by almost or any industrial GT without posing any safety risks. Nevertheless, these low ppmw values are still likely to corrode the GT inner parts if exposed to these impurities usually at high rates for a period ranging from few hours to a couple of days. For instance, Gurrappa [83] observed that a CM 247 LC cylindrical specimen (10 mm in diameter and 20 mm in height) was severely corroded in just 4 hours and was completely consumed in 70 hours after being exposed to a mixture of sodium sulfate and sodium chloride (90 % Na_2SO_4 + 10 % NaCl) at 900^oC. Khorrami et $al.$ [84] observed that a 10x12x4 mm Rene 80 specimen when exposed

to sodium sulfate at 850°C oxidized at a rate of 4.71x10^{-8}g^{2}cm^{-4}s^{-1} and was completely consumed at 900°C after 4 cycles. Eliaz *et al.* [34] reported that in order to attain good resistance to high temperature hot corrosion a nickel–based alloy must have a minimum of 15 wt% of chromium. Because CM 247 LC and Rene 80 do not satisfy this criterion, they are very susceptible to high temperature hot corrosion. Therefore, the bilayered structures of Rene 80 – APMT and CM 247 LC diffusion–bonded using the EMB process will be subjected to corrosion testing in order to understand their behavior in the type of syngas such as the one produced at the UND–EERC.

CHAPTER III

MODELING OF BONDING PRESSURES

The objective of this part of the work was to design a high–temperature clamping system to hold the APMT plate to the superalloy turbine structure with an evenly distributed pressure. This was done by simulating the bonding pressures during the heating of a bonding assembly (clamping system + bonding specimens) used to bond two superalloy plates. One of the plates was APMT and the other plate was either Rene 80 or CM 247 LC. The clamping system provided the force necessary to hold together the two plates which were bonded using a new bonding technique called evaporative metal bonding (EMB). A full understanding of bonding pressures especially at the interface of the bonding plates, was crucial mostly because joints created using the EMB process are good only if an adequate force is applied to the joint surface [2] and also because varying the level of compressive stress in a diffusion couple could affect the rate of growth of second phases [85]. The change in bonding pressure, as a result of increasing temperature in the system, depends on several factors such as the coefficient of linear thermal expansion (CTE), the compressive modulus of elasticity (CME), the applied temperature difference (bonding temperature), and the force distribution applied by the clamping system (bonding load). The next two sections focus on describing the bonding assembly as well as the bonding method (EMB). Then follow the results of CTE measurements for the three superalloys. The last section presents the finite element simulation results obtained from ANSYS with the input from the previous sections.

3.1   Description

3.1.1   Bonding Assembly

The initial bonding assembly was composed of a TZM molybdenum (0.50 % Titanium + 0.08 % Zirconium + 0.04 % Carbon + 99.38 % Molybdenum) clamping system (jig +

threaded bolt), two 1–inch diameter cylindrical rods (Rene 80, CM 247 LC and APMT), a 25–μm–thick zinc foil and two E52100 alloy steel hemispheres. The assembled view is shown on Figure 3.1 (a) while the exploded view is shown on Figure 3.1 (b).
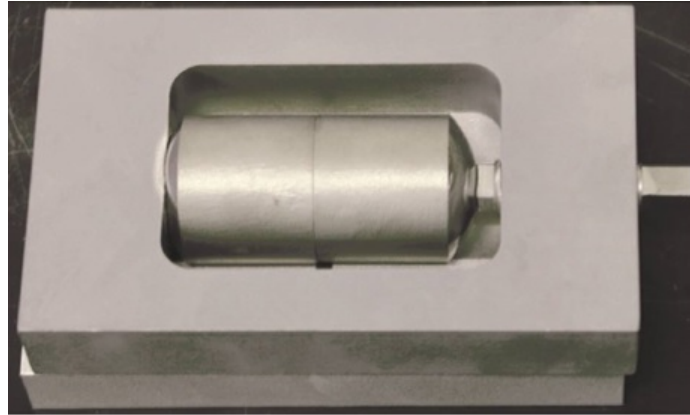
(a) Assembled view
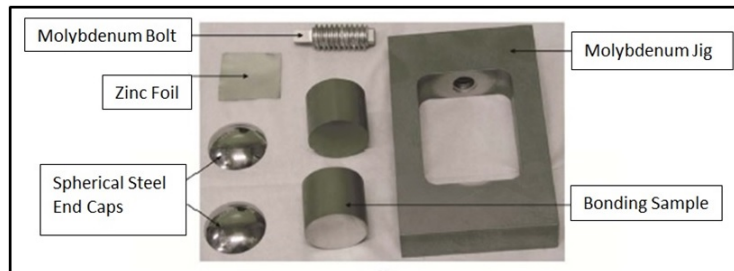
(b) Exploded view

Figure 3.1: Assembled and exploded views of the clamping system .

The advantage of using TZM molybdenum was that it had a CTE value much lower as compared to other two superalloys being joined. As consequence, it expanded less during heating and more pressure was applied to the rods. The bonding assembly was prepared by aligning the surfaces to be bonded and clamping them together with a thin foil of zinc between them. TZM molybdenum bolts were used to hold the rods in place, and pressure was applied to the rods by tightening the bolts to a fixed torque of 25 lb.in. The direction of the applied force is shown in Figure 3.2. The buffer plates served to distribute the force evenly across alloy plates which were being joined. To assure that the surfaces being joined were in perfect alignment, E52100 alloy steel hemispheres were placed on each end of the rods to allow them to fully articulate during the bonding process. The ends of the clamping
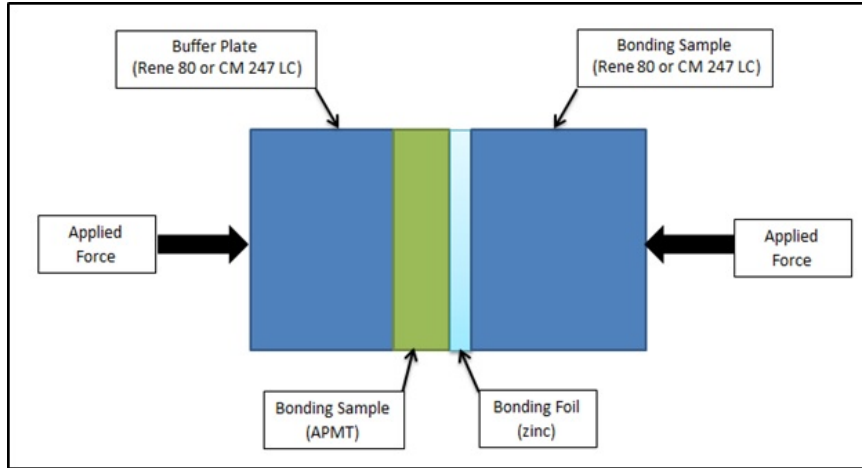
Figure 3.2: Schematic image of the modeled geometry.

bolts and the surface of the body where the E52100 alloy steel hemispheres contact the fixture were machined to match the curvature of the hemispheres in order to distribute the force evenly across the bonding surfaces.

3.1.2 Bonding Method

The EMB process is a new diffusion bonding technique developed at the EERC by Hurley *et al.* [2]. EMB is a solid–state joining process in which the surfaces of the specimens to be joined are held together and heated under a compressive load in a vaccuum environment. It is a variant of the traditional bonding method called transient liquid phase (TLP) but with the particularity that a zinc foil is used as bonding interlayer between the two metals to be bonded. As the whole system is being heated, the oxide scales and a portion of the metals to be joined dissolve allowing the melted zinc to diffuse through the joint and migrate towards the surface where it vaporizes completely. The joint formed with EMB is a much stronger bond as compared to other types of TLP bonds in which the bonding metal usually remains in the structure and can weaken the bondline by forming some secondary phases. The advantage of using zinc over other metals is that it melts and vaporizes at relatively low temperatures. Three primary parameters affect the EMB process: the bonding temperature, the bonding pressure, and the holding time [86, 87]. But the process can also be affected by some secondary parameters such as the bonding environment, the material

properties, and the surface finish of the bonding faces.

The bonding temperature is about 60% of the absolute melting point of the most fusible material in the bonded composition [86]. A bonding temperature of $1214^{o}C$ was chosen for the current EMB process as it was experimentally determined that effective bonding only occurs at or above that value [88]. Elevated temperature aids the plastic deformation of the bonding faces asperities and accelerates the zinc diffusion throughout the whole system. A study performed by Mahendran *et al.* [89] showed that the bonding temperature has predominant effect on the bonding surface characteristics as shown in Figure 3.3. The joint shear and bonding strengths increase with increasing bonding temperature [89].

The bonding pressure initially applied via the clamping forces was small (about 2.4 MPa) but sufficient to fabricate good joints [88]. The pressure applied throught a compressive load helps to initiate the contact between the mating faces to be bonded and also to ensure that all gaps and voids were filled during the bonding process without creating any macroscopic deformation. It has been demonstrated that the joint strength increases with the bonding pressure up to a certain threshold (about 10 MPa) then decreases if the bonding pressure continues to rise [89–92]. Figure 3.4 shows an illustration of the bonding pressure effect [90].

Holding time affects the bonding process in the sense that it has to be enough for the diffusion to take place but not too long as it might create some voids leading to a bad
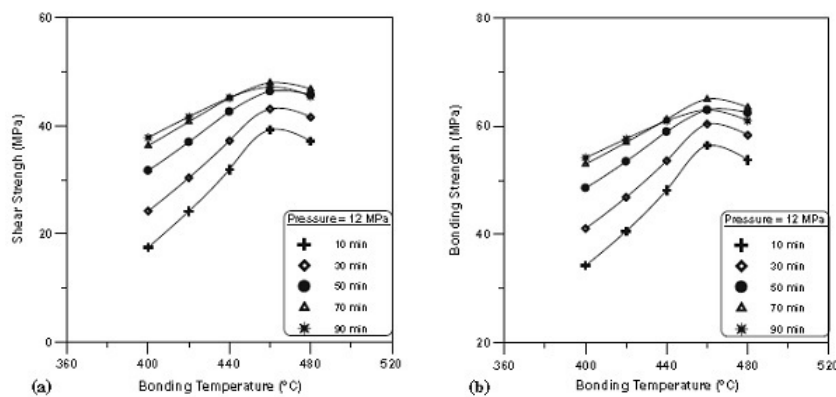
Figure 3.3: Effect of bonding temperature on bond characteristics [89].
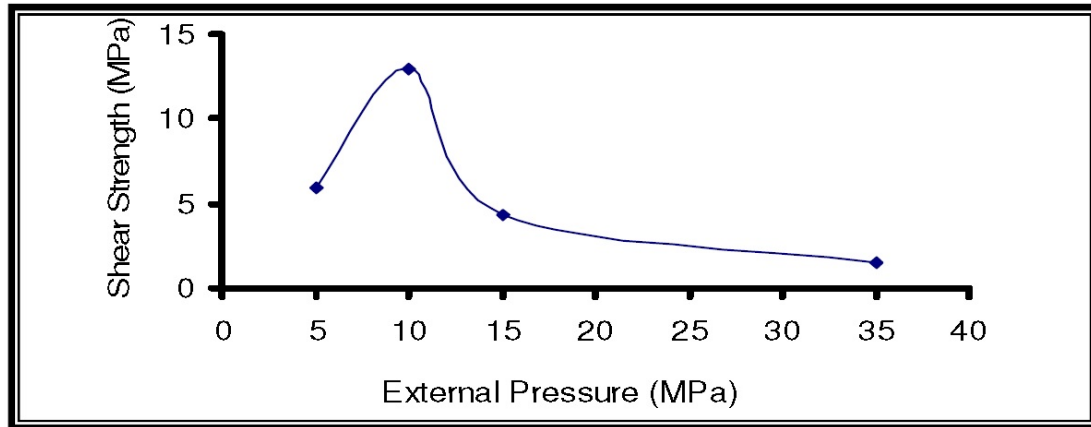
Figure 3.4: Effect of bonding pressure on bond characteristics [90].

joint. The higher the holding time, the higher the shear strength as an adequate holding time allows complete diffusion and better void closure [93]. A holding time of 12 hours was shown by Braband [88] to be sufficient to allow complete diffusion and vaporization of zinc through the bonding plates.

The heating cycle used in the EMB process includes five different phases as shown in Figure 3.5. Initially the clamping assembly was heated up to 700^oC at a rate of 450^oC/hour (phase 1). After reaching 700^oC, the temperature was held constant for about 1.5 hours (phase 2). Then the clamping system was heated again up to 1214^oC at a rate of 250^oC/hour (phase 3). At this point the temperature was held constant again but this time for a duration 12 hours (phase 4). After the 12 hours period the system automatically begins to cool down to room temperature at a rate of 800 ^oC/hour so as to minimize the residual stresses at the bonding surface. In phase 1, a high vacuum up to $6*10^{-4}$ mbar was created in the furnace tube (shown in Figure 3.6) and filled with argon at a partial pressure of 50 psi to remove any unwanted contaminant. The presence of argon gas enhances the cleanliness of the bonding surfaces and the sublimation of the oxide scales [86]. Argon was removed at the end of phase 1 to prevent any void or porosity formation in the bonded region due to argon impurities [94]. The holding time of phase 2 was to give the melted zinc enough time to diffuse through the entire structure. The heating process of phase 3 allows the diffused zinc to vaporize, leaving place to the bonding process to take place. The EMB process was used
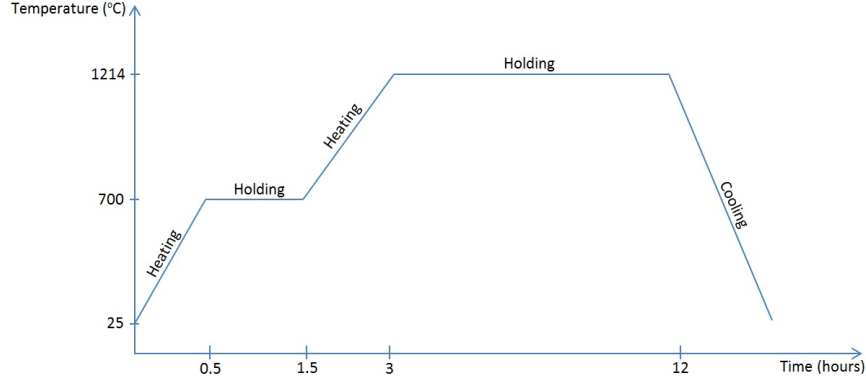
Figure 3.5: Heating curve used in samples preparation.

to successfully bond APMT small cylindrical samples to Rene 80 and CM 247 LC samples of the same shape as shown on Figure 3.7 (b). The diffusion–bonded specimens all had a 1.1 inch diameter and the following thicknesses: zinc foil 0.25 μm, APMT 0.1 inch, Rene 80 and CM 247 LC 1 inch. The bonding face of each specimen was sandblasted and polished using a 1200 grade diamond–coated grinding paper. All specimens were ultrasonically cleaned for 55 minutes and stored in isopropanol until they were ready for bonding. The inner plates not labeled on Figure 3.7 (a) are the APMT plates.

3.2   Thermal Expansion Measurements

3.2.1   Background

The thermal expansion is the decrease or increase in dimensions which occurs as a material is being heated. Cverna [95] defines the CTE as a material property that is indicative of the extent to which a material expands upon heating. For a solid at a given temperature, the mean CTE is calculated using Equation 3.2.1 [96]:

$$\alpha_m = \frac{\Delta L_{sp} * k}{L * \Delta T} \tag{3.2.1}$$

Where ΔL_{sp} is the change of specimen length in μm, L the specimen length at room temperature, ΔT the temperature difference over which the change in specimen length is
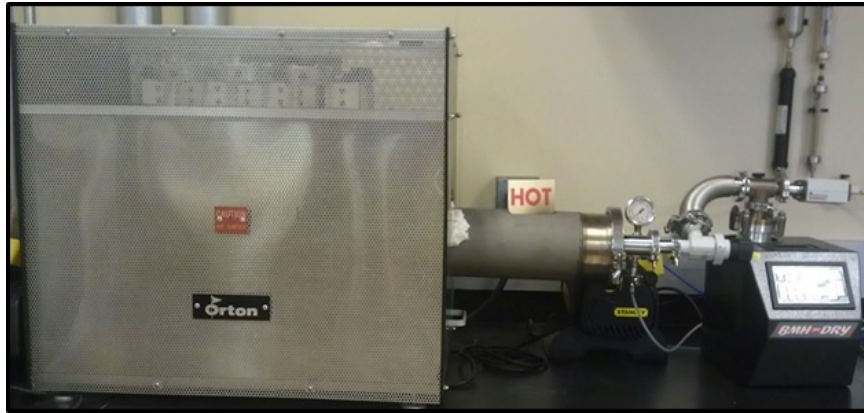
Figure 3.6: Tube Furnace used to prepare samples.

(a) Before bonding

(b) After bonding

Figure 3.7: Rene 80 – APMT and CM 247 LC – APMT specimens bonded using the EMB process .

measured in ^oC and k the calibration coefficient defined by Equation 3.2.2 [96]:

$$k = \frac{\alpha_{ref} * L_{ref} * \Delta T_{ref}}{\Delta L_{ref}} \qquad (3.2.2)$$

in which α_{ref} is the mean CTE for alumina in $\mu\epsilon/^oC$, L_{ref} the alumina reference length at room temperature, ΔT_{ref} the temperature difference over which the change in alumina reference length is measured in ^oC and ΔL_{ref} the change of alumina reference length due to heating. But in this work, the k value was calculated using an empirical formula given by Equation 3.2.3.

$$F(T) = [1.8948 + 1.6631 * 10^{-2}T - 1.3496 * 10^{-5}T^2 + 4.1192 * 10^{-9}T^3] * 10^{-6}K \quad (3.2.3)$$

Where the function F(T) was automatically generated by the thermomechanical analyzer. This function represents the differential correction to make on the thermal expansion measurement when alumina is used as reference material. The validity of Equation 3.2.3 holds for temperatures between 0 and 1600K. The CTE variations were measured from room temperature to 1200^oC in order to accurately model the high–temperature behavior of the APMT – Rene 80 and APMT – CM 247 LC clamping assemblies.

3.2.2 Experimental Procedure

A computer–operated thermomechanical analyzer was used to measure the CTE of E52100 alloy steel, TZM molybdenum, Rene 80, CM 247 LC and APMT, all heated and loaded at constant rates. A brief description of the sample preparation, the equipment used, the procedure and CTE determination method follows.

3.2.2.1 Apparatus. Thermal expansion measurements were made using a SHI-MADZU TMA–60H (Figure 3.8) thermomechanical analyzer. Instructions were followed as described in the ASTM Standard Tests Method E831 relative to the linear thermal expansion of metallic materials at elevated temperatures measurements by thermomechanical analysis [96]. The thermomechanical analyzer used mainly consists of a rigid sample holder used to center the specimen in the furnace and fix it to mechanical ground, a rigid expansion
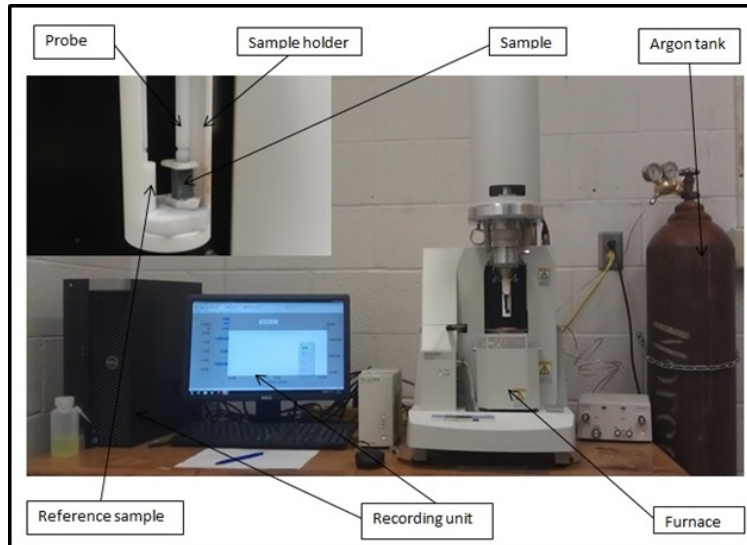
Figure 3.8: Thermomechanical Analyzer used.

probe used to contact the specimen with an applied compressive force, a furnace used to heat or cool the specimen at a constant rate, an argon tank used to sustain an inert environment around the specimen being heated, and a recording unit used to display the loaded specimen displacement as a function of temperature. Internal components and components not labeled on Figure 3.8 are:

- A temperature–sensing element linear over a minimum range of 2 mm and used to measure the displacement of the rigid expansion probe to within $\pm$ 50 nm resulting from changes in length of the specimen.

- Alumina buffer plates used to prevent any direct contact between the specimen, the sample holder (lower position) and the probe (upper position).

- A transducer used to generate a constant force of 1 to 100 mA (0.1 to 10 g) that is applied through the rigid expansion probe to the specimen.

- A thermocouple acting as temperature sensor and placed in close proximity to the specimen.

- A temperature controller used to execute the temperature program described in the previous section and to operate the furnace at rate of $20^oC/min$ between 25^oC and 1200^oC.

3.2.2.2   Sample preparation. APMT plates were provided by Sandvik Kanthal, Rene 80 and CM 247 LC plates by Siemens Power Generation, TZM molybdenum plates by Eagle Alloys and E52100 alloy steel plates by McMaster Carr. Each material was cut in three samples of about 2x2x12 mm in dimension. Samples were sandblasted and washed with propanol to prevent any contamination and kept in plastic boxes.

3.2.2.3   Procedure. The initial length of each specimen was measured and the sample placed in a vertical position in the specimen holder under the probe and between the buffer plates and next to an alumina reference sample. Once the sample was in position, a compressive load of 0.01 N was applied to the sensing probe as to hold the specimen in place and the furnace was turned on. All samples were heated by an increment of 100^oC at a rate of $20^oC/minute$ and held there for 15 minutes and then heated for another 100^oC. This process was repeated from room temperature to 1200^oC. The heating curve is shown on Figure 3.9.
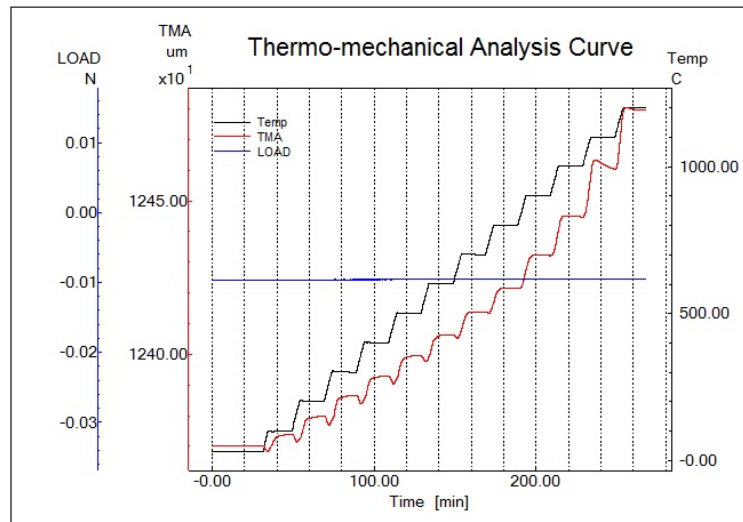
Figure 3.9: Thermal Expansion Curve.

Upon heating, the specimen expands, pushing up the probe which then transmits the changes in length of the specimen to a transducer which translates the movements of the probe into electrical signals which were then recorded in a computer in the form of an Excel spreadsheet. The precision of our measurements was determined to be better than $\pm$ 2 % over the range of 25 to 1200°C by means of verification tests using TZM molybdenum and E52100 alloy steel rods as reference materials. The system was purged with argon at a flow rate of 500 mL/min and a constant pressure of 15 psi to minimize the oxidation of the samples during the runs. The data set (temperature + expansion length) were stored at 1 s interval for each specimen. The temperature calibration was done according to the Test Method E831 [96] and a differential correction was applied to all measured expansions.

3.2.2.4 CTE Determination. From the Excel spreadsheet, CTE values were calculated using Equation 3.2.1 by averaging the 900 data points generated during the 15 minutes when the temperature was held constant. The final CTE values were calculated as an average of three different CTE corresponding to three specimens of the same superalloy. The final CTE values are shown in Table 3.1 for a temperature range of 100 to 1200°C. The CTE values are expressed in m/m.^{o}C and the temperature in ^{o}C. To make sure that our data were of good quality, measurements were performed on known metals such as E52100 alloy steel and TZM molybdenum and results were compared with those of Reference [97] and Reference [98] for the temperature range of 0 to 100°C. For E52100 alloy steel the value measured in this work was 1.14E-05 m/m.^{o}C while the value found in Reference [98] was 1.19E-05 m/m.^{o}C. For TZM molybdenum the value found in Reference [97] was 0.52E-05 m/m.^{o}C while the value measured in this work was 0.75E-05 m/m.^{o}C. The remaining CTE values are shown in Table 3.2 for further comparison.

3.2.2.5 Discussion. This discussion carries on the effect of the thermal mismatch of the APMT – Rene 80 and APMT – CM 247 LC evaporatively–bonded samples. Rene 80, CM 247 LC and APMT CTE values measured in this work were compared with those of Reference [99], Reference [100] and Reference [101] as shown in Table 3.3. The comparative trends are shown on Figure 3.10.

Table 3.1: Mean CTE as a function of temperature for each bonding superalloy used.

T	Rene 80		CM 247 LC		APMT	
	CTE	**Stdev**	**CTE**	**Stdev**	**CTE**	**Stdev**
100	1.30E-05	8.85E-08	1.23E-05	3.38E-08	1.42E-05	6.02E-08
200	1.42E-05	6.58E-08	1.36E-05	6.53E-08	1.46E-05	1.10E-07
300	1.52E-05	4.09E-08	1.48E-05	3.75E-08	1.58E-05	5.89E-08
400	1.59E-05	2.31E-08	1.56E-05	2.23E-08	1.66E-05	2.80E-08
500	1.64E-05	1.75E-08	1.62E-05	1.40E-08	1.69E-05	2.24E-08
600	1.68E-05	1.21E-08	1.67E-05	1.01E-08	1.70E-05	1.15E-08
700	1.72E-05	7.77E-09	1.71E-05	6.99E-09	1.71E-05	4.84E-09
800	1.75E-05	4.41E-09	1.74E-05	5.57E-09	1.73E-05	5.02E-09
900	1.80E-05	3.72E-09	1.77E-05	3.66E-09	1.76E-05	3.13E-09
1000	1.86E-05	2.98E-09	1.79E-05	1.32E-08	1.78E-05	8.13E-09
1100	1.96E-05	2.25E-08	1.75E-05	1.95E-08	1.78E-05	1.06E-08
1200	2.06E-05	4.69E-10	1.74E-05	1.28E-09	1.80E-05	8.47E-09

Table 3.2: Comparison between the TZM Molybdenum and E52100 alloy steel CTE values measured in this work with those found in the literature

T	E52100 Alloy steel		TZM Molybdenum	
	This work	**Ref. [98]**	**This work**	**Ref. [97]**
100	1.140E-05	1.119E-05	0.750E-05	–
200	1.511E-05	–	0.857E-05	–
300	1.752E-05	1.125E-05	1.019E-05	0.508E-05
400	1.842E-05	–	1.108E-05	0.512E-05
500	1.873E-05	–	1.159E-05	–
600	1.872E-05	–	1.183E-05	0.523E-05
700	1.851E-05	–	1.187E-05	0.529E-05
800	1.694E-05	–	1.199E-05	0.537E-05
900	1.880E-05	–	1.201E-05	0.545E-05
1000	1.941E-05	–	1.332E-05	0.553E-05
1100	1.862E-05	–	1.479E-05	–
1200	1.722E-05	–	1.528E-05	0.5730E-05

Table 3.3: Comparison between the Rene 80, CM 247 LC and APMT CTE values measured in this work with those found in the literature

T	Rene 80		CM 247 LC		APMT	
	This work	Ref. [101]	This work	Ref. [100]	This work	Ref. [99]
100	1.30E-05	–	1.23E-05	–	1.42E-05	–
200	1.42E-05	–	1.36E-05	1.27E-05	1.46E-05	1.24E-05
300	1.52E-05	–	1.48E-05	1.30E-05	1.58E-05	1.24E-05
400	1.59E-05	–	1.56E-05	1.32E-05	1.66E-05	–
500	1.64E-05	1.6E-05	1.62E-05	1.34E-05	1.69E-05	1.31E-05
600	1.68E-05	–	1.67E-05	1.36E-05	1.70E-05	–
700	1.72E-05	1.7E-05	1.71E-05	1.39E-05	1.71E-05	1.36E-05
800	1.75E-05	–	1.74E-05	1.43E-05	1.73E-05	1.36E-05
900	1.80E-05	–	1.77E-05	1.48E-05	1.76E-05	–
1000	1.86E-05	–	1.79E-05	1.56E-05	1.78E-05	1.47E-05
1100	1.96E-05	–	1.75E-05	1.67E-05	1.78E-05	–
1200	2.06E-05	–	1.74E-05	1.82E-05	1.80E-05	1.54E-05
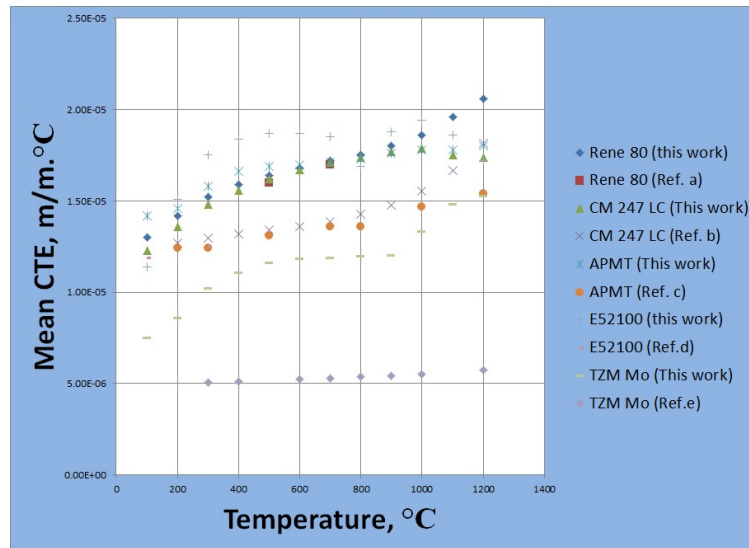
Figure 3.10: Comparative trends between the CTE values measured in this work and those found in the literature (Ref. a = Reference [101], Ref. b = Reference [100], Ref. c = Reference [99], Ref. d = Reference [98]), Ref. e = Reference [97]).

From Table 3.1 it can be observed that APMT has the highest expansion coefficient at all temperatures as compared to Rene 80 and CM 247 LC. The high expansion of APMT is due to its high iron content which is about 69 % of the total chemical composition. The low values of the thermal expansion of each superalloy demonstrated its stability at high temperature. The measurements showed small differences in the thermal expansion behavior of these three superalloys over the temperature range of 100 to 1200°C. Rene 80 had the lowest CTE values from 25 to 900°C followed by CM 247 LC. But after that range, Rene 80 appeared to have experienced a high–temperature phase transformation as about 35% increase in mean CTE was observed from 900 to 1200°C, while CM 247 LC and APMT increased with the same initial trend. A slight decrease starting from 1100°C, was also observed in the CM 247 LC CTE values as the temperature increased. It is also observed from Figure 3.10 that the CTE values measured in this work were relatively closed (about 4 % difference) to those found in the literature for all the superalloys used except for TZM molybdenum whose CTE values were twiced those found in Reference [97].

3.3   Numerical Analysis

An initial simulation was run by Braband [88] where the focus was on diffusion bonding of similar alloys. He investigated three bonding cases: Rene 80 – Rene 80, APMT – APMT and CM 247 LC – CM 247 LC. He found that for Rene 80 – Rene 80 (Figure 3.11 (a)) and CM 247 LC – CM 247 LC (Figure 3.11 (b)) joints stresses were the greatest at the center of the bonding area decreasing out to the edge of the bond. Stress decreased sharply at first and became more gradual and almost leveled towards the edge of the bond.

For the APMT – APMT (Figure 3.12 (a)) joint the stress distribution across the middle of the bond region was relatively constant then increased to a maximum then decreased again before the edge of the bond where it was at a minimum. He also observed that the maximum stress at the bonding surface exceeded the yield stress of APMT and it was assumed that the APMT yielded during the bonding process. He also discovered that the contact between the jig and the hemispheres should be circular for an even stress distribution and that a bonding time of 12 hours was sufficient to make good bonds. This bonding time was shown to be enough to avoid Kirkendall voids formation which is a major problem in
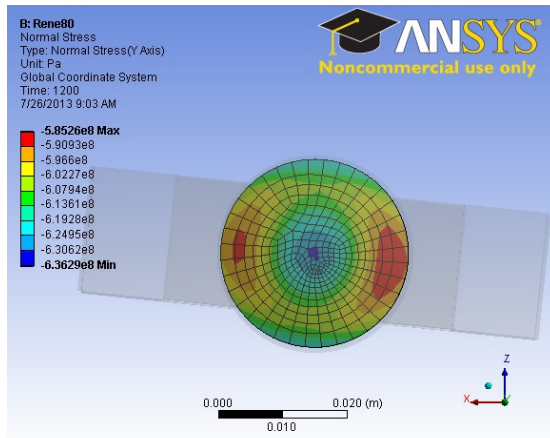
(a) Rene 80 – Rene 80
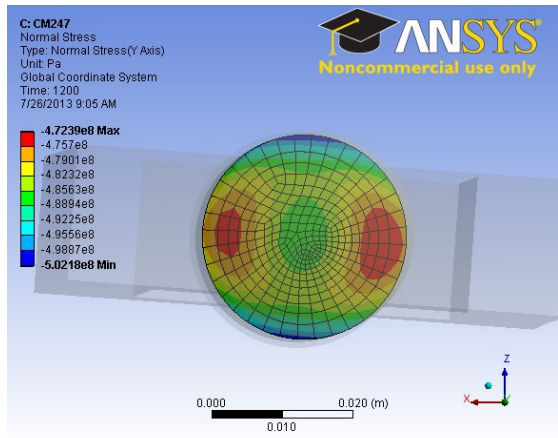
(b) CM 247 LC – CM 247 LC

Figure 3.11: Normal stress distribution at the bonding surface at 1200°C for Rene 80 and CM 247 LC [88].

various diffusion bonding processes.
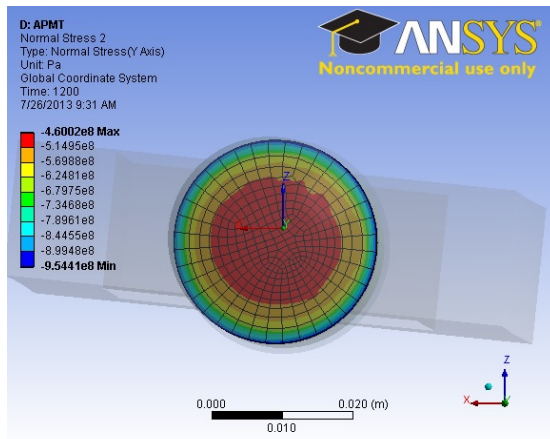
(a) APMT – APMT
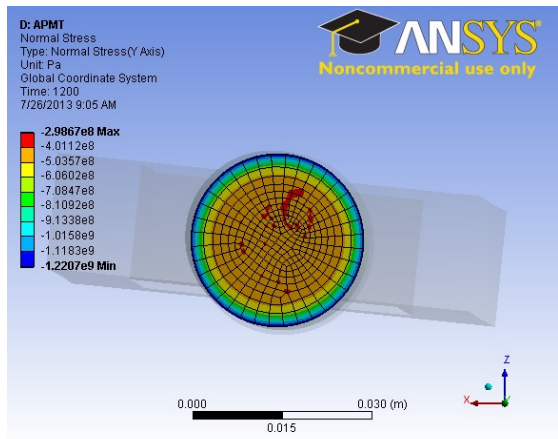
(b) APMT with Rene 80 used as buffer plate

Figure 3.12: Normal stress distribution at the bonding surface at 1200°C for APMT [88].

The finite element simulation presented in this thesis focuses on the same type of analysis but on dissimilar alloys. APMT – Rene 80 and APMT – CM 247 LC bonds will be evaporatively–bonded in order to examine the axial stress distribution at the interface. The outcome of this analysis will also help to design a clamping system to be used for more complicated geometries. A similar model was used as before with the exception that

thermal expansion properties used were slightly different from those used previously by Braband [88]. This was because new CTE data were taken after it was discovered that oxidation had occurred on the TMA probe that may have affected the original results. In addition, thermal expansion data for TZM molybdenum were added for the full temperature range of 25 to $1200^{o}C$ while the previous simulation used a constant CTE value of 6E-06 m/m.^{o}C for the TZM molybdenum [102].

3.3.1 Boundary Conditions and Mesh Setup

The finite element analysis of the clamping assembly presented in this thesis was performed using ANSYS Workbench 14.5. Figure 3.13 (a) shows the finite element model along

(a) Boundary conditions

(b) Meshed model
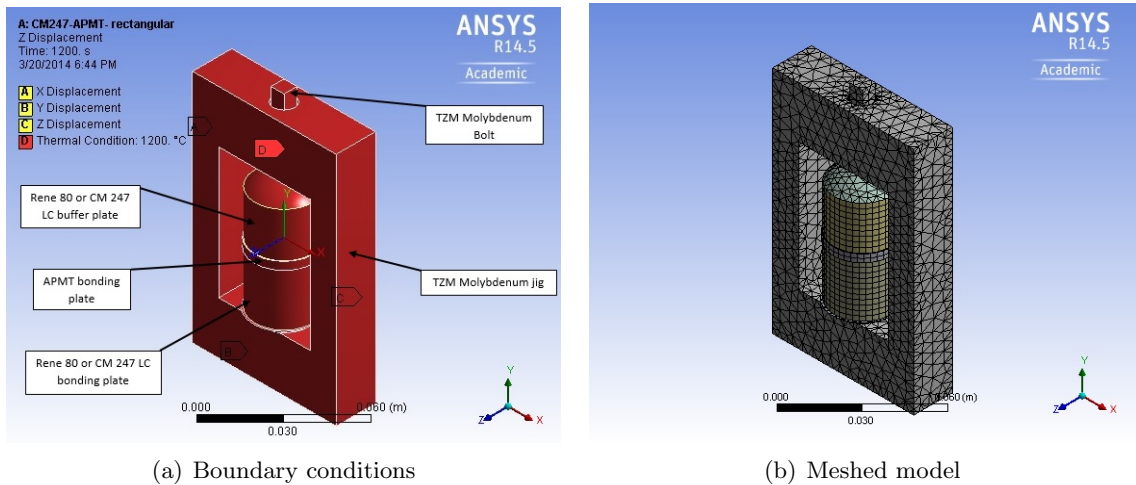
Figure 3.13: Finite element model used .

with boundary conditions constructed in ANSYS to model both the magnitude and the distribution of increasing bonding pressures. The temperature of the finite element model was increased while monitoring the stress distributions at the various interfaces. The mesh sizing of the models was determined from a mesh refinement convergence analysis. The model was meshed with a fine relevance center, high smoothing, fine span angle center, and the midside nodes were kept. The fine relevance center was chosen to decrease the default size of the elements in the mesh. The high smoothing and the fine span angle center were chosen so that the program would improve the mesh around the curves of the model. Having the midside nodes in the model enables an extra node at the center of each element edge,

which increases the order of the elements from linear to quadratic, which should increase the accuracy of the model [88]. The maximum allowable size of the edge of the elements was then varied and the maximum normal stress at the bonding surface was measured until it no longer changed. Table 3.4 shows the element size, number of nodes in the model corresponding to the given element size, the maximum stress at the bonding surface, and the percentage difference of the current element size from the next largest element size. Figure 3.14 shows a graph of the maximum stress at the bonding surface vs. the number of nodes in the model.

Table 3.4: Results from mesh refinement

Element size (mm)	Number of nodes	Max stress at bonding surface (Pa)	% difference
4	12291	2.62E+08	
3.5	19558	2.60E+08	-2
3	28959	2.60E+08	0.42
2.5	50985	2.59E+08	-0.65
2	75449	2.59E+08	-0.24
1.75	120018	2.59E+08	0.2
1.5	160884	2.59E+08	0.05
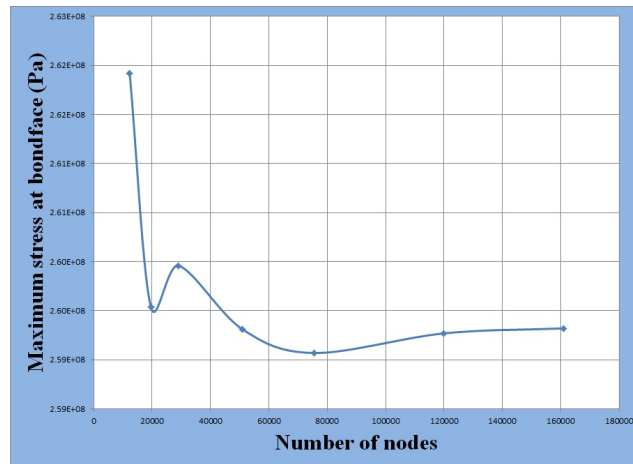
Figure 3.14: Maximum stress at the bonding surface vs. the number of nodes in the model.

The mesh refinement study showed that an element size of 2.5 mm created a mesh that was fine enough with a total of 50,985 nodes and 16,354 elements. This element size size was chosen because it yielded the lowest number of nodes, maximum stress and percent

difference values for our model. The final meshed model is shown on Figure 3.13 (b). The CME, CTE and Poisson's ratio (ν) for each material at room temperature were taken from References [4,98,99,101–104] and shown in Table 3.5. The other CTE values used from 100 to 1200°C were experimentally measured using a thermomechanical analyzer. CME values were also measured in this work for the same temperature range but they were not used in the ANSYS model because they were very small in magnitude as compared to the values reported in References [95,105,106]. Therefore constant CME values shown in Table 3.5 were used in the finite element model instead. The model was run in 12 steps taking data

Table 3.5: Engineering constants used in the finite element simulation [4,98,99,101–104,107].

	ν	CME (GPa)	CTE ($\mu\varepsilon/^o$C)
APMT	0.30	220	11
CM 247 LC	0.40	152	–
Rene 80	0.30	210	10
E52100 alloy steel	0.30	210	11.9
TZM molybdenum	0.38	330	6

starting at an ambient temperature of 25°C then at 100°C and at every subsequent 100°C increment all the way up to 1200°C. By performing the analysis in steps, transformation in the stress state can be observed. The stresses of most interest in this study were those at the bonding surface as those must be matched in future models of more complicated structures to assure that the same conditions are applied. The effects of some simulation parameters on the axial stress were investigated in order to optimize and validate the finite element model generated in ANSYS. These simulation parameters included the CTE variations, the types of boundary conditions and the APMT thicknesses.

3.3.1.1 Effect of CTE variations. Because the CTE values to be used were experimentally measured using the UND Thermomechanical analyzer there were some uncertainties on the measurements. Since the final CTE values were calculated as an average of three values, the idea here was to see how adding and subtracting the different standard deviation (stdev) to the mean CTE (α) will affect the maximum stress at the bonding surface. Three cases were considered according to data presented in Table 3.1. These cases

were: α, α – stdev and α + stdev. Their effects on the axial stress are presented on the graphs of Figure 3.15 (a) for the CM 247 LC – APMT joint and Figure 3.15 (b) for the Rene 80 – APMT joint.

(a) CM 247 LC – APMT   (b) Rene 80 – APMT

Figure 3.15: Effect of CTE variations on the maximum axial compressive stresses at the bonding surface for both joints.

It can be seen from Figure 3.15 (a) and Figure 3.15 (b) that subtle variations in CTE did not affect the normal stress distribution at the bonding surface of each joint. However, there were very small changes at 300^oC for both joints. For the CM 247 LC – APMT joint, adding the standard deviation reduced the normal stress by 1.49 MPa while subtracting the same standard deviation increased the normal stress by 1.5 MPa. For Rene 80 – APMT joint, adding the standard deviation reduced the normal stress by 1.74 MPa while subtracting the same standard deviation increased the normal stress by 1.74 MPa. Therefore it was concluded that the CTE values to be used would be those presented in Table 3.1. Another observation from Figure 3.15 (a) and Figure 3.15 (b) is that the bonding stress decreased with increasing temperature until about 900^oC and increased with increasing temperature after 900^oC. This change of mechanical behavior at 900^oC for both joints was most probably due to the increase in TZM molybdenum expansion rate which had almost doubled around 900^oC (from 0.75E-05 m/m.^oC at 100^oC to 1.2E-05 m/m.^oC at 900^oC) as shown in Table 3.2. In fact, any increase in expansion rate of the jig resulted in a certain amount of bonding stress being taken away from the bonding surface due to the fact that all contacts in the

74

ANSYS model were defined as *bonded* from 100 to 1200°C. Because of this high expansion, the bonding plates were forced to stretch away from the bonding surface, resulting in a decrease of bonding stress observed at the bonding surface

    3.3.1.2   Effect of boundary conditions. The goal here was to see how the type of constraint would affect the maximum compressive stress at the bonding surface. Two cases were considered: trinodal and trifacial constraints. In trinodal constraints the fixed nodes were chosen at the center of the face normal to the corresponding direction. The trinodal (or trifacial) constraint was done to account for the real–life situation where the TZM molybdenum jig is stiffer (expand less) compared to the bonding plates which have higher expansion coefficients. The jig was constrained in all the three directions to avoid the free–body situation but some degrees of freedom were constrained while some were set free to prevent the situation of over–constrained or under–constrained model. Compressive stresses were calculated at the surface separating the APMT and Rene 80 plates as well as between the APMT and CM 247 LC plates (bonding surface). Figure 3.16 (a) and Figure 3.16 (b) show the distributions of these compressive stresses for the different types of BC investigated.

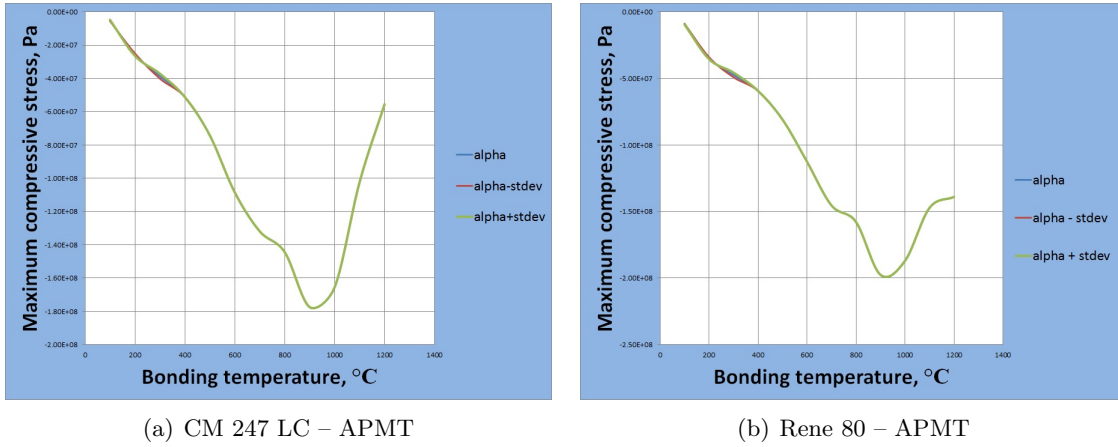(a) CM 247 LC – APMT   (b) Rene 80 – APMT
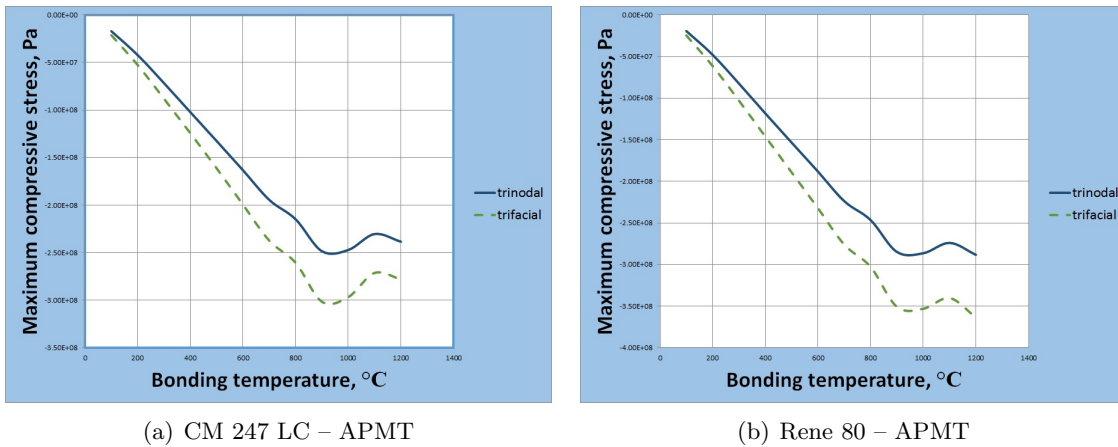
Figure 3.16: Effect of boundary condition on the maximum axial compressive stresses at the bonding surface for both joints.

    It can be seen from Figure 3.16 (a) and Figure 3.16 (b) that the type of BC did affect significantly the maximum compressive stress at the bonding surface for each joint. For

both types of joints, trinodal constraints yielded the the lowest values of the maximum axial compressive stress (249 MPa for the CM 247 – APMT joint and 288 MPa for the Rene 80 – APMT joint) while trifacial constraints yielded the highest maximum axial compressive stress values (302 MPa for the CM 247 – APMT joint and 364 MPa for the Rene 80 – APMT joint). Therefore it was concluded that the trinodal constraints will be applied to all future models since the goal was to minimize the compressive stresss at the bonding surface. The slight decrease in compressive stresses observed in Figure 3.16 (a) around 900°C was probably due to the increase in the rate of thermal expansion of TZM molybdenum and the drop in E52100 alloy steel CTE around that temperature.

3.3.1.3 Effect of APMT thickness. Because in the actual joint the bond coat is usually about 10 times or more less thick than the substrate, a thought was made to look at the effect of different APMT thicknesses on the distribution of normal stress at the bonding surface for each joint. Five cases were considered: 0.1 inch, 0.25 inch, 0.5 inch, 0.75 inch and 1 inch thick APMT vs. 1 inch thick substrate (Rene 80 or CM 247 LC) for each case. Figure 3.18 (a), Figure 3.18 (b), Figure 3.19 (a) and Figure 3.19 (b) show snapshots comparing a 0.1 inch and a 1 inch thick APMT bonding samples. Figure 3.17 (b) and Figure 3.17 (a) show the effects of the thickness on the normal stress distributions for each type of joint.

(a) Rene 80 – APMT   (b) CM 247 LC – APMT
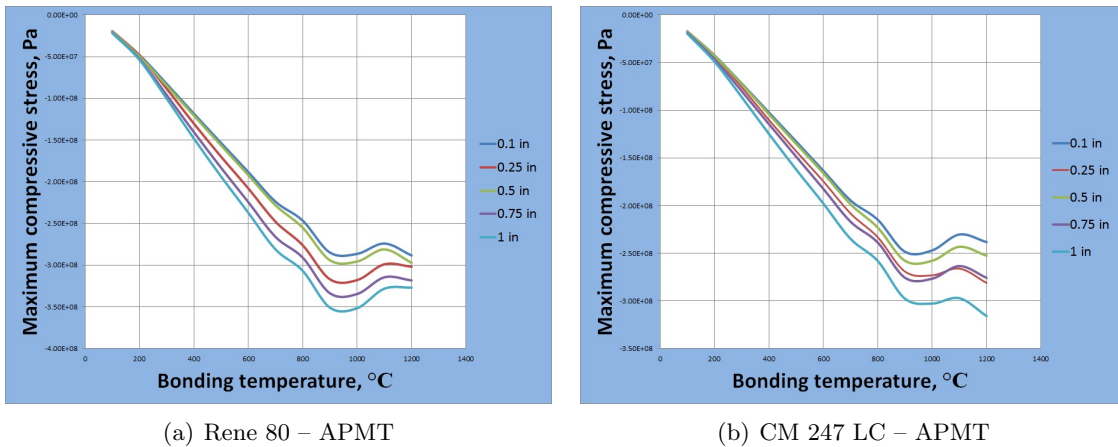
Figure 3.17: Effect of the APMT thickness on the maximum stress at the bonding surface.

(a) 0.1 inch thick APMT   (b) 1 inch thick APMT
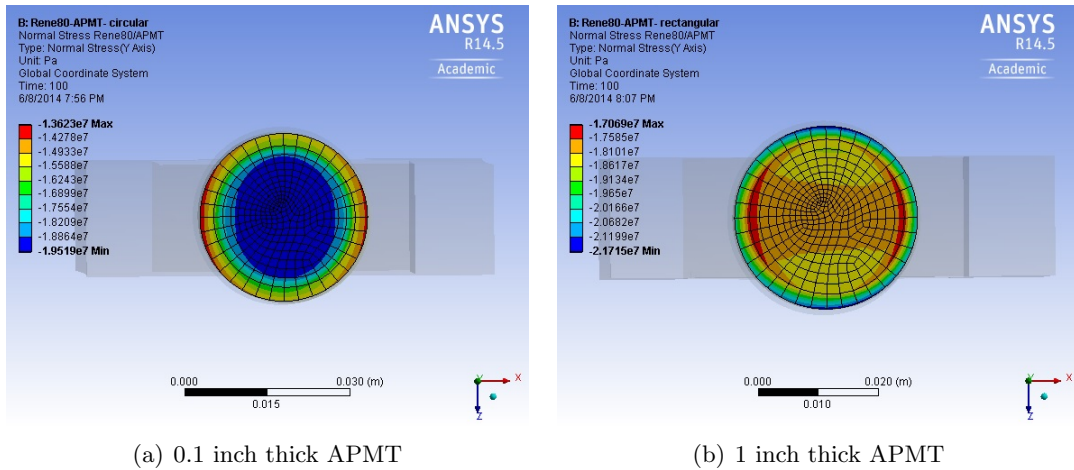
Figure 3.18: Comparison of APMT thicknesses with the maximum stress at 1200°C for Rene 80 – APMT joint.

From Figure 3.17 (a) and Figure 3.17 (b) it can be seen that the thinner the APMT layer the higher the axial compressive stress and the lower the axial tensile stress. For a joint with thin APMT there was high compression at the center and high tension at the edges but for a joint with a thick APMT there was high compression at the edges and high tension at the center as shown on Figure 3.18 (a), Figure 3.18 (b), Figure 3.19 (a) and Figure 3.19 (b). This observation showed that the effect of APMT thickness was consistent with the CTE measurements as the 1–inch thick APMT created more tensile–like stresses than the 0.1–inch thick one. Out of the different thicknesses considered, 0.1 inch yielded the lowest axial compressive stress values (248 MPa for the APMT – CM 247 LC joint and 288 MPa for the APMT – Rene 80 joint) while the 1–inch thich APMT yielded the highest axial compressive stress values (316 MPa for the APMT – CM 247 LC joint and 326 MPa for the APMT – Rene 80 joint). Since the goal was to minimize the axial stresses at the bonding surface (mostly at the center), it was decided to use the 0.1–inch thick APMT in all future models. A similar behavior was previously reported by Xiaoqin *et al.* [108] in the study of the effect of the Ti and Ti–Cu–Ti interlayers on the axial thermal stress distribution. They found that using the Ti–Cu–Ti interlayer the maximum axial compressive stress decreased from 139 MPa to 83.7 MPa towards the edge when using single Ti interlayer. Al–Ajaj *et*

(a) 0.1 inch thick APMT

(b) 1 inch thick APMT
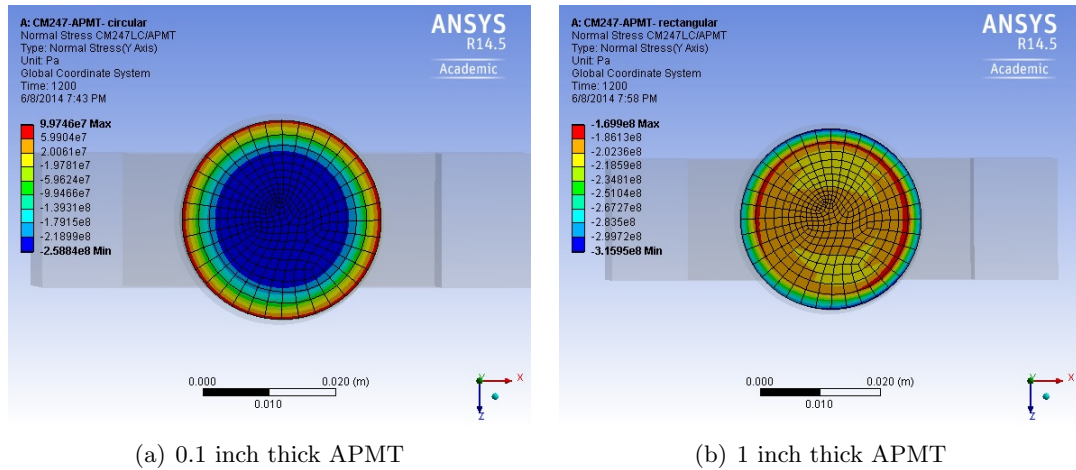
Figure 3.19: Comparison of APMT thicknesses with the maximum stress at 1200°C for CM 247 LC – APMT joint.

al. [90] also reported that the thinner the Ni interlayer the lower the compressive stresses at the interface (edges) when diffusion bonding Inconel 600 to pyrolytic graphite using Ni as interlayer.

3.3.2   Results and Discussion

3.3.2.1   Results. A full simulation was run at this point in order to include all previous conclusions. These conclusions included the use of simple CTE values, 0.1–inch thick APMT plate and a jig with three faces constrained each in the direction normal to it. The meshing was done using the same steps as described Figure 3.13 (a). Figures 3.20 (a) shows the normal stresses at 1200°C for Rene 80 – APMT samples while Figure 3.20 (b) shows the maximum compressive axial stresses at 1200°C for the CM 247 LC – APMT samples. The remaining stresses for the full temperature range of 100 to 1200°C are shown in Table 3.6.

3.3.2.2   Discussion. The accuracy of the model used in this thesis was checked by comparing the results obtained with previous works published by Ekrami *et al.* [94] on the diffusion bonding of Rene 80 to itself as well as the diffusion bonding of Al$_2$O$_3$-TiC to W$_{18}$Cr$_4$V published by Xiaoqin *et al.* [108].

From the snapshots of Figures 3.20 (a) and Figure 3.20 (b), it can be observed that the magnitude of the maximum compressive stresses were the lowest near the edge (99.74

(a) Rene 80 – APMT   (b) CM 247 LC – APMT
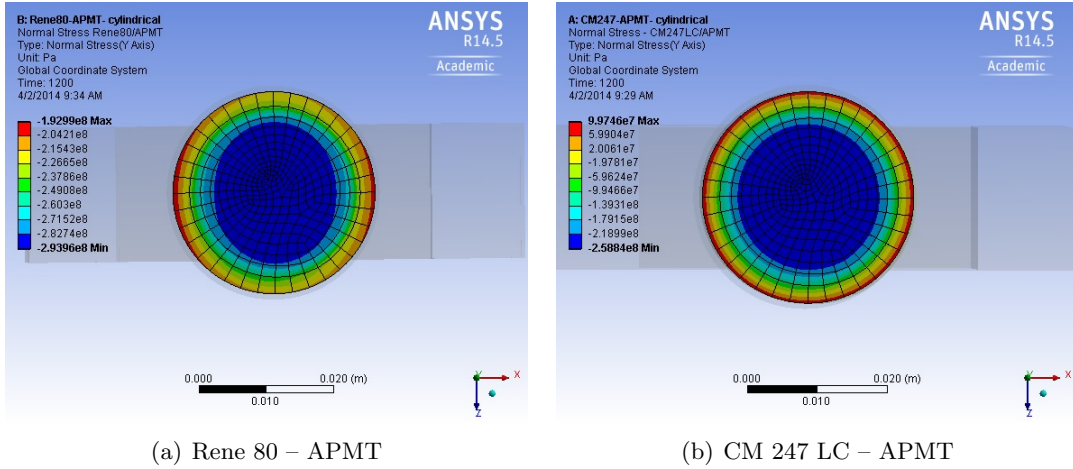
Figure 3.20: Maximum compressive axial stress distribution at the bonding surface at 1200^oC for Rene 80 – APMT and CM 247 LC – APMT (no preload) .

Table 3.6: Minimum and maximum compressive axial stresses of cylindrical samples (no preload).

T	Rene 80 – APMT		CM 247 LC – APMT	
^oC	Min (Pa)	Max (Pa)	Min (Pa)	Max (Pa)
100	-1.95E+07	-1.36E+07	-1.73E+07	-1.20E+07
200	-4.84E+07	-3.49E+07	-4.28E+07	-2.83E+07
300	-8.54E+07	-3.44E+07	-7.39E+07	-3.00E+07
400	-1.24E+08	-3.39E+07	-1.06E+08	-2.91E+07
500	-1.61E+08	-3.88E+07	-1.38E+08	-3.70E+07
600	-1.97E+08	-4.96E+07	-1.69E+08	-5.65E+07
700	-2.35E+08	-6.11E+07	-2.02E+08	-6.93E+07
800	-2.59E+08	-7.26E+07	-2.23E+08	-7.58E+07
900	-2.99E+08	-9.57E+07	-2.58E+08	-9.19E+07
1000	-3.00E+08	-1.01E+08	-2.59E+08	-4.92E+07
1100	-2.85E+08	-1.24E+08	-2.47E+08	4.65E+07
1200	-2.94E+08	-1.93E+08	-2.59E+08	9.97E+07

MPa for the APMT – CM 247 LC joint and 192.99 MPa for the APMT – Rene 80 joint) and the highest near the center (258.84 MPa for the APMT – CM 247 LC joint and 293.96 MPa for the APMT – Rene 80 joint) of the joint. This observation is in good agreement with the previous results published by Xiaoqin *et al.* [108] in which they showed that the axial stresses changed greatly near the edge of the joint and have a uniform distribution near the central axis. For both type of joints, the normal stress starts from a minimum value at the center then increases to a maximum value at about 3/4 of the way but the decreases again to a medium value at the edge. The negative signs of the normal stresses simply indicate a state of compression on the face of interest (bonding surface) which was the surface between the APMT and the Rene 80 or CM 247 LC samples.

Another important observation is that the maximum compressive stresses at the bonding surface increased as the temperature increased for each model. This increase was due to the fact that each material involved in the bonding process expanded with increasing temperature. Also the TZM molybdenum jig, which was used to hold the bonding samples in place, had the lowest CTE what put more pressure on the bonding samples as the temperature increased. This also explains the high axial stress values observed on the edges supported by the jig in both cases. The uniform distibution observed in those joints was simply due to the uniform expansion of each superalloy involved in the bonding process. At 1200°C, Rene 80 – bonding surface showed a maximum axial compressive stress of 260 MPa which was about 1.5 times the axial compressive stress of the CM 247 LC – APMT bonding surface of 168 MPa. The reason was that Rene 80 has a CTE higher than that of CM 247 LC meaning that during the heating process, Rene 80 expands more but is constrained by the TZM molybdenum jig which then pushes back leading to a higher compression on the bonding surface.

The next step was to predict stress distributions in samples at an industrial scale. The effects of some model features on the maximum normal stresses at the bonding surface were investigated in order to better predict the thermal behavior of each joint. The features investigated were: the geometry of the jig, the shape of the bonding sample, and the shape

of the buffer plate.

3.3.2.2.1   *Effect of jig geometry.* Two potential configurations were considered in each case for the fabrication of larger samples. Figure 3.21. (a) and Figure 3.21 (b) show the full–plate (configuration 1) and multiple–jig (configuration 2) potential jig configurations. Configuration 1 consisted of two plates of TZM molybdenum which were larger than the specimens to be joined and a set of bolts regularly arranged and spaced to allow an evenly distribution of pressure to the bonding samples. Additional holes may be drilled as needed if the bonding specimens seem to be loose. The total number of bolts would depend on the length of the specimen needed. Configuration 2 consisted of a set of TZM molybdenum jigs clamped along the bonding samples. The jigs were identical and had the same geometry as in Figure 3.13 (a).

(a) Configuration 1   (b) Configuration 2
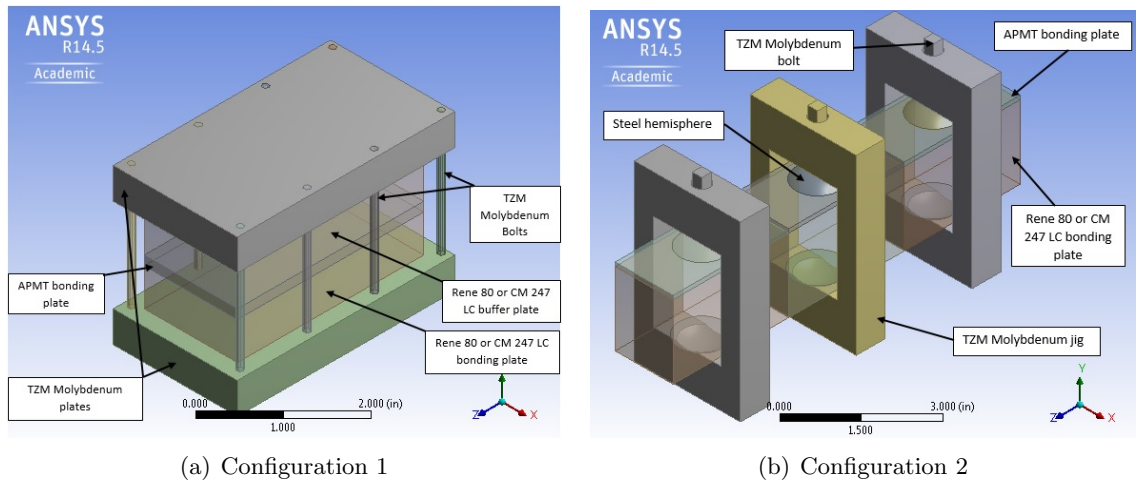
Figure 3.21: Potential jig configurations .

Configuration 2 required more machining of TZM molybdenum than configuration 1 but offered more open space for zinc evaporation than configuration 1. Moreover, configuration 2 could easily be adapted to produce specimens of more intricate geometries as compared to configuration 1 which was only appropriate for making specimens with simple geometries. A look at Figure 3.22 (a) and Figure 3.22 (b) revealed that configuration 1 yielded the highest values of the maximum compressive stresses (5.1 GPa for the Rene 80 – APMT joint and 3.66 GPa for the CM 247 LC – APMT joint) across the bonding surface (surface between the

(a) Configuration 1   (b) Configuration 2
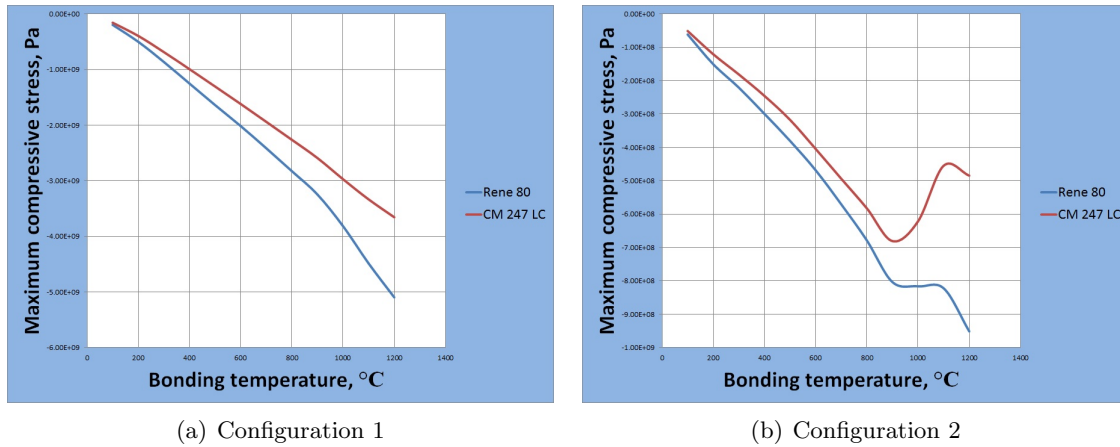
Figure 3.22: Effect of the jig geometry on the maximum stress at the bonding surface.

APMT and Rene 80 or CM 247 LC plates) while configuration 2 yielded the lowest values of the maximum compressive stresses (952 MPa for the Rene 80 – APMT joint and 681 MPa for the CM 247 LC – APMT joint). Because the goal was to minimize the compressive stresses at the bonding surface, configuration 2 was finally considered for use in the making of larger samples and also because it offered more flexibility and opportunities. The change of mechanical behavior (reduction in compressive stresses) observed in configuration 2 at about 900°C was due to the fact that the jig did not entirely cover the bonding samples as in configuration 1. The portion of the bonding plates not covered by the jig expanded freely resulting in more tensile–like stresses at the bonding surface. Configuration 1 provided more contact with the bonding samples therefore higher compressive stress as compared to configuration 2. Because of the low expansion values of the TZM molybdenum, the jig used acted as compressive load towards the bonding samples. The behavior observed in Figure 3.22 (a) was in good agreement with the behavior reported by Xiaoqin *et al.* [108] in the study of the effect of pressure on the axial stress distribution. They showed that the compressive stress increased from 72.1 to 101 MPa when the pressure improved from 5 to 30 MPa.

3.3.2.2.2   *Effect of bonding sample shape.* Two configurations were considered regarding the bonding sample shapes: elliptical and rectangular. The elliptical configuration was considered for the sake of symmetrical distribution of pressure applied through the

bolt while the rectangular configuration was considered for the reason of simplicity in its fabrication. Figure 3.23 (a) and Figure 3.23 (b) show the elliptical and rectangular shapes of the samples to be bonded. The effects of the different shapes on the maximum compressive stresses are shown on Figure 3.24 (b) for the CM 247 LC – APMT joint and Figure 3.24 (a) for the Rene 80 – APMT joint.

(a) Configuration 1   (b) Configuration 2
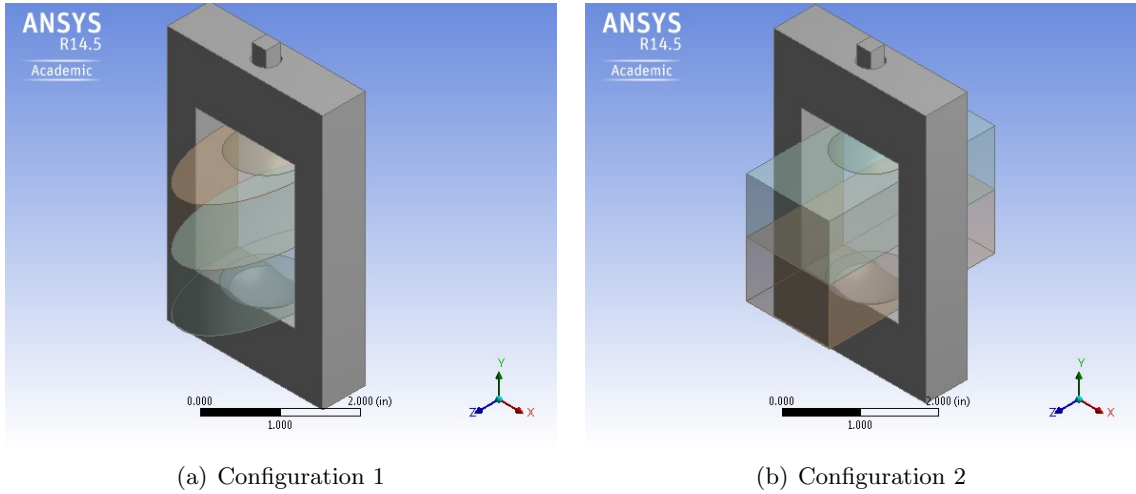
Figure 3.23: Potential sample configurations .

(a) Rene 80 – APMT   (b) CM 247 LC – APMT

Figure 3.24: Effect of bonding sample shape on the maximum stress at the bonding surface .

It can be seen from Figure 3.24 (b) and Figure 3.24 (a) that the elliptical configuration showed the highest values of the maximum compressive stresses (224 MPa for the Rene 80 – APMT and 204 MPa for the CM 247 LC – APMT) than the rectangular configuration which
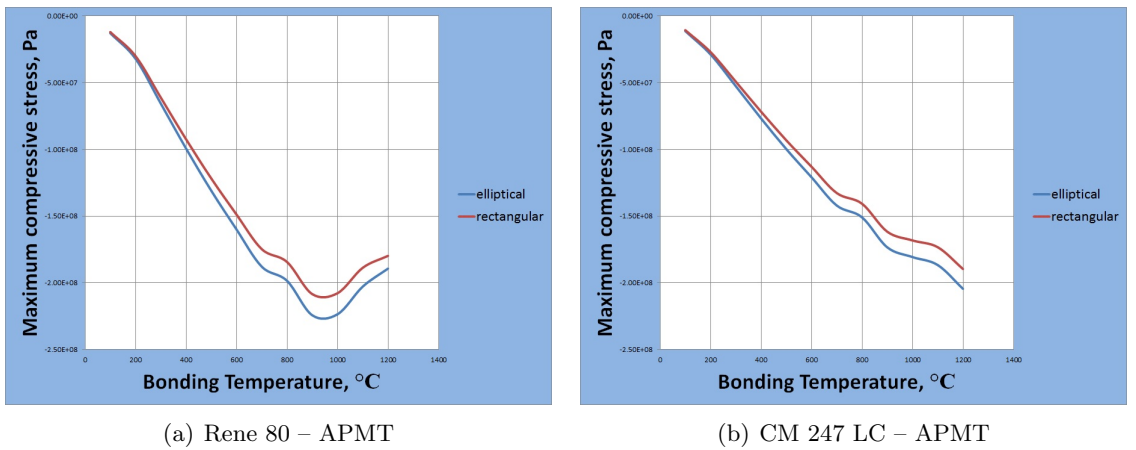
showed the lowest values (208 MPa for the Rene 80 – APMT and 190 MPa for the CM 247 LC – APMT). But the elliptical configuration was later discarded due to the fact that making samples of those shape would cause a great lost of material despite the fact that it exhibited higher compressive stresses than the rectangular configuration. Moreover, the bonding plates provided by Kanthal and Siemens Energy had rectangular shapes, therefore making specimens of elliptical shape would require considerable machining time and material waste. Rectangular shape was finally considered for used in the fabrication of larger bilayered structures but with the exception that a buffer will be added above the the thin APMT plate to increase the compressive stresses at the bonding surface.

3.3.2.2.3 ***Effect of buffer plate shape.*** The buffer was introduced to ensure an effective distribution of pressure across the bonding surface of the new bonding assembly model in which the APMT plate was thinner than the Rene 80 or CM 247 LC plate. Two types of buffer shapes were considered: cylindrical and rectangular as shown in Figure 3.25 (a) and Figure 3.25 (b).

(a) Cylindrical configuration   (b) Rectangular configuration
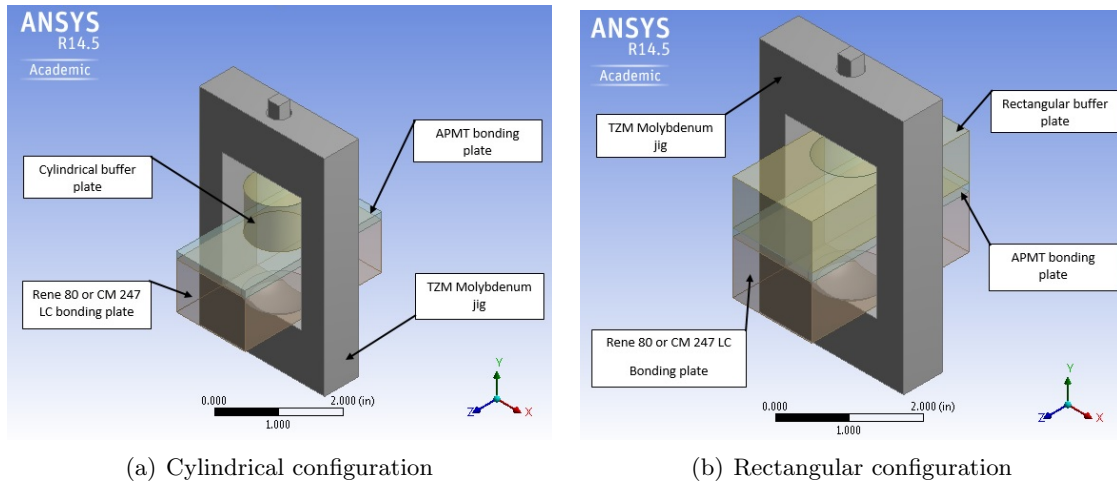
Figure 3.25: Potential buffer configurations .

The effects of the different buffer plate shapes on the maximum compressive stresses acrosss the bonding surface (surface between the APMT and Rene 80 or CM 247 LC bonding plates) are shown on Figure 3.26 (a) for the Rene 80 – APMT joint and Figure 3.26 (b) for the CM 247 LC – APMT joint. The boundary conditions (trinodal constraint) and

mesh were set up using the same steps and features as described in previous sections (Figure 3.13 (a)).

(a) Rene 80 – APMT

(b) CM 247 LC – APMT
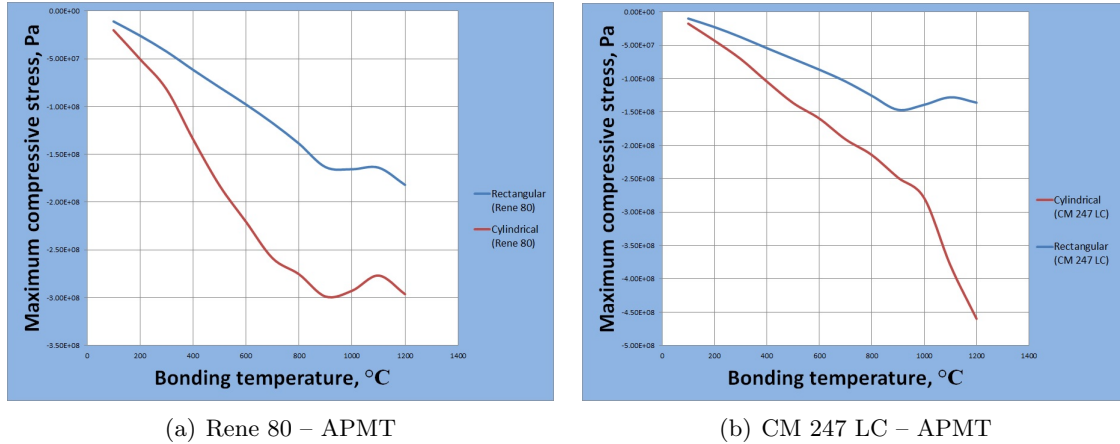
Figure 3.26: Effect of the buffer plate shape on the maximum compressive stress at the bonding surface for both joints .

From Figure 3.26 (a) and Figure 3.26 (b) it can be seen that the cylindrical configuration yielded the highest value of the maximum compressive stresses in both types of joints (299 MPa for the Rene 80 – APMT joint and 460 MPa for the CM 247 LC – APMT joint) compared to the rectangular configuration (182 MPa for the Rene 80 – APMT joint and 147 MPa for the CM 247 LC – APMT joint). But these compressive stresses were not distributed across the entire bonding surface as they quickly faded away from the center creating more tensile–like stresses as shown on the snapshots of Figure 3.27 and Figure 3.28. In fact, the cylindrical buffer shown in Figure 3.25 (a) covered an area of about 1 square–inch on the joint stress distribution for both types of joints. At 1200°C, in the CM 247 LC – APMT joint, compressive stresses directly below the edge of the rod were approximately 154 MPa. Approximately 5 mm beyond the edge of the rod, these stresses were reduced to about 29 MPa. In the Rene 80 – APMT joint, stresses directly below the edge of the rod were approximately 230 MPa. The stresses reduced to approximately 88 MPa at about 7.5 mm beyond the edge of the rod. Figure 3.27 and Figure 3.28 revealed the rectangular configuration of the buffer provided a more widespread compressive stresses across the bonding surface. There were very few tensile stresses observed at the edges of the bonding

surface using the rectangular configuration as compared to the cylindrical configuration which had much more tensile stresses across the bonding surface. Because the goal was to have a bonding model with high compressive stresses across the entire bonding surface, the rectangular configuration was considered for use in the making of bi–layer structures of Rene 80 – APMT and CM 247 LC – APMT even though it yielded compressive stresses lower than those yielded by the cylindrical configuration. Besides, using the cylindrical configuration would require that a model having two 30 mm steel hemispheres along with several TZM molybdenum bolts (one bolt per jig) spaced approximately 45 mm center–to–center for compressive stresses to be maintained in the desired range. The snapshots showing the effects of buffer plate shape on the compressive stress distributions at other temperatures (100^oC, 300^oC, 600^oC and 900^oC) can be found in the appendix of this thesis.

(a) Cylindrical configuration   (b) Rectangular configuration

Figure 3.27: Snapshots of the distribution compressive stress at the bonding surface at 1200^oC for the CM 247 LC – APMT joint (no preload) .

The transition from compressive–like stresses at the center to tensile–like stresses toward the edge of each specimen observed on the snapshots of Figure 3.27 and Figure 3.28 is believed to be related to the nature of the contact condition applied at the interface of the APMT with the base metal. The contact was set to *bonded*, which caused more tension on the bonding surface as the system was being heated up. This was due to the increase in thermal expansion of the TZM molybdenum jig, which forced the bonding samples to

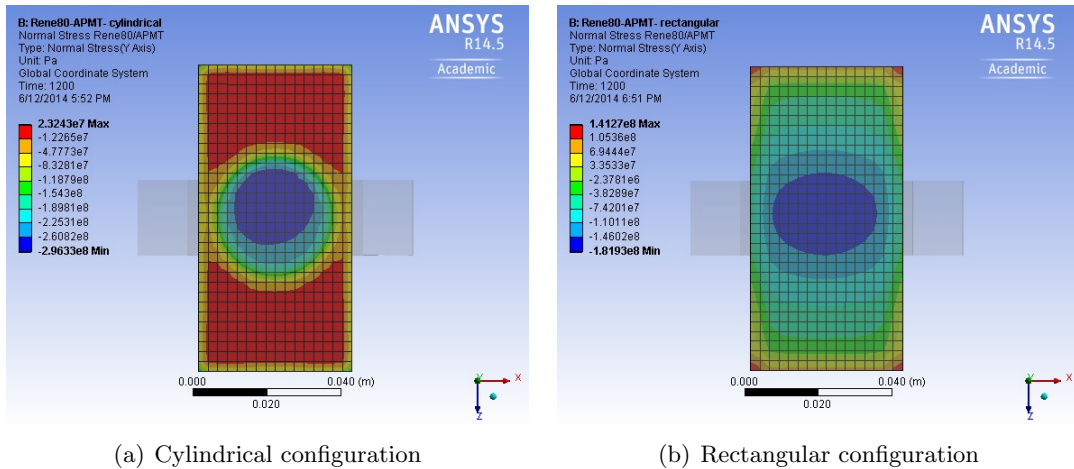(a) Cylindrical configuration   (b) Rectangular configuration
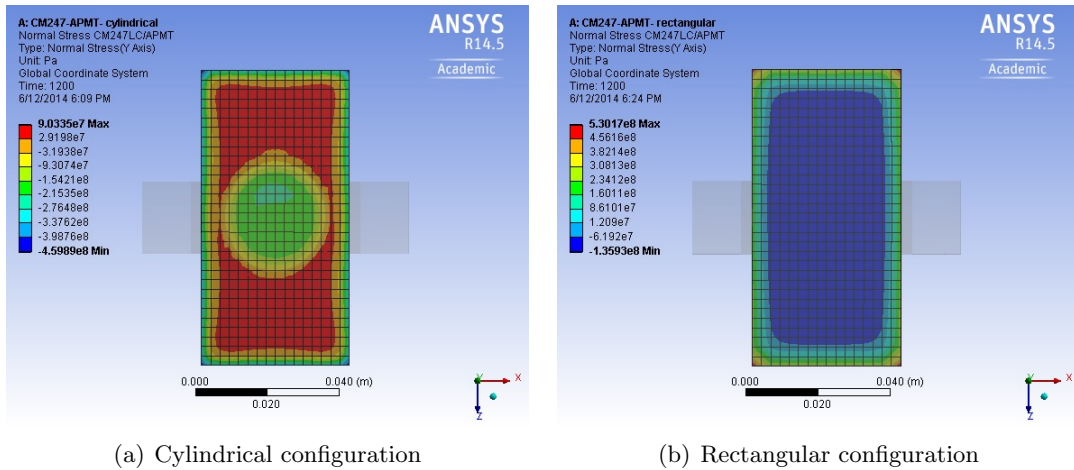
Figure 3.28: Snapshots of the distribution compressive stress at the bonding surface at $1200^{o}C$ for the CM 247 LC – APMT joint (no preload) .

stretch further away from the bonding surface.

3.4   Summary

The main goal of this chapter was to predict the thermally–induced stresses distribution in the bilayered structures of Rene 80 – APMT and CM 247 LC – APMT. This was done by simulating their thermal behavior from 25 to $1200^{o}C$. CTE values used in the finite element model were experimentally measured using the UND Mechanical Engineering Thermome- chanical analyzer. The optimization of the model was done through the investigations of the effects of various parameters on the maximum stress distribution at the bonding surface. These parameters were: the CTE variation, the type of boundary condition, the APMT thickness, the shape of the bonding sample, the geometry of the jig and the shape of the buffer plate.

The study of the effect of CTE variations on the maximum stress at the bonding sur- face revealed that subtle variations of CTE had no effect on the stress distribution. This was due to the fact that the calculated standard deviation values were very small as the measured CTE values were very close to each others. Among the two types of boundary conditions investigated, the trinodal constraints were considered to be the best fit as they yielded the lowest axial stress values at the bonding surface. Five different thicknesses were chosen to check the effect of the APMT thickness on the maximum stress at the bonding

surface. The APMT thickness of 0.1 inch was retained as the ideal thickness as it created more compressive–like stresses than tensile–like ones. But it was concluded that a buffer plate was needed above the APMT sample to increase the compressive stresses at the bonding surface and mostly to make sure that the APMT stayed in contact with the substrate during the entire bonding process. For the effect of the bonding sample shape, the rectangular configuration was finally considered because of the ease in its fabrication. For the effect of the jig geometry, it was shown that the multijig configuration was best suited as clamping sytem for the fabrication of Rene 80 – APMT and CM 247 LC – APMT bilayered structures. This was due to the fact that it provided more space for zinc evaporation during the diffusion bonding process despite the fact that the multiplate configuration yielded higher compressive stresses at the bonding surface. For the buffer plate shape, the rectangular configuration was finally considered as it provided a more widespread distribution of compressive stresses across the bonding surface even though these stresses were smaller in magnitude as compared to those provided by the cylindrical configuration.

CHAPTER IV

CONCLUSION

Rene 80 – APMT and CM 247 LC – APMT joints were investigated so as to assess their behavior in high temperature environments as they appear to be very promising materials for use in gas turbine parts manufacturing. The high temperature behavior study consisted of finding what types of microcontaminants were present in the syngas produced using the EERC pilot–scale gasifiers as well as finding the magnitude of bonding stresses created at the different bonding faces using ANSYS Workbench. The CTE values were experimentally measured using the UND Mechanical Engineering thermomechanical analyzer and APMT small cylindrical plates were successfully plated onto Rene 80 and CM 247 LC cylindrical plates. These data along with other material properties found in literature were used as input for the simulation process in ANSYS Workbench.

The syngas microcontaminants characterization revealed the presence of several elements trapped on the filter surfaces and in the impinger solutions. The elements of most concern were: V, Na, K, Pb, and Ca. This was because their presence in significant amount usually leads to blades fouling and severe corrosion of the GT materials, resulting in the reduction of the overall efficiency of the GT. The significance level (expressed in terms of parts per million of fuel equivalent content) of the samples collected in this work satisfied the tolerance of less than 2 ppmw recommended by GT manufacturers except for Si and S which had respective ppmw values of 3.69 and 4.6 for Test 4–2012. The high sulfur–content was most probably due to the fact that no sulfur removal was used during that run. The high silicon–content was most likely coming from the rust present at the bottom of the TOx and some of that silicon might have come from the inner walls of the stainless steel pipes used to transport the syngas. For this reason, the level of contamination by trace metals should be of interest and concern to all gas turbine users irrespective of the type of fuel used.

The low ppmw values measured showed that the syngas produced at the UND–EERC was of good quality and could be tolerated by any industrial GT without posing any safety risks. But because these low ppmw values could still trigger the hot corrosion of GT materials in a long–term, the bilayered structures of Rene 80 – APMT and CM 247 LC diffusion–bonded using the EMB process will be subjected to corrosion testing in order to understand their behavior in the type of syngas such as the one produced at the UND–EERC.

Finite element simulations revealed a general trend according to which the compressive stresses were relatively uniform at the center and increased to a maximum at about 3/4 of the way before before decreasing to a minimum value towards the edge. This appeared to be in good agreement with some of the previous results found in the literature. The optimization of the finite element model was done by studying the effects of parameters such as the CTE variation, the types of boundary condition, the APMT thickness, the bonding sample shape, the jig geometry and the buffer plate shape on the maximum compressive stress distribution across the bonding surface (surface between the APMT and Rene 80 or CM 247 LC plates). It was shown that subtle variations in CTE had no effect on the stress distribution as the calculated standard deviation values were very small due to the closeness of the measured CTE values. Among the two types of boundary conditions investigated, the trinodal constraints were considered to be the best fit as they yielded the lowest axial stress values at the bonding surface. Five different thicknesses were chosen to check the effect of the APMT thickness on the maximum stress at the bonding surface. The APMT thickness of 0.1 inch was retained as the ideal thickness as it created more compressive–like stresses than tensile–like ones. But it was concluded that a buffer plate was needed above the APMT sample to increase the compressive stresses at the bonding surface and mostly to make sure that the APMT stayed in contact with the substrate during the entire bonding process. For the effect of the bonding sample shape, the elliptical configuration had a more uniform distribution of compressive stresses across the bonding surface but the rectangular configuration was finally considered because of the ease in its fabrication. For the effect of the jig geometry, it was shown that the multijig configuration

was best suited as clamping sytem for the fabrication of Rene 80 – APMT and CM 247 LC – APMT bilayered structures. This was due to the fact that it provided more space for zinc evaporation during the diffusion bonding process despite the fact that the multiplate configuration yielded higher compressive stresses at the bonding surface. For the buffer plate shape, the rectangular configuration was finally considered as it provided a more widespread distribution of compressive stresses across the bonding surface even though these stresses were smaller in magnitude as compared to those provided by the cylindrical configuration.

APPENDICES

Appendix A

Description of the EERC Gasifier Equipment used

A.2 High Pressure Fluidized–Bed Gasifier

The HP–FBG used at the UND–EERC is capable of feeding up to 9.0 kg/hr (20 lb/hr) of pulverized coal or biomass at pressures up to 70 bar absolute (1000 psig). The externally heated bed is initially charged from an independent hopper with silica sand, but through time the bed converts to coal ash. Independent mass flow controllers meter the flow of nitrogen, oxygen, steam, and recycled syngas into the bottom of the fluid bed. Various safety interlocks prevent the inadvertent flow of pure oxygen into the bed or reverse flow into the coal feeder. Recycled syngas is injected several inches above the bottom distributor plate, which prevents direct combustion of syngas with oxygen entering at the bottom of the bed. The feed system uses a K–tron loss–in–weight feeder setting inside of the pressure vessel capable of 6.9 MPa (1000 psig) operation. A design drawing and a photograph of the fuel feeder system are shown in Figure A.1. This system allows a real–time measurement of the fuel feed rate to the gasification system. The feed system electronic controls are interfaced to a data acquisition system that allows for local or remote computer control of the fuel feed rate. Power and electronic signals to and from the feeder are through two isolation fittings on the pressure vessel. The upper pressure vessel is the fuel charge hopper. The fuel charge hopper is manually charged with fuel through the top valve while at atmospheric pressure. It is then sealed and pressurized. Finally, the fuel feed material is transferred by gravity feed to the weigh hopper inside through the lower dual–valve system. The weigh hopper is on an integral platform scale that provides an electronic signal of the overall weight of the fuel feed material. Hopper weights along with feed rates are recorded by the data acquisition system and can be displayed and trended as required. The feed system pressure vessel is on a movable platform to allow easy transition from one gasifier

to the other. An internal mixer allows for the feeding of more difficult materials such as biomass materials to be completed on this system. During operation of the system, fly ash is captured in a hot–gas filter vessel (HGFV) that uses an iron aluminide candle filter, providing near–absolute filtration. The gas then passes through water–gas shift reactors that can shift sour gas (containing H_2S) to increase its H_2 concentration. The gas then passes through water quench pots to remove tars and a portion of the H_2S. A portion of this gas is then sent to a piece of technology and the rest is combusted in the thermal oxidizer from which the M29 and M26–A samples are collected. Approximately 85% of the 2500 ppm of H_2S in the gas is removed with a zinc–based fixed–bed sorbent system before the thermal oxidizer.

A.3 Entrained–Flow Gasifier

The UND–EERC EFG is a dry–feed, downfired system. The reactor tube is vertically housed in a pressure vessel approximately 24 inches in diameter and 7 ft in length. It fires nominally 8 lb/h of coal and produces up to 20 scfm of fuel gas. The maximum allowable working pressure is 300 psig. The reactor has the capability to run in oxygen– or air–blown mode. The supplemental electrical heating system is capable of reaching a nominal temperature of 1500^oC (2732^oF) and is separated into four independent zones so that a consistent temperature can be maintained throughout the length of the furnace. The radially spaced heating elements provide the initial heat for the centrally located alumina reactor tube, and refractory walls outside the heating elements provide insulation. Type S thermocouples are used to monitor and control the temperatures of the heating zones and reactor tube. All of the gasification reactions occur inside the reactor tube, and slag is able to flow on the tube walls. Pressure inside the alumina reactor tube is balanced with a slightly positive nitrogen pressure outside of the alumina reactor tube. Pulverized coal is fed into the top of the furnace via a twin–screw feeder and scale contained in a pressurized vessel. A lock hopper is in place that allows the system to be refilled while running, thereby facilitating a continuous mode operation. Feed rates are calculated in real time. The feed system can be run in either volumetric mode or gravimetric mode. Nitrogen or syngas is used to convey the solid pulverized coal into the combustion zone. Product gas

Figure A.1: Photograph of the EERC fluid–bed coal feed system.

exits at the bottom of the furnace tube and enters a reducing section that houses a quench system capable of injecting water, syngas, or nitrogen as the quench fluid. The product gas then enters a cross, making a 90° turn, and then exits the main unit on its way to the back–.end control devices. Slag, ash, and char drop through the cross and are collected in a refractory–lined slag trap. Fine particulate is able to flow with the gas through the 90° turn and is collected in a downstream filter. The overall system layout for the test run is shown in Figure 2.1. Slag is collected below the gasifier in a refractory–lined slag trap. Fly ash is captured in the hot–gas filter vessel (HGFV) that uses an iron aluminide candle filter, providing near–absolute filtration. Drger tube samples can be taken in the HGFV, measuring for ammonia, HCN, HCl, and H_2S. The gas then passes through water–gas shift reactors that can shift sour gas (containing H_2S) to increase its H_2 concentration. A portion then goes through sulfur adsorbers and then to hydrogen separation membranes that were tested during this run. The portion not going to the separation membranes is quenched to remove moisture and any tars formed in the system. All gas streams, including the membrane raffinate and permeate streams, are then recombined before combusting them in the thermal oxidizer from which the M29 samples are collected.

Figure A.2: Photograph of the Thermal Oxidizer used.

A.4 Thermal Oxidizer

The thermal oxidizer contains a burner at the top of a refractory–lined chamber that admits the syngas and air separately and also includes a premixed natural gas and air supplemental gas stream. An accurate flame temperature is not available for the thermal oxidizer because thermocouples burn out too quickly in the flame. The sampling occurs at the bottom of the downfired oxidizer. The gas being sampled is at approximately 750^oC. It is quenched as it is pulled through the glass sampling tube to approximately 100^oC before reaching the filter. The HP–FBG was designed according to ASME B31.3 Process Piping Code specifications. After a review of available alloys, Haynes 556 was selected as the material most suitable for fabrication of this high–temperature, high–pressure system. The reactor was designed with the capability to operate at 6.9 MPa (1000 psig) at an operational temperature of 843^oC (1550^oF), 4.5 MPa (650 psig) at an operational temperature of 917^oC (1650^oF), and 2.0 MPa (300 psig) at an operational temperature of 1800^oF. This system is externally electrically heated. Haynes 556 alloy was selected as the material of construction for the reactor, all the reactor nozzles, and the cyclone. A photograph of the thermal oxidizer used is shown in Figure A.2.

Appendix B

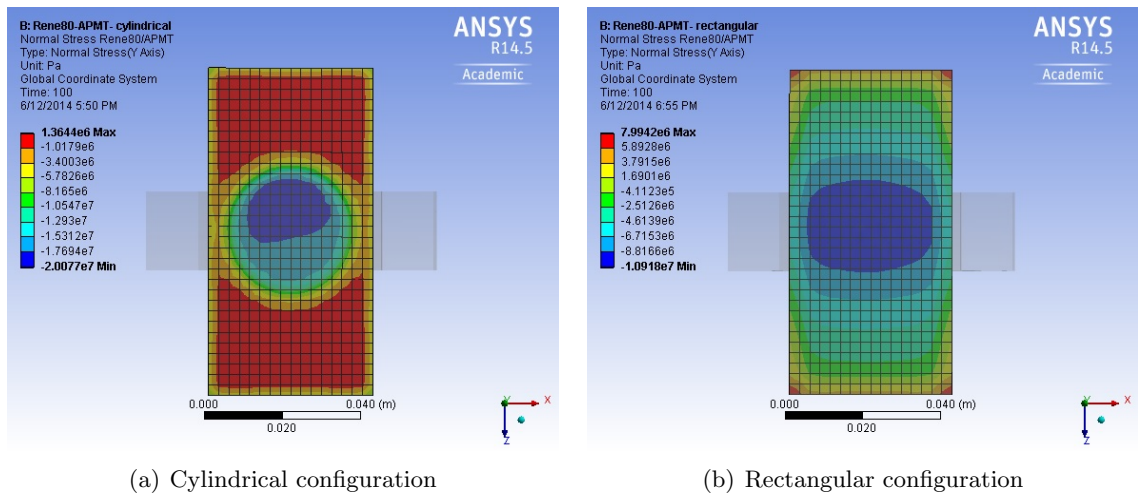# Effects of buffer shape on the compressive stress distributions

(a) Cylindrical configuration

(b) Rectangular configuration

Figure B.1: Snapshots of the distribution of compressive stresses at the Bondface at 100°C for the Rene 80 – APMT joint (no preload) .

(a) Cylindrical configuration

(b) Rectangular configuration

Figure B.2: Snapshots of the distribution of compressive stresses at the Bondface at 300°C for the Rene 80 – APMT joint (no preload) .

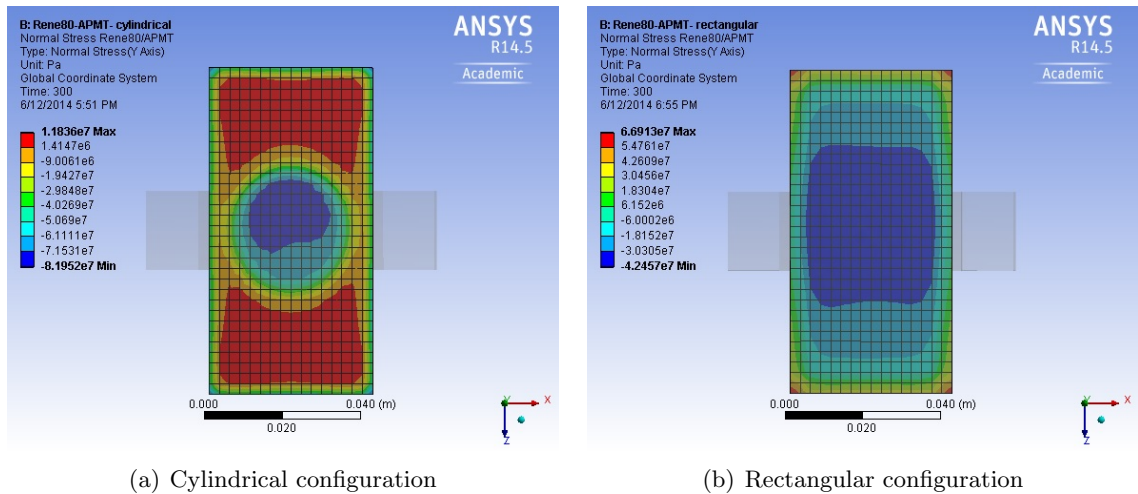(a) Cylindrical configuration
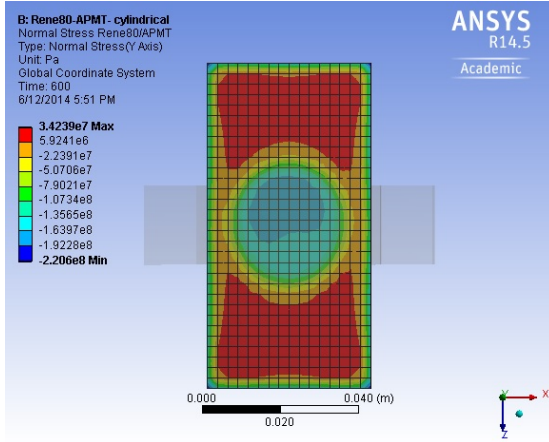
(b) Rectangular configuration

Figure B.3: Snapshots of the distribution of compressive stresses at the Bondface at 600°C for the Rene 80 – APMT joint (no preload) .

(a) Cylindrical configuration

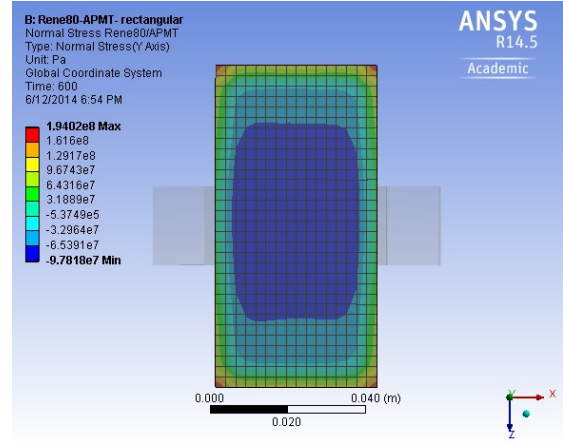(b) Rectangular configuration

Figure B.4: Snapshots of the distribution of compressive stresses at the Bondface at 900°C for the Rene 80 – APMT joint (no preload) .
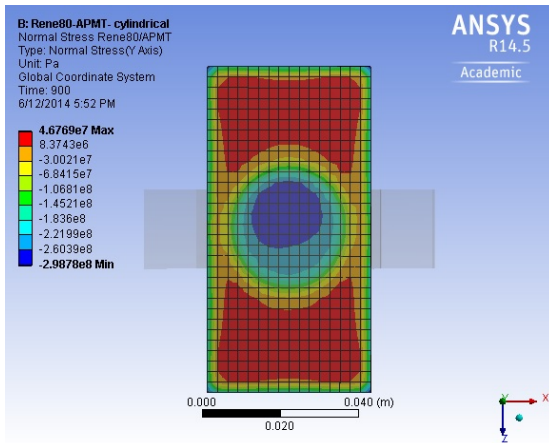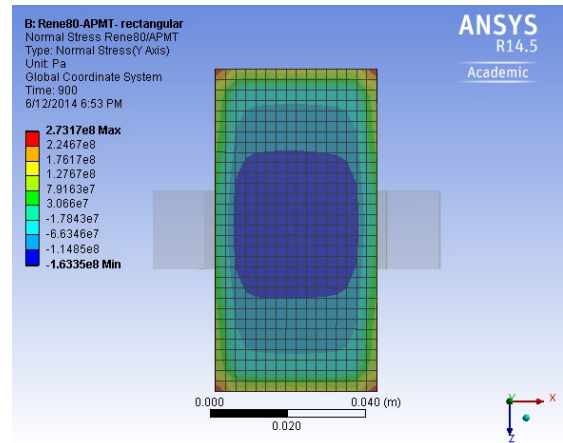
(a) Cylindrical configuration

(b) Rectangular configuration

Figure B.5: Snapshots of the distribution of compressive stresses at the Bondface at 100°C for the CM 247 LC – APMT joint (no preload) .

(a) Cylindrical configuration

(b) Rectangular configuration

Figure B.6: Snapshots of the distribution of compressive stresses at the Bondface at 300°C for the CM 247 LC – APMT joint (no preload) .

(a) Cylindrical configuration

(b) Rectangular configuration

Figure B.7: Snapshots of the distribution of compressive stresses at the Bondface at 600°C for the CM 247 LC – APMT joint (no preload) .
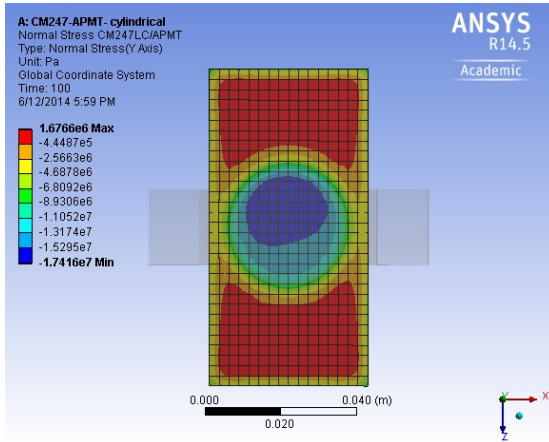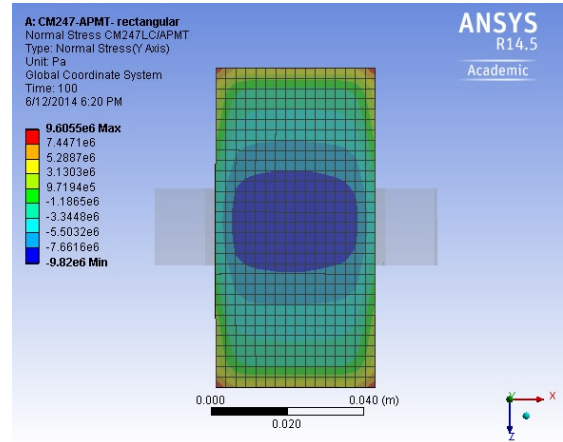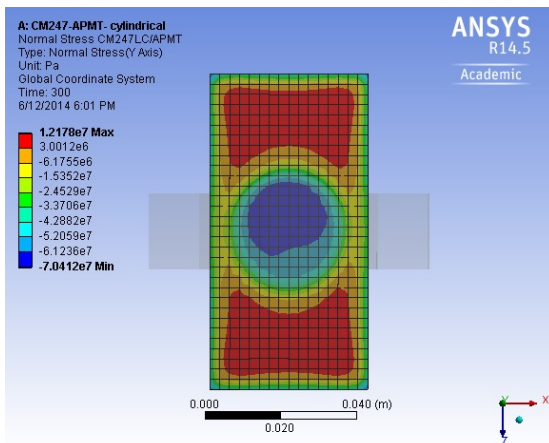

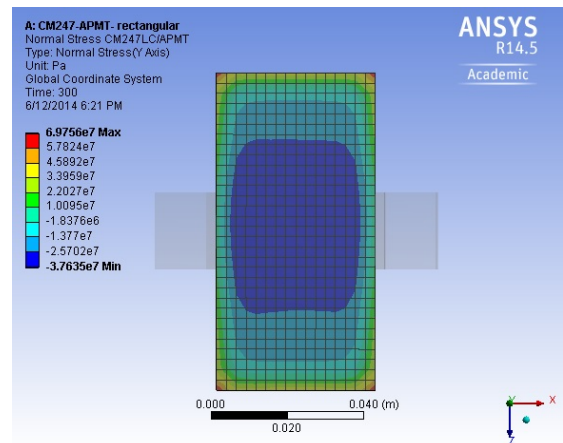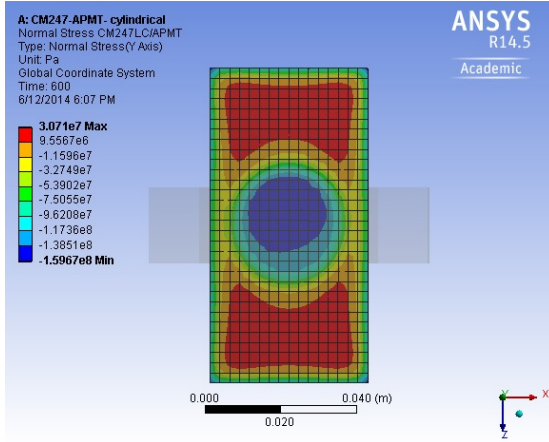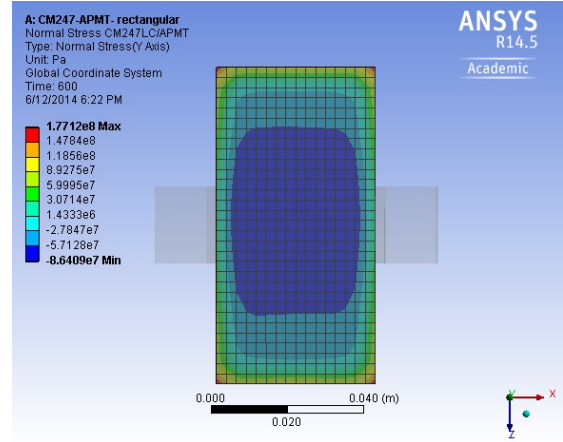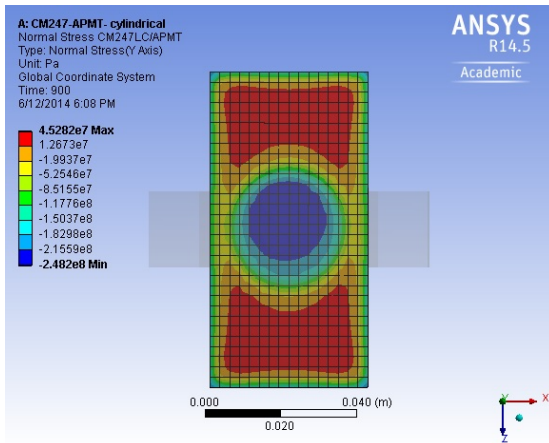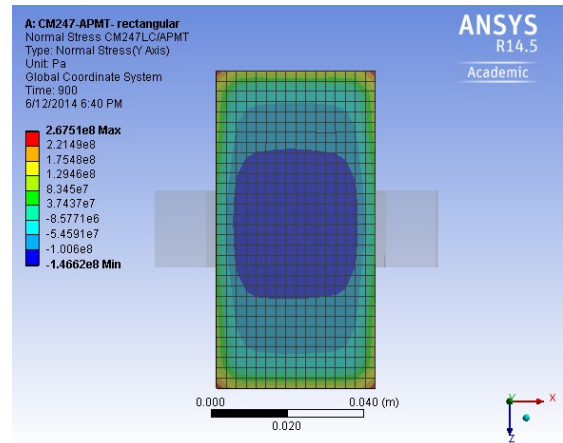(a) Cylindrical configuration

(b) Rectangular configuration

Figure B.8: Snapshots of the distribution of compressive stresses at the Bondface at 900°C for the CM 247 LC – APMT joint (no preload) .

REFERENCES

[1] Tennant, J. B., "Gasification Systems Overview," <u>DOE Gasification Program</u>, 2013, pp. 1–146.

[2] Hurley, J. P. and Cavalli, M. N., "Preparation and Testing of Corrosion–and Spallation–Resistant Coatings," <u>NETL Fossil Energy Research and Development</u>, 2011, pp. 1–146, FOA Number: DE–FOA–0000459.

[3] Phillips, J., "Different Types of Gasifiers and Their Integration with Gas Turbines," <u>DOE Gasification Report</u>, 2004, pp. 1–11.

[4] "Kanthal powder metallurgy high–temperature tubes," http://www.kanthal.com/Global/Downloads/Furnacetubes.pdf.

[5] Huang, H. and Koo, C., "Characteristics and Mechanical Properties of Polycrystalline CM 247 LC Superalloy Casting," <u>Materials Transactions</u>, Vol. 45, 2004, pp. 562–568.

[6] Aghaie-Khafri, M. and Farahany, S., "Creep Life Prediction of Thermally Exposed Rene 80 Superalloy," <u>Journal of Materials Engineering and Performance</u>, 2010, pp. 1065–1070.

[7] Cheng, J. M., "Transient Liquid Phase Bonding in the Nickel Based Superalloy CM247LC." 2003.

[8] Bordenet, B., "High Temperature Corrosion in Gas Turbines: Thermodynamic Modelling and Experimental Results," 2004.

[9] Grol, E. and Yang, W., "Evaluation of Alternate Water Gas Shift Configurations for IGCC Systems," <u>DOE Gasification Report</u>, 2009, pp. 1–11.

[10] "Introduction to Gas Turbines and Applications," http://www.epa.gov/chp/documents/presentations/.../NCHPTTRFKurzFinal.pdf?

[11] Cramer, D. S. and Covino, S. B., <u>ASM Handbook. Corrosion: Environments and Industries</u>, Vol. 13C, ASM International, Materials Park, Ohio, 2006, pp. 441–490.

[12] Covino, B. and Holcomb, G., "Corrosion in a Temperature Gradient," <u>Albany Research Center, U. S. Department of Energy</u>, Vol. 1, 2009, pp. 1–15.

[13] Bradshaw, A., Simms, N., and Nicholls, J., "Passage of trace metal contaminants through hot gas paths of gas turbines burning biomass and waste-fuels," <u>Fuel</u>, Vol. 87, 2008, pp. 3529–3536.

[14] Hurley, J. P. and Kuhnel, V., "Support Services for Ceramic Fiber–Ceramic Matrix Composites," ORNL/Sub/94–SS112/03, Vol. 94, 1998, pp. 1–14.

[15] Hurley, J. P. and Nowok, J. W., "Support Services for Ceramic Fiber–Ceramic Matrix Composites," ORNL/Sub/94–SS112/04, Vol. 94, 1999, pp. 1–7.

[16] Cramer, D. S. and Covino, S. B., ASM Handbook. Corrosion: Fundamentals, Testing, and Protection, Vol. 13A, ASM International, Materials Park, Ohio, 2003, pp. 216–959.

[17] Singh, H., Puri, D., and Prakash, S., "AN OVERVIEW OF Na2SO4 AND/OR V2O5 INDUCED HOT CORROSION OF Fe– AND Ni–BASED SUPERALLOYS," Rev. Adv. Mater. Sci., Vol. 16, 2007, pp. 27–50.

[18] Andijani, I. and Malik, A. U., "SULFUR AND VANADIUM INDUCED HOT CORROSION OF BOILER TUBES," Chemistry and Industry Conference, 2004, pp. 1–10.

[19] Liang, Y., Syuichi, I., and Yomei, Y., "HIGH TEMPERATURE CORROSION OF GAS TURBINE MATERIALS WITH ASH DEPOSITION IN METHANE GAS COMBUSTION ENVIRONMENT," Corrosion, Vol. 05445, 2005, pp. 1–7.

[20] Raask, E., Mineral Impurities In Coal Combustion, Hemisphere Publishing Corporation, New York, 1985.

[21] "Mechanisms of Oxidation and Corrosion," http://www.physics.uwo.ca/courses/Lect12.

[22] Godinho, M., Birriel, J., Marcilio, N. L., Leonardo Masotti, L., and Wenzel, M., "High–temperature corrosion during the thermal treatment of footwear leather wastes," Fuel Processing Technology, Vol. 92, 2011, pp. 1019–1025.

[23] Skrifvars, B.-J., Backman, R., Hupa, M., Salmenoja, K., and Vakkilainen, E., "Corrosion of superheater steel materials under alkali salt deposits Part 1: The effect of salt deposit composition and temperature," Corrosion Science, Vol. 50, 2008, pp. 1274–1282.

[24] Zhao, X. H., Han, Y., and Bai, Z. Q., "The experiment research of corrosion behavior about Ni–based alloys in simulant solution containing H2S/CO2," Electrochimica Acta, Vol. 56, 2011, pp. 7725–7731.

[25] Lee, D. B., Nguyen, T. D., and Kim, D. J., "High–temperature SO2–gas corrosion of TiN–Ti5Si3 composites prepared by polymer pyrolysis," Corrosion Science, Vol. 53, 2011, pp. 283–289.

[26] Deacon, R., DuPont, J., and Marder, A., "High temperature corrosion resistance of candidate nickel–based weld overlay alloys in a low NOx environment," Materials Science and Engineering A, Vol. 392, 2007, pp. 460–461.

[27] Kim, H., Mitton, D., and Latanision, R., "Corrosion behavior of Ni–base alloys in aqueous HCl solution of pH 2 at high temperature and pressure," Corrosion Science, Vol. 52, 2010, pp. 801–809.

[28] Kritzer, P., Boukis, N., and Dinjus, E., "Factors controlling corrosion in high–temperature aqueous solutions: a contribution to the dissociation and solubility data influencing corrosion processes," Journal of Supercritical Fluids, Vol. 15, 1999, pp. 205–227.

[29] Ardy, H., Putra, S., and Hardianto, T., "FAILURE OF GAS TURBINE CONE BURNER BY CARBURIZATION," Journal of KONES Powertrain and Transport, Vol. 19, 2012, pp. 1–8.

[30] Font, O., Querol, X., Plana, F., Coca, P., and Burgos, S., "Condensing species from flue gas in Puertollano gasification power plant, Spain," Fuel, Vol. 85, 2006, pp. 2229–2242.

[31] Font, O., Querol, X., Izquierdo, M., Moreno, N., Alvarez, E., Diez, S., Alvarez-Rodriguez, R., Clemente-Jul, C., Coca, P., and Garcia-Pena, F., "Partitionin of elements in an entrained flow IGCC plant:Influence of selected operational conditions," Fuel, Vol. 85, 2006, pp. 2229–2242.

[32] Kawahara, Y., "High temperature corrosion mechanisms and effect of alloying elements for materials used in waste incineration environment," Corrosion Science, Vol. 44, 2002, pp. 223–245.

[33] Bornstein, N. S., "Literature Review of Inhibitation for Vanadate Attack," AD–A, Vol. 212–213, 1988, pp. 198–325.

[34] Eliaz, N., Shemesh, G., and Latanision, R. M., "Hot corrosion in gas turbine components," Engineering Failure Analysis, Vol. 9, 2002, pp. 31–43.

[35] Stringer, J., "High temperature corrosion in practical systems," JOURNAL DE PHYSIQUE IV, Vol. 3, 1993, pp. 43–61.

[36] Harper, M. A., Barnes, J. E., and Regan, C., "Hot Corrosion Burner Rig Testing of various Commercial alloys," Nace International Corrosion99, Vol. 67, 1999, pp. 1–14.

[37] Rapp, R. A., "Hot Corrosion of Materials," Pure and Appl. Chem., Vol. 62, 1990, pp. 113–122.

[38] Bornstein, N., Roth, H., and Pike, R., "Vanadium corrosion studies," United Technologies Research Center Final Report, 1993, pp. 1–27.

[39] Rocca, E., Aranda, L., Moliere, M., and Steinmetz, P., "Nickel oxide as a new inhibitor of vanadium–induced hot corrosion of superalloys–comparison to MgO–based inhibitor," J. Mater. Chem., Vol. 12, 2002, pp. 3766–3772.

[40] May, W. R., Zetlmeisl, M. J., Annand, R. R., and Laurence, D. F., "High–temperature corrosion in gas turbines and steam boilers by fuel impurities. Part VIII. Evaluation of the effects of Mn, Ca, and several heavy metals on corrosion and slag formation," ASME Paper, Vol. 76, 1976, pp. 489–524.

[41] Zhuang, Y., Dunham, D. J., and Pavlish, J. H., "Continuation of Corrosion Potential of Bromide Injection under Taconite Operating Conditions," <u>EERC Revised Final Report</u>, 2012, pp. 1–25.

[42] Bankiewicz, D., Vainikka, P., Lindberg, D., Frantsi, A., and Silvennoinen, J., "High temperature corrosion of boiler waterwalls induced by chlorides and bromides – Part 2: Lab–scale corrosion tests and thermodynamic equilibrium modeling of ash and gaseous species," <u>Fuel</u>, Vol. 94, 2012, pp. 240–250.

[43] Hernas, A., Chmiela, B., and Szczucka-Lasota, B., "Untypical bromine corrosion in boilers co–firing biomass," <u>Journal of Achievements in Materials and Manufacturing Engineering</u>, Vol. 54, 2012, pp. 58–66.

[44] Vainikka, P., Bankiewicz, D., Frantsi, A., Silvennoinen, J., and Hannula, J., "High temperature corrosion of boiler waterwalls induced by chlorides and bromides. Part 1: Occurrence of the corrosive ash forming elements in a fluidized bed boiler co–firing solid recovered fuel," <u>Fuel</u>, Vol. 90, 2011, pp. 2055–2063.

[45] Zhuang, Y., Dunham, D. J., and Pavlish, J. H., "Assessment of Potential Corrosion Induced by Bromine Species Used for Mercury Reduction in a Taconite Facility," <u>EERC Revised Final Report</u>, 2009, pp. 1–29.

[46] Chung, K., Taejon, Y., and Lim, J., "CHARACTERISTICS OF LEAD INDUCED STRESS CORROSION CRACKING OF ALLOY 690 IN HIGH TEMPERATURE," <u>Corrosion96</u>, Vol. 93, 1996, pp. 1–9.

[47] Bankiewicz, D., Enestam, S., Yrjas, P., and Hupa, M., "Experimental studies of Zn and Pb induced high temperature corrosion of two commercial boiler steels," <u>Fuel Processing Technology</u>, Vol. 105, 2013, pp. 89–97.

[48] Zhang, J., "A review of steel corrosion by liquid lead and lead–bismuth," <u>Corrosion Science</u>, Vol. 51, 2009, pp. 1207–1227.

[49] Sakai, T., Nakagomi, T., Kikuchi, T., Aoki, K., Nakayasu, F., and Yamakawa, K., "Mechanism of Lead–induced Stress Corrosion Cracking of Nickel–Based Alloys in High–Temperature Water," <u>Corrosion Science</u>, Vol. 54, 1997, pp. 515–523.

[50] Lu, Y. C., "EFFECT OF LEAD CONTAMINATION ON STEAM GENERATOR TUBE DEGRADATION," <u>Proceedings of the 12th International Conference on Environmental Degradation of Materials in Nuclear Power System – Water Reactors</u>, 2005, pp. 1211–1218.

[51] Leeper, J. E., "Mercury – LNG Problem," <u>Hydrocarbon Processing</u>, Vol. 24, 1980, pp. 237–239.

[52] Carnell, P., Row, V. A., and McKenn, R., "A re–think of the mercury removal problem for LNG plants," <u>Puraspec</u>, 2009, pp. 1–16.

[53] Zerouali, D., Derriche, Z., and Azri, M. Y., "Effect of cathodic adsorbed hydrogen on industrial aluminium alloy AA 5083 corrosion induced by elemental mercury in LNG industries," <u>Journal of Applied Sciences</u>, Vol. 11, 2006, pp. 2394–2400.

[54] Nengkoda, A., Reerink, H., Hinai, Z., Supranto, P., Prasetyo, I., and Purwono, S., "Understanding of mercury corrosion attack on stainless steel material at gas well: case study," IPTC 13368, Vol. 13368, 2009, pp. 1–5.

[55] Palani, A., Lu, B., Tian, L., Luo, J., and Lu, Y., "Effect of magnesium on the lead induced corrosion and SCC of alloy 800 in neutral crevice solution at high temperature," Journal of Nuclear Materials, Vol. 396, 2010, pp. 189–196.

[56] Pidaparti, R. M. and Rao, S. A., "Analysis of pits induced stresses due to metal corrosion," Corrosion Science, Vol. 50, 2008, pp. 1932–1938.

[57] Mazur, Z., Kubiak, J., and Marino-Lopez, C., "Failure Analysis of Gas Turbine Last Stage Bucket Made of Udimet 500 Superalloy," Practical Failure Analysis, Vol. 2, 2002, pp. 1–7.

[58] Virmani, Y. P., "Corrosion Costs and Preventive Strategies In The United States," NACE International, Vol. 156, 2002, pp. 373–394.

[59] "Annual Cost of Corrosion in the US." http://www.g2mtlabs.com/2011/06/nace-cost-of-corrosion-study-update/.

[60] Subramanian, H., Subramanian, V., Chandramohan, P., Srinivasan, M., Rangarajan, S., Narasimhan, S., and Velmurugan, S., "Role of magnesium ions in reducing high temperature aqueous corrosion of carbon steel," Corrosion Science, Vol. 70, 2013, pp. 127–139.

[61] Fukumoto, M., Tachikawame, C., Matsuzaka, Y., and Hara, M., "Formation of Si diffusion layer on stainless steels and their high temperature corrosion resistance in molten salt," Corrosion Science, Vol. 56, 2012, pp. 105–113.

[62] Immarigeon, J.-P., Parameswaran, V. R., Chow, D., and Morphy, D. D., "Evaluation of Thermal Barrier Coatings from Burner Rig Tests," AGARD SMP Meeting, Vol. R–823, 1997, pp. 1–10.

[63] Reed, R., The Superalloys Fundamentals and Applications, Cambridge University Press, New York, 2006.

[64] Gurrappa, I., "Thermal barrier coatings for hot corrosion resistance of CM 247 LC superalloy," JOURNAL OF MATERIALS SCIENCE LETTERS, Vol. 17, 1998, pp. 1267–1269.

[65] Tortorellia, P. F. and Natesanb, U. K., "Critical factors affecting the high–temperature corrosion performance of iron aluminides," Materials Science and Engineering, Vol. 258, 1998, pp. 115–125.

[66] Singh, H., Surendra, S., and Prakash., "High temperature corrosion behavior of some Fe–, Co– and Ni–based superalloys in the presence of Y2O3 as inhibitor," Applied Surface Science, Vol. 255, 2009, pp. 7062–7069.

[67] Phongphiphat, A., Ryu, C., Yang, B., and Finney, K. N., "Investigation into high–temperature corrosion in a large–scale municipal waste–to–energy plant," Corrosion Science, Vol. 52, 2010, pp. 3861–3874.

[68] "Gasification Systems Main Area: Gas Cleaning," http://www.netl.doe.gov/technologies/coalpower/gasification/gas-clean/.

[69] Marchant, D. D., Griffin, C. W., and Bates, J. L., "ELECTROCHEMICAL CORROSION OF IRONMAGNESIUM–ALUMINA SPINEL (FMAS) IN MOLTEN POTASSIUM SALTS AND COAL SLAG," J. Mol. Liq., Vol. PNL–3627, 1981, pp. 1–117.

[70] Hurley, J. P. and Schobert, H. H., "Ash Formation During Pulverized Subbituminous Coal Combustion. 1. Characterization of Coals, and Inorganic Transformations during Early Stages of Burnout," Energy and Fuels, Vol. 6, 1992, pp. 47–58.

[71] Hurley, J. P. and Schobert, H. H., "Ash Formation During Pulverized Subbituminous Coal Combustion. 2. Inorganic Transformation during Middle and Late Stages of Burnout," Energy and Fuels, Vol. 7, 1993, pp. 542–553.

[72] Laumb, J., Benson, S., Crocker, C., Gunderson, J., and Jensen, R., "EVALUATION OF POTENTIAL SCR CATALYST BLINDING DURING COAL COMBUSTION AND ADD–ON: IMPACT OF SCR CATALYST ON MERCURY OXIDATION IN LIGNITE–FIRED COMBUSTION SYSTEMS." UNDEERC–final–report, Vol. 31, 2004, pp. 1–69.

[73] "Wood gas as engine fuel," http://www.fao.org/docrep/t0512e/T0512e0a.htmTopOfPage.

[74] "Synthesis Gas Treating." http://www.uop.com/processing-solutions/gas-processing/synthesis-gas-treating/.

[75] Gibbons, T. B. and Wright, I. G., "A REVIEW OF MATERIALS FOR GAS TURBINES FIRING SYNGAS FUELS," ORNL/TM, Vol. 137, 2009, pp. 47–50.

[76] "Determination of Metals Emissions from Stationary Sources - US," http://www.epa.gov/ttnemc01/promgate/m-29.pdf.

[77] "Atomic Absorption Spectroscopy." http://www.galbraith.com/spectroscopy.htm.

[78] Gardner, B., Davidson, M., Guan, X., Hendrix, H., Shirley, B., Dahlin, R., Landham, C., and Spain, J., "Commercial Readiness Of Hot–Gas Filtration For Pressurized Combustion." International Conference On Fluidized–Bed Combustion, Vol. 16th, 2001, pp. 1–15.

[79] Foster, A. D., von Doering, H. E., and Hilt, M. B., "Fuels flexibility in heavy–duty gas turbines." General Electric Reference Document, Vol. GER–3428a, 1983, pp. 1–33.

[80] Pavri, R. and Moore, G. D., "Gas turbine emissions and control." General Electric Reference Document, Vol. GER–4211, 2001, pp. 1–36.

[81] "Syngas Processing Systems."
http://www.netl.doe.gov/research/coal/energy-systems/gasification/syngas.

[82] "Conversion of micrograms per cubic meter to ppm."
http://www.gasdetection.com/calculator/mic2ppm.xls.

[83] Gurrappa, I., "Hot Corrosion Behavior of CM 247 LC Alloy in Na2SO4 and NaCl Environments," Oxidation of Metals, Vol. 51, 1999, pp. 353–382.

[84] Khorrami, M. R., Ashrafizadeh, F., and Saatchi, A., "Kinetic and Morphological Study of Hot Corrosion of Rene 80 Nickel Based Super Alloy." Journal of Applied Chemical Research, Vol. 8, 2009, pp. 31–38.

[85] Onishi, M. and Miura, H., "Effect of Compressive Stress on Reaction–Diffusion in the Cu–Si System," Transactions of the Japan Institute of Metals, Vol. 18, 1977, pp. 107–112.

[86] Moilanen, A., "CREEP EFFECTS IN DIFFUSION BONDING OF OXYGEN–FREE COPPER." 2013.

[87] "Diffusion Bonding,"
http://www.vpei.com/technologies-processes/diffusion-bonding.

[88] Braband, J. E., "CHARACTERIZATION OF EVAPORATIVE METAL BONDING IN SUPERALLOYS FOR USE IN GASIFIED COAL TURBINE GENERATORS," 2013.

[89] Mahendran, G., Balasubramanian, V., and Senthilvelan, T., "Influences of diffusion bonding process parameters on bond characteristics of Mg–Cu dissimilar joints." Transaction of Nonferrous Metals Society of China, Vol. 20, 2010, pp. 997–1005.

[90] Al-Ajaj, E., Abdul-Rassol Awfa, A., and Moosa, A., "Modeling and Experimental Studies of Diffusion Bonding of Inconel 600 to Pyrolytic Graphite." International Journal of Metallurgical and Materials Science and Engineering, Vol. 3(1), 2013, pp. 9–30.

[91] Kadhim, Z., Al-azzawi, A. I., and Al-Janabi, S. J., "Effect of the Diffusion Bonding Conditions on Joint Strength." Journal of Engineering and Development, Vol. 13(1), 2009, pp. 179–188.

[92] Masahashi, N. and Hanada, S., "Effect of Pressure Application by HIP on Microstructure Evolution during Diffusion Bonding." Materials Transactions, Vol. 46(7), 2005, pp. 1651–1655.

[93] Eslami, P. and Karimi Taheri, A., "An investigation on diffusion bonding of aluminum to copper using equal channel angular extrusion process." Materials Letters, Vol. 65, 2011, pp. 1862–1864.

[94] Ekrami, A., Moeinifar, S., and Kokabi, A., "Effect of transient liquid phase diffusion bonding on microstructure and properties of a nickel base superalloy Rene 80." Materials Science and Engineering A, Vol. 456, 2007, pp. 93–98.

[95] Cverna, F., <u>ASM Ready Reference: Thermal Properties of Metals</u>, Vol. 06702G, ASM International, Materials Park, Ohio, 2002, pp. 9–220.

[96] E831-06, A. S., <u>Standard Test Method for Linear Thermal Expansion of Solid Materials by Thermomechanical Analysis</u>, Annual Book of ASTM Standards, 2000, pp. 241–245.

[97] "MOLYBDENUM AND ITS ALLOYS," http://www-ferp.ucsd.edu/LIB/PROPS/PANOS/moa.html.

[98] "AISI E 52100 Steel." Matweb. Matweb LLC." http://www.matweb.com/search/datasheet–print.aspxmatguid.

[99] "Kanthal APMT Kanthal. AB Sandvivik Materials Technology." http://www.matweb.com/search/datasheet.aspx?matguid.

[100] "Average linear thermal expansion coefficient of CM247LC, Udimet720LI, CMSX–4 and TMS," http://www.ostec.or.jp/nmc/ndb/cgi–bin/NI/nktb6.htm.

[101] "Rene 80." Stainless SS. Jiangyou Longhai Special Steel Co, Ltd." http://www.steelss.com/High–alloy/rene–80.html.

[102] "Molybdenum, Mo, Annealed." http://www.matweb.com/search/datasheet-print.aspxmatguide.

[103] Sehitoglu, H. and Maier, H. J., <u>Thermo–mechanical Fatigue Behavior of Materials: Third Volume.</u>, Materials Park: ASM International, 2000.

[104] Moore, Z., "Life Modeling of Notched CM247LC DS Nickel–Base Superalloy." 2008.

[105] "Coefficient of Thermal Expansion Data," http://www.repairengineering.com/coefficient–of–thermal–expansion.html.

[106] "Coefficient of Linear Thermal Expansion," http://www.engineeringtoolbox.com/linear-expansion-coefficients-d95.html.

[107] "Data Table for Steel Grades: High Alloy–Rene 80," http://www.steelgr.com/Steel–Grades/High–Alloy/rene–80.html.

[108] Xiaoqin, S., Yajiang, L., Putchkov, U., Juan, W., and Wanqun, H., "Finite-element analysis of residual stresses in Al2O3-TiC/W18Cr4V diffusion bonded joints." <u>Computational Materials Science</u>, Vol. 45, 2009, pp. 407–410.